

GROWTH OF EPITAXIAL ZIRCONIUM CARBIDE LAYERS  
USING PULSED LASER DEPOSITION

By

JUHYUN WOO

A DISSERTATION PRESENTED TO THE GRADUATE SCHOOL  
OF THE UNIVERSITY OF FLORIDA IN PARTIAL FULFILLMENT  
OF THE REQUIREMENTS FOR THE DEGREE OF  
DOCTOR OF PHILOSOPHY

UNIVERSITY OF FLORIDA

2005

Copyright 2005

by

Juhyun Woo

Dedicated to Jihoon, the parents of us all, and Dr. Craciun.

## ACKNOWLEDGMENTS

I would like to express my gratitude to Dr. Valentin Craciun without whose help, guidance and encouragement this work might not have been possible. Also I would like to express my sincere appreciation to my committee members, Dr. Fereshteh Ebrahimi, Dr. Rajiv K. Singh, Dr. Cammy Abernathy, and Dr. Timothy J. Anderson. Especially, I am deeply grateful to Dr. Ebrahimi. A lot of what I have learnt is due to her guidance.

Also I would like to thank Gerald Bourne and Kerry Siebein. Gerald Bourne helped me to solve many problems in nanoindentation measurements, and Kerry Siebein helped me to get outstanding high resolution TEM images. The assistance and help of Wayne Acree and Eric Lambers to obtain high quality SEM, XPS, and AES results are gratefully acknowledged. I also would like to thank Woochul Kwak and Sang-yup Kim for their help with AFM and FE-SEM. And I personally thank Dr. Luisa Amelia Dempere for giving me a great opportunity of working in Major Analytical Instrumentation Center and “hands-on” learning about thin film characterization.

Finally I would like to thank my wife Jihoon Yi for her support and patience. My best friend and senior Sang-yup Kim helped me a lot to focus on my research.

## TABLE OF CONTENTS

	<u>page</u>
ACKNOWLEDGMENTS .....	iv
LIST OF TABLES .....	vii
LIST OF FIGURES .....	viii
ABSTRACT .....	xiii
CHAPTER	
1 INTRODUCTION .....	1
2 LITERATURE REVIEW .....	4
2.1 Characteristics of Zirconium Carbide.....	4
2.1.1 Composition and Structure .....	4
2.1.2 Properties and Applications of Zirconium Carbide Thin Films .....	5
2.2. Techniques Used for Zirconium Carbide Thin Film Depositions .....	7
2.2.1 Thermal Evaporation (TE) .....	7
2.2.2 Sputtering Deposition (S) .....	7
2.2.3 Chemical Vapor Deposition (CVD) .....	8
2.2.4 Pulsed Laser Deposition (PLD) .....	9
2.2.5 Comparison of Techniques.....	12
2.3 Growth and Factors Determining the Quality of Thin Films in PLD.....	13
2.3.1 Nucleation and Growth.....	13
2.3.2 Background Gas .....	15
2.3.3 Vacuum.....	16
2.3.4 Laser Fluence.....	17
2.3.5 Laser Wavelength.....	17
2.3.6 Target to Substrate Distance.....	18
3 EXPERIMENTAL METHODS.....	24
3.1 Pulsed Laser Deposition System .....	24
3.2 Structural Characterization .....	25
3.3 Film Thickness and Roughness .....	26
3.4 Surface Chemistry Analysis .....	27
3.5 Electrical Measurement .....	28

4 GROWTH AND CHARACTERIZATION OF HIGH CRYSTALLINE QUALITY ZIRCONIUM CARBIDE FILMS .....	31
4.1 Introduction.....	31
4.2 Experiment.....	32
4.3 Results and Discussion .....	33
4.3.1 Laser Fluence and Temperature Effect on Deposited Films .....	33
4.3.2 Deposition Rate and Thickness Uniformity of Deposited Films.....	35
4.3.3 ZrC Films Growth at High Temperature and High Laser Fluence.....	38
4.3.3.1 Growth behaviors of ZrC films deposited on Si and sapphire substrate .....	39
4.3.3.2 TEM analysis of ZrC films grown on Si and sapphire substrate .....	43
4.3.4 Surface analysis of ZrC films .....	45
4.4 Summary.....	49
5 MECHANICAL PROPERTIES OF ZIRCONIUM CARBIDE FILMS MEASURED BY NANOINDENTATION.....	85
5.1 Introduction.....	85
5.2 Experiment.....	86
5.3 Nanoindentation Test.....	87
5.4 Result and Discussion.....	88
5.4.1 Hardness and Young's Modulus of Substrates.....	88
5.4.2 Hardness and Elastic Modulus of ZrC Films Deposited on Si (001), Si (111), and Sapphire.....	90
5.5 Summary.....	91
6 CONCLUSION.....	101
LIST OF REFERENCES.....	106
BIOGRAPHICAL SKETCH .....	111

## LIST OF TABLES

<u>Table</u>	<u>page</u>
2-1 Characteristics and properties of ZrC reported in literature .....	5
3-1 Excimer laser operating wavelengths .....	24
3-2 Typical XRR values for the resolution and ranges .....	27
4-1. Growth conditions of deposited films, showing GIXD spectra in fig. 4-1 .....	34
4-2. Thickness, density, and surface roughness values of the ZrC films deposited at 700 °C for different times .....	36
4-3. Degree of out-of-plane texture of ZrC films at various growth conditions .....	37
4-4. Structure information of ZrC , Si, and sapphire and lattice mismatch .....	38
4-5. Surface roughness and density of as-grown films .....	46
4-6. The relative percentage of Zr 3d XPS areas corresponding to Zr-C bonds at different take-off angles .....	48
4-7. Resistivity of as-deposited ZrC films .....	48
5-1. Poisson's ratio and Young's modulus of Al <sub>2</sub> O <sub>3</sub> (poly), Si, and diamond tip .....	88

## LIST OF FIGURES

<u>Figure</u>	<u>page</u>
2-1. Image of cubic rocksalt (B1) structure of transition metal carbides. Carbon atoms are depicted as the light gray spheres, metals as dark gray spheres.....	19
2-2. Zr-C phase diagram showing wide range congruent compositions.....	19
2-3. Schematic diagram of an apparatus for pulsed laser deposition.....	20
2-4. Schematic diagram of the approximate energy range of deposited atoms for various deposition techniques. The shaded box indicates the supposed energy range of atom fluxes considered to be beneficial for film growth .....	21
2-5. Schematic diagram comparing the pressure ranges over various techniques. PLD can operate over the widest range of all the methods .....	21
2-6. Growth diagram drawn by equation 2-3, showing the dependence of growth behavior on temperature and growth rate.....	22
2-7. Relationship of impinging particles fluxes to deposition rate, and gas pressure.....	22
2-8. ZrC ablation rate, showing linear dependence on laser fluence, and threshold laser fluence of 1.3 J/cm <sup>2</sup> .....	23
3-1. A schematic diagram of symmetric and asymmetric GIXD geometry .....	29
3-2. A schematic diagram of omega rocking curve geometry .....	29
3-3. An example of a schematic reflections on pole figure related to crystal quality.....	30
4-1. GIXD spectra (incidence beam angle, $\omega = 1^\circ$ ) of ZrC films deposited under various conditions .....	51
4-2. Comparison of GIXD spectra obtained from ZrC deposited films at same deposition conditions (a) without pre-ablated target (red) and (b) with pre-ablated target (blue).....	51
4-3. XRD spectra obtained from ZrC target; vertical lines represent position and intensity for stoichiometric ZrC, JCPDS PDF# 32-1489 .....	52

4-4. GIXD spectra obtained from films deposited under residual vacuum and different $C_2H_2$ gas pressures .....	52
4-5. XRR spectra of ZrC films deposited for various times at 700 °C and 10 J/cm <sup>2</sup> under vacuum .....	53
4-6. ZrC film deposition rate at $T_s = 700^\circ\text{C}$ , $P_d = 1.0 \times 10^{-6}$ Torr, 10 J/cm <sup>2</sup> , and 5Hz.....	53
4-7. GIXD spectra of ZrC films deposited for various times at 700 °C and 10 J/cm <sup>2</sup> under vacuum; the standard position of diffraction lines from ZrC (dashed lines) and ZrC <sub>0.7</sub> (solid lines) are also shown.....	54
4-8. XRD spectra of ZrC films deposited for various times at 700 °C and 10 J/cm <sup>2</sup> under vacuum .....	54
4-9. XRD spectra of ZrC films deposited at 750 °C on various substrates .....	55
4-10. XRD and GIXD spectra (incidence beam angle = 1°) of ZrC films deposited on Si (111) substrates .....	55
4-11. Omega-rocking curves of ZrC (111) or (200) peaks recorded from ZC104 films deposited at 750 °C on various substrates.....	56
4-12. Omega-rocking curves of ZrC (002) peaks recorded from the films deposited on Si (001) substrate at various background gas pressures.....	56
4-13. Omega-rocking curves of ZrC (111) peaks recorded from the films deposited on sapphire (0001) substrate at various different gas pressures.....	57
4-14. XRD spectra of (002) reflection from the films deposited on Si (001) and calculated lattice parameters .....	57
4-15. Background gas effect on lattice parameter of the films deposited on Si (001) substrate.....	58
4-16. The relationship between deposited films on Si (001) and texture degree of the films measured by omega-rocking curve .....	58
4-17. Phi-scan of {111} in-plane obtained from (a) ZrC film and Si (001) substrate of sample ZC202 and (b) phi-scan diffractometer configuration.....	59
4-18. (111) pole figures of (a) ZrC film and (b) Si (001) substrate obtained from sample ZC202 .....	60
4-19. (100) pole figures of (a) ZrC film and (b) Si (111) substrate obtained from sample ZC104 .....	61
4-20. Pole figures showing (a) (100) pole figures of ZrC film, and (b) (1 1-2 6) pole figure of sapphire (0001) substrate obtained from ZC104.....	62

4-21. Projection view for two crystallographic orientations of ZrC grown on sapphire (0001), and orientation relationship between ZrC film and sapphire substrate .....	63
4-22. Possible nucleation site (marked as A) for the first monolayer on sapphire (0001). .....	63
4-23. Bright field TEM image obtained from cross-section of ZrC film grown on silicon (111) substrate; the regions showing inhomogeneous random grains are marked.....	64
4-24. TEM (a) bright field image and (b) SADP (selected area electron diffraction pattern) obtained from cross-section of ZrC film (sample ZC104) grown on silicon (111) substrate .....	65
4-25. TEM (a) bright field image and (b) SADP (selected area electron diffraction pattern) obtained from cross-section of ZrC film grown on silicon (001) substrate; diffraction pattern obtained from ZrC film is marked by circles.....	66
4-26. Bright field TEM image obtained from cross-section of ZrC film grown on silicon (001) substrate exhibiting clear lattice fringe .....	67
4-27. Bright field TEM image obtained from cross-section of ZrC film grown on sapphire (0001) substrate showing sharp interface; the regions marked as A and B are magnified in figure 4-28 for observation of twinning .....	68
4-28. High resolution TEM image of (a) 'A' region in fig. 4-26, showing parallel twin to the surface of film; (b) 'B' region in fig. 4-26, showing perpendicular twin to the surface of film .....	69
4-29. Secondary electron images of ZrC surface grown on Si (001) substrate, at $\times 10K$ (a), and $\times 50K$ (b).....	70
4-30. Secondary electron images of ZrC surface grown on sapphire (0001) substrate, at $\times 10K$ (a), and $\times 50K$ (b).....	71
4-31. AFM height images obtained from the surface of ZC106 sample (ZrC (001) layer grown on Si (001) substrate) .....	72
4-32. AFM height images obtained from the surface of ZC202 sample (ZrC (001) layer grown on Si (001) substrate) .....	73
4-33. AFM height images obtained from the surface of ZC208 sample (ZrC (001) layer grown on Si (001) substrate) .....	74
4-34. AFM height images obtained from the surface of ZC107 sample (ZrC (111) layer grown on Si (111) substrate) .....	75

4-35. AFM height images obtained from the surface of ZC208 sample (ZrC (111) layer grown on sapphire (0001) substrate).....	76
4-36. AFM height images obtained from the surface of ZC210 sample (ZrC (111) layer grown on sapphire (0001) substrate).....	77
4-37. Cross-sectional bright field TEM image showing an oxidized layer due to discontinued growth.....	78
4-38. Cross-sectional bright field TEM image showing distinguishable three layers, also supporting a model used for XRR analysis.....	78
4-39. Z-contrast image of cross-sectional ZC106 sample for TEM-EDX analysis by line and point scan.....	79
4-40. High resolution Zr 3d spectra acquired at 45° and 90° take off angles and their fitting for an as-received sample deposited at 600 °C under vacuum.....	80
4-41. High resolution Zr 3d spectra acquired at 45° and 90° take off angles and their fitting for a sample deposited at 600 °C under $1 \times 10^{-4}$ Torr of C <sub>2</sub> H <sub>2</sub> that was sputtered-clean by Ar <sup>+</sup> bombardment.....	81
4-42. AES depth profile of an as-deposited ZrC film.....	82
4-43. AES survey spectrum of a ZrC film (ZC202) sputtered with a 4 kV Ar ion beam..	82
4-44. AES survey spectrum of (a) a as-deposited ZrC film under CH <sub>4</sub> atmosphere and (b) the ZrC film sputtered for 1 min with a 4 kV Ar ion beam.....	83
4-45. Residual gas partial pressure analyzed by RGA before deposition at (a) vacuum and right after introducing (b) C <sub>2</sub> H <sub>2</sub> and (c) CH <sub>4</sub> .....	84
5-1. Tip area function used for calculation of mechanical properties.....	92
5-2. Example of erroneous fitting of tip area function in depth below 5nm range.....	92
5-3. Hardness of Si (001), Si (111), and sapphire (0001) single crystal substrates.....	93
5-4. Young's modulus of Si (001), Si (111), and sapphire (0001) single crystal substrates.....	93
5-5. Error range change in Young's modulus as function of Poisson's ratio of substrate according to eq. (5-1).....	94
5-6. Load-displacement curves of Si (001) substrate.....	94
5-7. Load-displacement curves of Si (111) substrate.....	95
5-8. Load-displacement curves of sapphire (0001) substrate.....	95

5-9. Load-displacement curves of sapphire (0001) substrate before ‘pop-in’ occurs.....	96
5-10. Combined modulus of film and substrate for different quality of ZrC (001) grown on Si (001) substrate. FWHM of ZC202 = 2.53, FWHM of ZC210a = 7.27 in omega rocking curve.....	96
5-11. Load-displacement curves of ZrC (001) grown on Si (001) substrate, sample ZC202 in fig 5-10.....	97
5-12. Load-displacement curves of ZrC (001) grown on Si (001) substrate, sample ZC202 in fig 5-10.....	97
5-13. Measured elastic modulus as a function of relative penetration into a coated specimen (a is contact radius, and t is film thickness). For curve 1, $E_{\text{film}}$ is less than $E_{\text{substrate}}$ , and opposite case for curve 2 .....	98
5-14. Combined modulus of film and substrate for different quality of ZrC (111) grown on sapphire (0001) and Si (001) substrate, sample ZC204 and ZC210c respectively. FWHM of ZC204 = 2.53, FWHM of ZC210c = 6.95 in omega rocking curve.....	98
5-15. Load-displacement curves of ZrC (111) grown on sapphire (0001) substrate, sample ZC204 in fig 5-14.....	99
5-16. Load-displacement curves of ZrC (111) grown on Si (111) substrate, sample ZC210c in fig 5-14.....	99
5-17. Combined hardness of ZrC and substrate as a function of normalized depth; h - displacement, t - film thickness.....	100
6-1. XRD spectra of thin films deposited from a Co doped ZrC target under various conditions .....	105

Abstract of Dissertation Presented to the Graduate School  
of the University of Florida in Partial Fulfillment of the  
Requirements for the Degree of Doctor of Philosophy

GROWTH OF EPITAXIAL ZIRCONIUM CARBIDE LAYERS  
USING PULSED LASER DEPOSITION

By

Juhyun Woo

December 2005

Chair: Valentin Craciun

Major Department: Materials Science and Engineering

Epitaxial ZrC thin films were grown on Si (001), Si (111), and sapphire (0001) substrate by the pulsed laser deposition technique. It has been found that crystalline films could be grown only by using laser fluences higher than  $6 \text{ J/cm}^2$  and substrate temperatures in excess of  $600 \text{ }^\circ\text{C}$ . For a fluence over  $8 \text{ J/cm}^2$  and a substrate temperature of  $600\sim 700 \text{ }^\circ\text{C}$ , cubic ZrC films exhibiting a (001) texture were deposited under vacuum or low pressure  $\text{C}_2\text{H}_2$  atmosphere. Under very low water vapor pressures ( $10^{-8}\sim 10^{-9}$  Torr), high substrate temperatures ( $700\sim 750 \text{ }^\circ\text{C}$ ), and high laser fluence ( $10 \text{ J/cm}^2$ ), highly textured ZrC films were deposited on single crystalline substrates. Pole figures investigation showed that films were epitaxial, with in-plane axis aligned with respect to those of the substrate. X-ray reflectivity, atomic force microscope, ellipsometry, and scanning electron microscopy confirmed that these films were smooth, with surface roughness values below  $1.0 \text{ nm}$  and mass densities around the stoichiometric ZrC tabulated value of  $6.7 \text{ g/cm}^3$ . X-ray photoelectron spectroscopy and Auger electron

spectroscopy investigations showed that the surface of the films contained a significant amount of oxygen and Zr-O bonds, the outmost 1~2 nm of the surface region being mainly ZrO<sub>2</sub>. However, after the removal of this surface contamination layer, low oxygen atomic concentration below 3 % were measured. Despite of the rather high levels of oxygen contamination, electrical resistivity measured by four probe measurement indicated that the deposited ZrC films were very conductive. The use of a low C<sub>2</sub>H<sub>2</sub> pressure atmosphere during deposition had a small beneficial effect on crystallinity and stoichiometry of the films. Nanoindentation measurements showed higher values of the hardness for higher crystallinity. For the highest crystalline quality, (111) ZrC films deposited on sapphire, values over 450 GPa for the elastic modulus and ~31 GPa for the hardness were measured.

## CHAPTER 1 INTRODUCTION

Zirconium carbide (ZrC) is a typical refractory compound that crystallizes in the rock salt (NaCl, B1) ground-state structure under normal conditions. Recently, ZrC is arousing interest because of its several notable properties, characterized by a very high melting temperature of 3530 °C [Zai84], excellent thermal stability, exceptional mechanical hardness and strength [Che05a], chemical inertness, and imperviousness to hydrogen attack [Tot71]. In addition, electrical conductivity is comparable to metals [Zai84], and work function for electron emission is low [Mac95].

The common applications are in chemical- and wear-resistant coatings and ultra-high temperature applications so far. However, as a form of thin coating or layer (or film) in a thickness range of micron or submicron, ZrC has more important applications in vacuum electronics or MEMS (micro electro-mechanical system) devices [Cha01, Tem99, and Xie96]. Particularly, the growth of epitaxial ZrC film has special importance because of its anisotropic properties and possibility to be fabricated in various shapes of microstructure by using anisotropic etching. When it is manufactured as a form of microstructured shapes, its applications are much wider with high efficient and compact devices, using electron emission, such as short responding bright flat displays and electron beam lithography. Also ZrC is a potential good candidate as a diffusion barrier for metallization on silicon because it exhibits lower lattice mismatch and thermal expansion coefficient difference with silicon (Si) than that of zirconium nitride (ZrN).

Especially, epitaxial films for this application could very efficiently prevent diffusion of metal atoms (Al or Cu) because there are no grain boundaries for fast atomic diffusion.

Despite such many attractive applications and technological interest, only a few studies describing ZrC film growth have been published so far. The growth of ZrC film by thermal evaporation [Tes93], sputtering deposition [Brü93, Spr86], vacuum plasma spray processes [Var94], chemical vapor deposition (CVD) [Ber95], pulsed laser deposition (PLD) [Ale00], and ion beam deposition [He98] have been reported. However, it appears that it is quite difficult to obtain high crystalline quality ZrC film, because of its high melting temperature, low vapor pressure, and Zr atoms affinity for oxygen.

The objective of this study was focused on studying the relationship between the thin film deposition parameters and the structure and properties of the resulting ZrC films. Based on performance considerations, a pulsed laser deposition technique for the growth of ZrC thin film had been chosen, and hence used in this work. In chapter 2, a general background of ZrC material was presented, and growth methods and problems were discussed as well. In chapter 3, the experimental method and characterization tools used for analysis of film properties were explained. Grazing incidence x-ray diffraction (GIXD), symmetrical XRD, and pole figure were used for structure analysis. Omega rocking curve technique was used to check the degree of texture of films. X-ray reflectometry (XRR), atomic force microscope (AFM), scanning electron microscopy (SEM), and ellipsometry were used for surface morphology, thickness and/or roughness measurement. Auger electron spectroscopy (AES) and X-ray photoelectron spectroscopy (XPS) were used for surface chemical analysis. Four points probe was used to measure electrical sheet resistance and resistivity, while transmission electron microscope (TEM)

was used for microstructure analysis. In chapter 4, the influence of process parameters on the microstructure, crystallinity, and morphology were presented, and also the dependence of substrates and its orientation on growth behavior of ZrC thin film was analyzed and discussed. In chapter 5, the results regarding the hardness and elastic modulus of ZrC films, obtained by nanoindentation technique, were presented. Finally, the overall conclusions drawn from this work and suggestions for future work were summarized in chapter 6.

## CHAPTER 2 LITERATURE REVIEW

### 2.1 Characteristics of Zirconium Carbide

#### 2.1.1 Composition and Structure

Zirconium (Zr,  $[\text{Kr}]4d^25s^2$ , group IVB) is a solid transition metal which has a hexagonal close-packed (HCP) crystal structure at room temperature. Carbon (C,  $1s^22s^2p^2$ , group IV) also naturally crystallizes in the same HCP structure. However, the structure of the zirconium carbide (ZrC) does not follow its parent metal structures. That is, ZrC has the Zr on a face centered cubic (FCC) lattice, even though Zr has HCP structure, and carbon atoms occupy octahedral interstitial sites between Zr atoms. In transition metal carbides, their structure depends on the s-p electron count [Oya92a]. With increasing s-p electron count, the metal structure changes from body centered cubic (BCC) to HCP to FCC across the transition series. Therefore, the group IVB and VB metal carbides (MC) crystallize in the rock salt (B1, NaCl-type) structure (fig. 2-1) rather than a hexagonal form because the partially filled bands of the host metals can accommodate a high ratio of sp-electron-rich carbon to metal. In group IV the stoichiometry of  $\text{M}_2\text{C}$  occurs often, while group VII and VIII retain metal-rich stoichiometries of  $\text{M}_3\text{C}$  and  $\text{M}_4\text{C}$ , consistent with an attempt to avoid filling anti-bonding levels in the metal bands [Oya92b].

Most of the transition metal mono-carbides form in the rock salt structure, fcc metal with carbon occupying the octahedral interstitial sites. The shortest metal to metal distance is about 30% greater in the metal carbide (MC) structure than in the pure metal

structure for the group IV and group V carbides [Oya92a]. At one hundred percent site occupancy, the stoichiometry of transition metal carbide is  $M_1C_1$ . Although the zirconium carbide is stable in solid solutions composition from carbon-deficient  $ZrC_{1-x}$  to stoichiometric ZrC (Fig. 2-2) [Bra92], it has been reported that crystalline ZrC film with rocksalt structure can be synthesized with Zr to C atomic ratios from 0.5 up to 1.78 as a vacancy compound [Brü93, Smi93, and Tes93].

### 2.1.2 Properties and Applications of Zirconium Carbide Thin Films

The properties of ZrC depend on several factors such as chemical compositions, grain size, defect structures, and porosity. Hence, variations in properties have been observed in the literature. Some of the characteristics and properties of zirconium carbide reported in the literature are listed in table 2-1.

Table 2-1 Characteristics and properties of ZrC reported in literature.

Structure	Rocksalt (B1) [Oya92a, Tot71]
Space group	Fm3m (225) [JCPDS PDF#: 35-0784]
Lattice parameter (Å)	4.698 [Tot71], 4.6930 [JCPDS PDF#: 35-0784]
Density (g/cm <sup>3</sup> )	6.59 [Tot71], 6.73 [Lid05]
Hardness	2860 kg/mm <sup>2</sup> [Zai84], up to 30.2 GPa [Che05a]
Elastic modulus (GPa)	~325 [Che05a]
Melting temperature (°C)	3532 [Lid05], 3530 [Zai84], 3420 [Shi98]
Thermal expansion ( $\times 10^{-6}/^{\circ}C$ )	6.7 [Tot71]
Electrical resistivity ( $\times 10^{-5}\Omega\cdot m$ )	6.2 at 293 K [Zai84], 20.4 at 300 K [Mod85]
Work function (eV)	3.38 [Zai84], 3.3~3.4 [Mac95]

As shown in table 2-1, ZrC exhibits many unusual properties such as high thermal and electrical conductivity with extreme hardness, and low work function. Recently, most

applications of the zirconium carbide rely on its significant hardness such as cutting tools [Pri92 and Tot71]. However, these combinations of properties are more important in a variety of technological applications. For example, zirconium carbide coatings on molybdenum, niobium, and nickel-based alloy were used to increase the radiation emissivity, indicating a good candidate material for thermophotovoltaic (TPV) radiator [Coc99]. Also, the coatings showed excellent resistance to thermal cycling and acceptable stability during vacuum annealing at 1100 °C.

In addition, ZrC films improved the field emission stability and beam confinement when they were deposited on field emitter cathodes [Eda96 and Mac95]. The full width at half maximum of energy distribution for particular materials is nearly equal to a half of the work function [Ada74]. Thus, the cathodes of low work function have an advantage because the full width at half maximum in energy distribution of the emitted electrons is narrow.

Moreover, ZrC coating layers have much higher temperature stability and are more resistant to the chemical attack by the palladium (Pd) fission product, while silicon carbide (SiC) coating layers lose their mechanical integrity at temperatures over 1700 °C [Oga86 and Oga92].

Furthermore, video displays [Mac98a, Mac98b, and Mac98c], microwave application [Mac92, Mac93, Mac94, Mac95, and Xie96], cold cathodes for operation in poor vacuum environment, photocathodes for electron beam lithography [She97], hole injection layers of organic light-emitting diodes (OLEDs), and substrates for epitaxial growth of nitride are good potential fields for ZrC applications.

## **2.2. Techniques Used for Zirconium Carbide Thin Film Depositions**

### **2.2.1 Thermal Evaporation (TE)**

The thermal evaporation technique for ZrC films deposition was used by Tessner and Davis in 1993 [Tes93] to widen the emission area of high-temperature thermionic energy converters (TEC) and by Mackie et al. for the use of field emitter arrays (FEAs) [Mac95]. In the evaporation process, the material to be deposited should be heated to a high enough temperature to achieve a sufficient vapor pressure and the desired evaporation. The wire filaments, sheet metal, or electrically conductive ceramic sources are used in evaporation and they are heated by electrical current. Thermal evaporation must be an important technology for the formation of functional coatings on a variety of materials. However, there are limitations regarding the type of material that can be heated. In some cases such as ZrC, it is not possible to achieve the necessary evaporation temperatures without significantly evaporating the source holder. Moreover, chemical reactions between the holder and the material can result in the contamination of the coating.

### **2.2.2 Sputtering Deposition (S)**

In the sputtering process, the target material is bombarded with high energy ions that transfer their momentum to the atoms on the target materials which are ejected. These sputtered particles condense on the substrate facing the target. The dc or rf sputtering by an Ar plasma are the most common form. Because of the low sputter yield, magnetron sputtering is often used to increase the deposition rate. Magnets which are positioned behind the target induce the electrons to spiral and increase the degree of ionization of the plasma due to longer path length of electrons.

Alternatively, the configuration consisting of three Ar ions beams can be used to co-deposit ZrC film, which is called “tri-ion beam-assisted deposition (tri-IBAD)” [He98]. Two beams of Ar ions can be used to sputter from graphite and zirconium. A third Ar ion beam can be used to bombard the growing ZrC film to provide additional energy to enhance film formation processes.

Compared to evaporated particles, sputtered particles have considerably higher kinetic energies. As a result, sputtered layers usually have higher adhesive strength and a denser coating structure than evaporated layers. The greatest advantage of sputtering deposition is a large particle source area compared to evaporators, which enables a large area coating with a high degree of uniformity. Nevertheless, sputtering could have a relatively low ratio of energetic ions to neutral species, so that it is possible not to produce the hardest films.

### **2.2.3 Chemical Vapor Deposition (CVD)**

In chemical vapor deposition methods, the state of substances used for the growth is in the vapor phase when they are introduced to the vacuum system. The substances must be thermally excited by appropriate high temperatures or with plasma to be deposited. Chemical vapor deposition (CVD) of ZrC can be accomplished by the reaction between zirconium halide and a hydrocarbon in  $H_2$  atmosphere at temperatures above  $1000^\circ C$ . The zirconium halide vapor can be obtained either by a reaction between a halide vapor and zirconium metal, or by sublimation of  $ZrCl_4$ .

Nuclear fuel particles were coated with ZrC coatings by CVD [Rey74]. Argon (Ar) gas was initially bubbled through dichloromethane ( $CH_2Cl_2$ ) that was kept at  $0^\circ C$ . Then the Ar and  $CH_2Cl_2$  gas mixture was passed through a heated zirconium (Zr) “sponge” at  $600^\circ C$  to produce  $ZrCl_4$  vapors. Preheated methane ( $CH_4$ ) and hydrogen ( $H_2$ ) gases to

600 °C were mixed with the ZrCl<sub>4</sub> vapors inside a graphite tube and heated to 1100 °C for 3 hours to produce ZrC coatings. Chemical analysis of the coating resulted in a C/Zr ratio of 1.01 which indicated that some free carbon was present in the coatings.

The effect of the composition of gas mixtures on the properties of ZrC coatings was studied [Hol77 and Wag76]. Chemical vapor deposition of ZrC coatings was achieved by reacting gaseous mixtures of CH<sub>4</sub>, H<sub>2</sub>, ZrCl<sub>4</sub>, and Ar as carrier gas. The overall reaction is given by



Increasing the amount of CH<sub>4</sub> in the coating gas mixture (i.e., increasing C/Zr molar ratio) resulted in ZrC coatings with increased amounts of carbon. The chemical analysis of the coating showed the presence of free carbon, when the C/Zr molar ratio in the coating gas mixture was over 0.21.

Organometallic precursor (cyclopentadienylzirconium) was also used to deposit ZrC coatings at temperatures in the range of 300~600 °C [Han95]. The chemical composition of the films synthesized at 600 °C showed presence of zirconium carbide, as determined by x-ray photoemission spectroscopy (XPS).

#### **2.2.4 Pulsed Laser Deposition (PLD)**

The technique of pulsed laser deposition (PLD) has been used to deposit high quality films of various materials for more than two decades. The technique uses high energy laser pulses (typically 2~5 J/cm<sup>2</sup>) to melt, evaporate, and ionize material (ablation process) from the surface of a target. This ablation event produces a transient, highly luminous plasma plume that expands rapidly away from the target surface. The ablated material is collected, and then condenses on a suitably placed substrate.

Applications of the technique range from the superconducting films production and insulating circuit components to medical applications to improve biocompatibility. In spite of this widespread usage, the fundamental processes occurring during the transfer of material from target to substrate are not fully understood yet, and are consequently the focus of much research.

The interaction of laser radiation with solid surfaces was under investigation from as early as 1962, when Breech and Cross [Bre62] analyzed the emission spectrum of material vaporized by laser pulses. The first demonstration of PLD in 1965 [Smi65] did not attract significant interest, as the films were inferior to those obtained by other deposition techniques, such as chemical vapor deposition (CVD) or molecular beam epitaxy (MBE). The PLD technique was slowly developing for approximately the next twenty years until Dijkamp and Venkatesan [Dij87] used PLD to grow a film of the high temperature superconducting material  $\text{Ba}_2\text{Cu}_3\text{O}_7 + \text{YBaCuO}$  (YBCO). The films obtained were found to be superior in quality to those previously grown using other deposition methods and awaked a tremendous interest in the technique. Present day research applications include growing films for magneto-optic storage devices, developing multilayer devices for x-ray optics, and depositing diamond films on components for protection and insulation.

A schematic diagram of the basic PLD configuration is shown in fig. 2-3. The general understanding of the process is somewhat simple, which uses short pulses (pulse duration, 10~30 ns) of laser energy to remove material from the surface of a target. The vaporized material, containing neutrals, ions, and electrons, is known as a laser-produced plasma plume, and expands rapidly away from the target surface (velocities typically

$\sim 10^6$  cm/s in vacuum). Film growth occurs on a substrate upon which some of the plume material recondenses. However, in practice, the situation is not so simple, with a large number of variables affecting the properties of the film, such as laser fluence, background gas pressure and substrate temperature. These variables allow the film properties to be improved for individual applications. However, optimization can require a considerable amount of time and effort. Indeed, much of the early research into PLD concentrated on the empirical optimization of deposition conditions for individual materials and applications, without attempting to understand the processes occurring as the material is transported from target to substrate. The technique of PLD was found to have significant benefits over other film deposition methods. The capability for stoichiometric transfer of material from target to substrate, i.e., the almost exact chemical composition of a complex material such as YBCO, can be reproduced in the deposited film. Relatively high deposition rates ( $\sim 100$  Å/min) can be achieved at moderate laser fluences, with film thickness controlled in real time by simply turning the laser on and off.

The fact that a laser is used as an external energy source results in an extremely clean process without internal filaments. Thus deposition can occur in both inert and reactive background gases. The use of a carousel housing a number of target materials enables multilayer films to be deposited without the need to break vacuum when changing between materials. In spite of these significant advantages, industrial adoption of PLD has been slow and most applications have been limited to the research environment. There are basically three main reasons for this. First, the plasma plume created during the laser ablation process is highly forward directed; therefore the thickness of material collected on a substrate is highly non-uniform and the composition

can vary across the film. The area of deposited material is also quite small in comparison to that required for many industrial applications which require area coverage of at least  $\sim 8 \times 8 \text{ cm}^2$ . Second, the ablated material contains macroscopic globules of molten material, up to  $\sim 10 \text{ }\mu\text{m}$  diameter. The arrival of these particulates at the substrate is obviously detrimental to the properties of the film being deposited. Third, the fundamental processes occurring within the laser-produced plasmas are not fully understood. Thus deposition of novel materials usually involves a period of empirical optimization of deposition parameters. To a large extent the first two problems have been solved. Films of uniform thickness and composition can be produced by rastering the laser spot across the target surface and moving the substrate during deposition. Line-focus laser spots have also been used to obtain large area coverage. The particulate material was initially removed from the plume using a mechanical velocity filter, although recently more elaborate techniques, involving collisions between two plasma plumes or off-axis deposition, have been used to successfully grow particulate-free films. The third problem will be resolved by the development of computer simulations to describe PLD. However, a large amount of experimental data is required to support the verification of such models.

### **2.2.5 Comparison of Techniques**

Fig. 2-4 [Chr94] compares the energy range of the atomic fluxes for each technique. The solid boxes are typical values for the energy range of the atomic fluxes in practice, and the dashed boxes are the energetic fluxes values which could be controlled. The spread in energy of the atomic flux can be divided into energetic portion to the flux and thermal fluxes. The purely thermal techniques such as CVD (chemical vapor deposition) and MBE (molecular beam epitaxy) are mostly used so far because the energetic

deposition techniques are still under development. The shaded area in fig. 2-4 [Chr94] is the best energy range for deposition flux that was established earlier. Energy of 5 eV to 10 eV per atom promotes surface diffusion and high sticking probability while minimizing damage. The energetic flux over 100 eV can produce deep damage, so it should be avoided. The energy range of sputtering (S) and PLD matches most closely the best energy range indicated. Although the techniques with purely thermal fluxes are in standard use to deposit high quality epitaxial films, the energetic techniques can be employed to lower the growth temperature at which epitaxy can be achieved, especially for high melting temperature materials such as ZrC.

Fig. 2-5 [Chr94] shows the range of pressures in which each of the techniques is operable. PLD can relatively operate in a wide pressure range from UHV (ultra high vacuum) to 1 Torr, while other techniques need lower than HV (high vacuum) pressure to minimize contamination, to avoid oxidation of evaporation filaments, or to sustain plasma. Although most materials do not require performing the deposition in a high pressure of background gas, PLD has an advantage over other techniques in operating under high background gas pressure that is particularly useful for multicomponent oxides for example.

## **2.3 Growth and Factors Determining the Quality of Thin Films in PLD**

### **2.3.1 Nucleation and Growth**

The atoms accumulated on the surface may diffuse laterally over substrate, also they may encounter other mobile atoms to form mobile or stationary clusters, then they may attach to preexisting film-atom clusters, or they may be reevaporated from substrate [Ven84]. The balance between growth and dissolution processes will be governed by the total free energy of the cluster. Nucleation could be stabilized and destabilized,

depending on the energy stored in forming surface of new face, the adhesion energy released in formation of an epitaxial interface, the strain energy stored in lattice-mismatched epitaxial growth, and electrical energy stored in the formation of a surface dipole.

Three modes of film growth at the initial stages are possible [Lew78]. When the cohesive energy of the film atoms is greater than the cohesive binding between the film and substrate atoms, the formation and growth of isolated islands occur (Volmer-Weber Island growth) [Mah99]. This mode can result in an epitaxial film that has a rough surface, or a polycrystalline film. When the cohesive energy between the film and substrate atoms is greater than the cohesive energy of the film (but monotonically decreases as each film layer is added), layer by layer (Frank-Van der Merwe) growth occurs [Mah99]. This mode results in a very smooth epitaxial film. When the monotonic decrease in binding energy with each successive layer is energetically overridden by some factor such as strain energy, island formation becomes more favorable. So mixed (Stranski-Krastanov) growth, island growth after the first monolayer forms, can occur [Mah99].

The growth of thin films by PLD depends on many factors, such as energy, ionization degree, and type of the condensing particles, temperature, and physicochemical properties of the substrate. There are two main thermodynamic parameters that determine the growth mechanism. One is substrate temperature  $T$  and the other is supersaturation  $m$ .

$$m = kT \ln \frac{R}{R_e} \quad (2-2)$$

where  $k$  is the Boltzmann constant,  $R$  is the actual deposition rate, and  $R_e$  is equilibrium deposition rate at temperature  $T$ .

The overall film growth process in PLD has been theoretically studied [Met89]. The mean thickness at the moment of 99% covered substrate ( $N_{99}$  [Kas78]) at which a growing thin discontinuous film reaches continuity has been found to be given by

$$N_{99} = 0.5 \left( \frac{\nu N_0}{R} \right)^{1/3} \exp \left( \frac{-3E_{des} + 2E_{ad}}{3kT} \right) \quad (2-3)$$

where  $\nu$  is the adatom vibrational frequency,  $N_0$  is the density of adsorption sites on the substrate,  $E_{des}$  is the activation energy for adatom desorption, and  $E_{sd}$  is the activation energy of adatom surface diffusion. The lines of equal mean film thickness at the moment of 99% covered substrate (defined by the condition  $N_{99}(R, T) = \text{constant}$ ) can be drawn in  $\ln R$  versus  $1/T$  coordinates (fig 2-6).

One of line of equal mean film thickness at the moment of 99% covered substrate is drawn as dashed line. Depending on deposition rate and temperature, high-island growth region and low-island growth region are divided in the growth diagram. In the high-island growth region the thin film reaches continuity with a mean thickness. In the low-island growth region a mean thickness does not exceed a few monolayers. At higher  $R$  and lower  $T$ , continuous growth (amorphous) takes place from island growth [Kas78].

Therefore depending on the experimental conditions, such as energy density of laser and substrate temperature, single crystalline thin film in high-island growth region, polycrystalline film in low-island growth region, or amorphous film can be formed.

### 2.3.2 Background Gas

During pulsed laser deposition, the use of background gas can be divided into passive or active use. The passive use is mostly to compensate for some loss of a

constituent element. For examples, the deposited oxides tend to be deficient in oxygen. Typically 10~300 mTorr of background oxygen in chamber is required for oxide superconductors.

Also the introduction of background gas change typical particulate size as the ambient gas pressure varies. Inert or reactive gas can be introduced to form particulates with a desired size or composition for active use of ambient gas during PLD. The decrease in the ambient gas pressure results in a decrease in size and a narrower size distribution [Mat86].

The origins of the formation of the particulates and the mechanisms of enrichment in specific element in the particulates are different in vacuum and in inert ambient gas for PLD processes. The effect of inert ambient gas pressure increases collisions between the ejected species and the ambient gas as the pressure increases. At a pressure of 1 mTorr, the mean free path is about 5 cm. The mean free path of ejected species becomes 0.05cm at a higher pressure of 100 mTorr. In vacuum, there are no collisions between ejected species virtually, so particulates are predominantly formed from solidified liquid droplets, and the vapor species are deposited as a uniform background film in the same time.

However, when the ambient gas pressure increases, the vapor species can have enough collisions. Thus, nucleation and growth of vapor species can occur, before they arrive at the substrates. This suggests that the ultrafine particulates are formed from the vapor species instead of liquid droplets.

### **2.3.3 Vacuum**

The quality of the vacuum is a major consideration for determining the deposition rate. Gaseous impurities in the deposition chamber impinge on the growing film and will be incorporated into the film depending on their sticking probabilities. The most common

impurities are H<sub>2</sub>O, CO, CO<sub>2</sub>, and H<sub>2</sub>. Fig. 2-7 [Chr94] indicates the relationship between atomic fluxes on surface with pressure and deposition rate. To avoid contamination of impurities, deposition rate should be controlled depending on deposition pressure.

#### **2.3.4 Laser Fluence**

The laser fluence is most significant on the particulate size and density. The laser fluence can be changed varying the laser power or the laser spot size. There is threshold laser fluence to ablate target material with laser beam. For example, in the case of ZrC, the threshold laser influence is about 1.3 J/cm<sup>2</sup> [Ale00]. The laser fluence is extrapolated and a linear trend up to 13 J/cm<sup>2</sup> is maintained (fig. 2-8 [Ale00]). In other word, the saturation of ablation process is not observed. One of the mechanisms that reduce the ablation rate is plasma shielding of the target [Dye89], and it is more often encountered in the laser-ablation deposition using longer wavelength.

#### **2.3.5 Laser Wavelength**

The laser wavelength is directly related to the effectiveness of the absorption of the laser power into the target. For most metals, the absorption coefficient decreases with decreasing laser wavelength. Thus, the laser penetration depth in metal is larger in the UV range than in the infrared range. For other materials, the variation of absorption coefficient with wavelength is more complex due to various absorption mechanisms, such as lattice vibration, free carrier absorption, impurity centers, or bandgap transition.

The primary effect of the laser wavelength on particulate generation is mostly due to the difference in the absorption coefficient when different laser wavelength is used. Larger particulates are generated when using longer laser wavelength [Kau90].

### **2.3.6 Target to Substrate Distance**

The effect of target to substrate distance is mainly reflected in the angular spread of the ejected flux. Depending on the position of the substrate, different particulate appearance may occur. The specific effects of target to substrate distance and ambient pressure are related. The plume dimension decreases as the background gas pressure increases due to the increased collisions between the laser-produced plume and the background gas. When the target to substrate distance is smaller than the plume length, there is no remarkable difference in particulate size and density. As the target to substrate distance increases, a few larger particulates appear [Chr94].

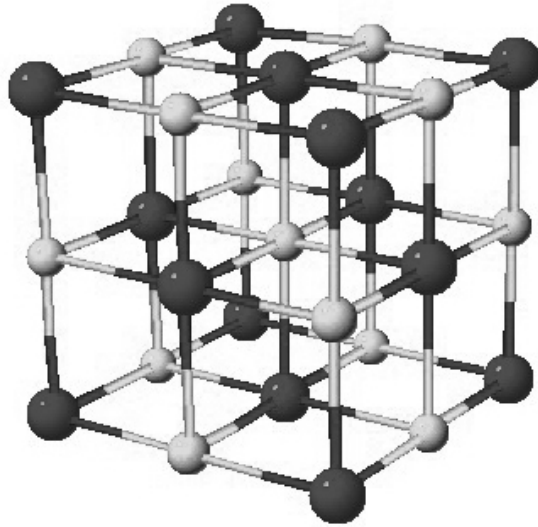


Figure 2-1. Image of cubic rocksalt (B1) structure of transition metal carbides. Carbon atoms are depicted as the light gray spheres, metals as dark gray spheres.

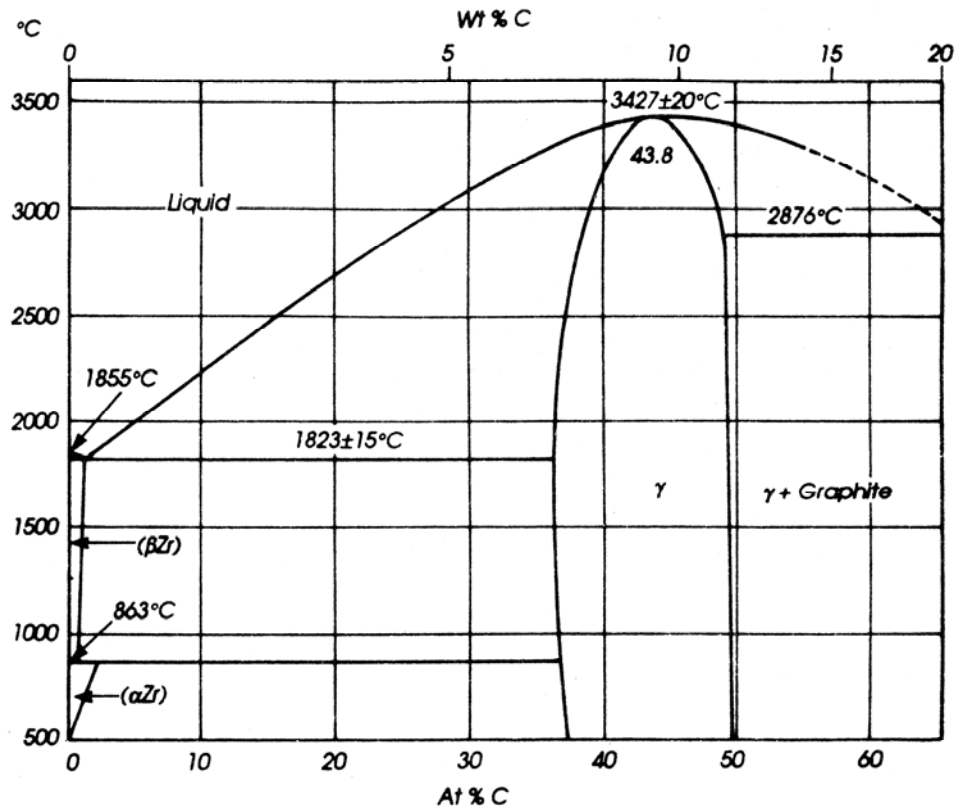


Figure 2-2. Zr-C phase diagram showing wide range congruent compositions [Bra92].

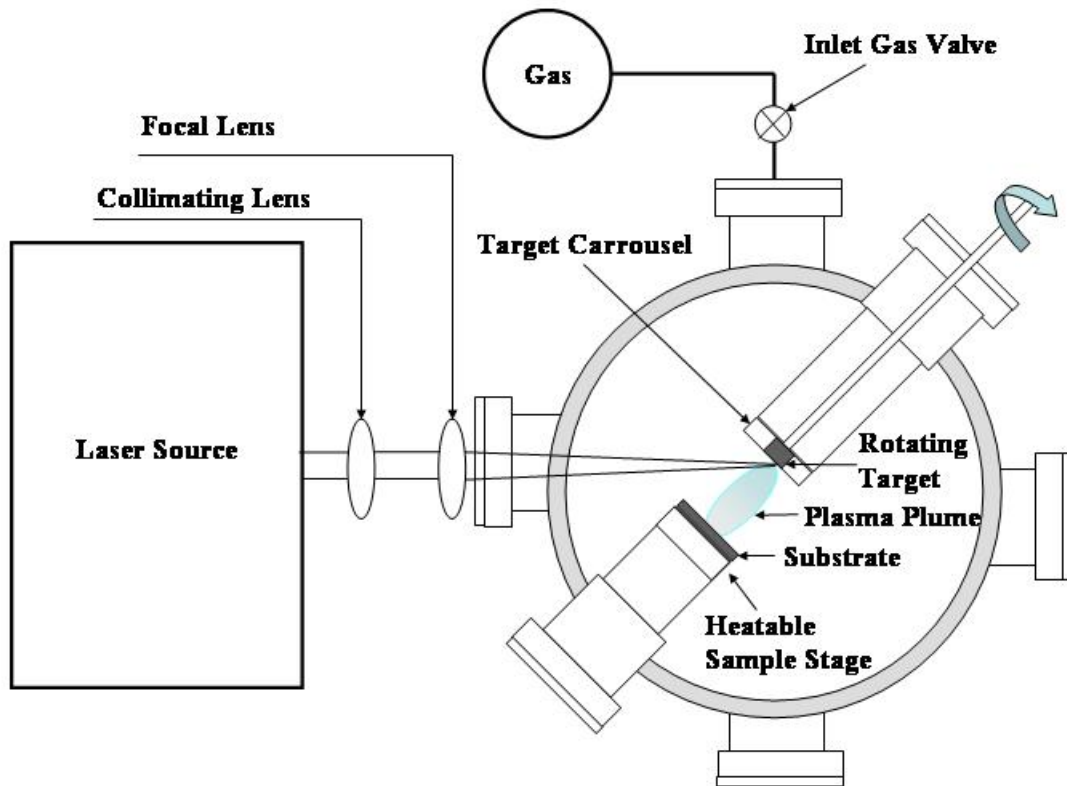


Figure 2-3. Schematic diagram of an apparatus for pulsed laser deposition.

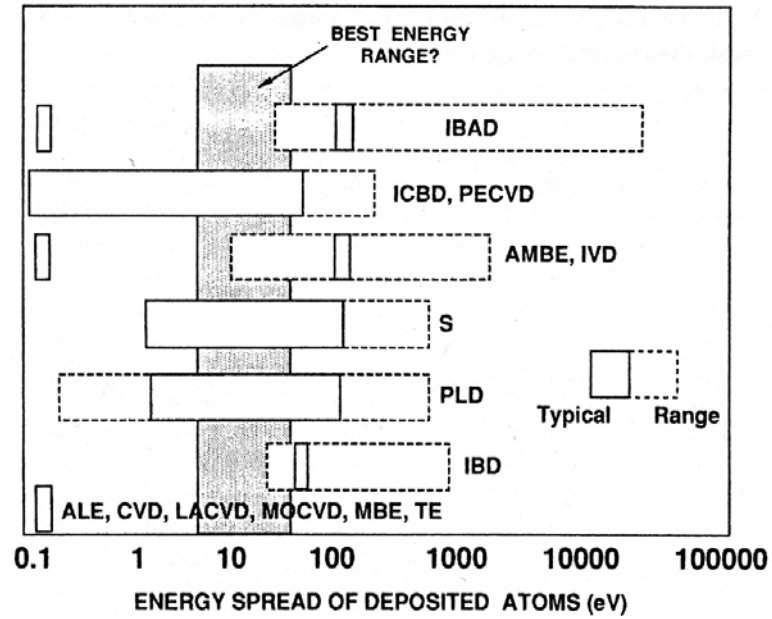


Figure 2-4. Schematic diagram of the approximate energy range of deposited atoms for various deposition techniques. The shaded box indicates the supposed energy range of atom fluxes considered to be beneficial for film growth [Chr94].

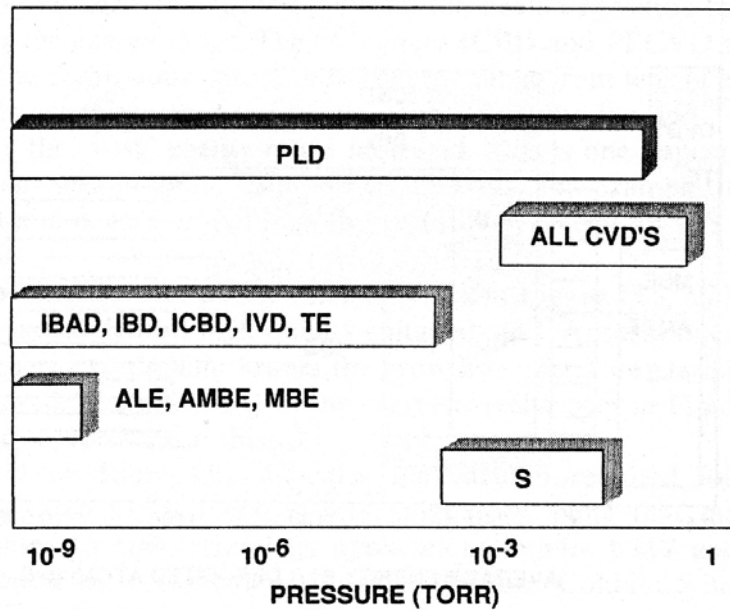


Figure 2-5. Schematic diagram comparing the pressure ranges over various techniques. PLD can operate over the widest range of all the methods [Chr94].

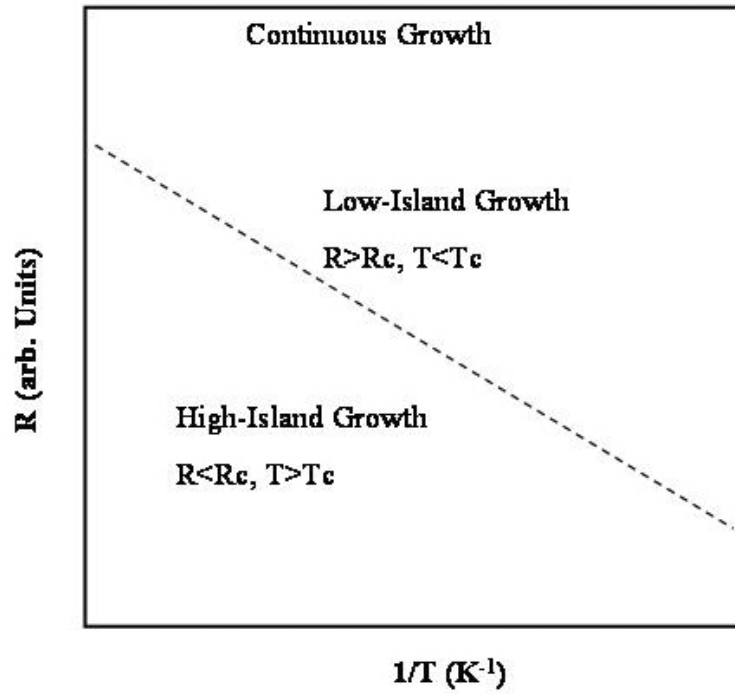


Figure 2-6. Growth diagram drawn by equation 2-3, showing the dependence of growth behavior on temperature and growth rate.

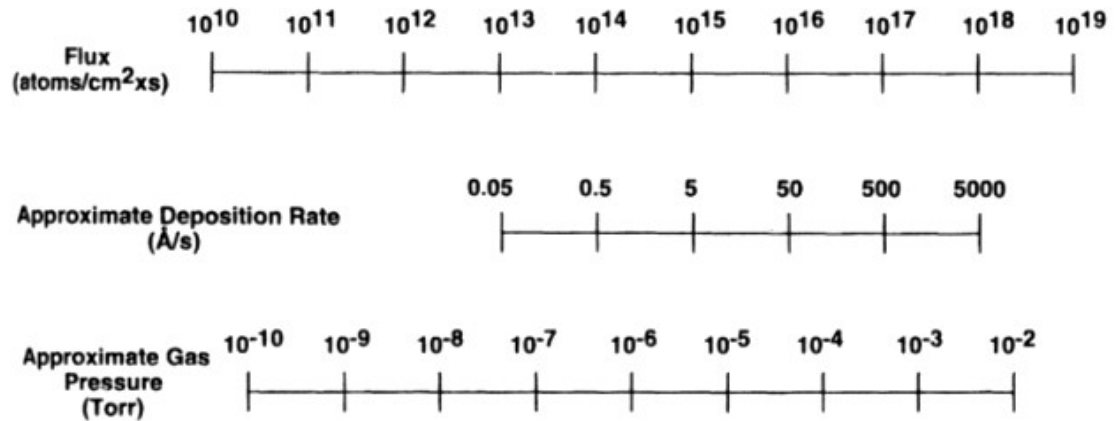


Figure 2-7. Relationship of impinging particles fluxes to deposition rate, and gas pressure [Chr94].

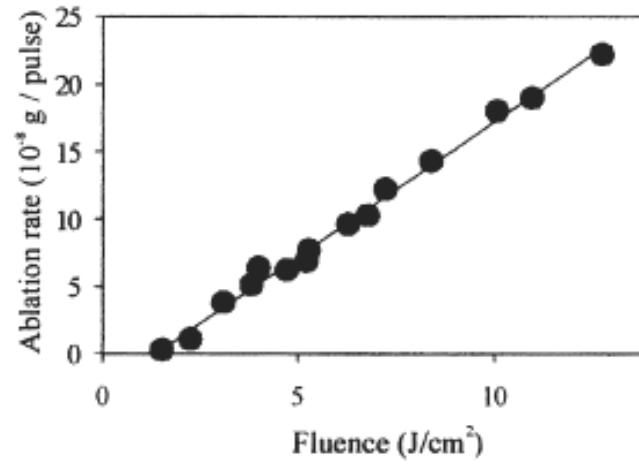


Figure 2-8. ZrC ablation rate, showing linear dependence on laser fluence, and threshold laser fluence of 1.3 J/cm<sup>2</sup> [Ale00].

CHAPTER 3  
EXPERIMENTAL METHODS

**3.1 Pulsed Laser Deposition System**

Most depositions are conducted using the laser wavelength of 193~400 nm because strong absorption is exhibited in this spectral region by target materials. Absorption coefficients have a tendency to increase as laser wavelength is shorter in this range. The excimer laser wavelengths used in a commercial laser system are listed in table 3-1. A Lambda Physik KrF laser ( $\lambda = 248$  nm) was used for the experiments in this study with a 25 ns pulse duration.

Table 3-1 Excimer laser operating wavelengths

Excimer	Wavelength (nm)
F2	157
ArF	193
KrCl	222
KrF	248
XeCl	308
XeF	351

A schematic diagram for chamber was illustrated in fig. 2-3. A stainless steel spherical vacuum chamber is used. The laser entry port is protected by a quartz plate, which is designed to reduce the deposition rate of materials on window. The angle between the target normal and laser beam is  $45^\circ$ . A turbo-molecular pump backed by a

mechanical pump provided the high vacuum. The system operated between  $2.5 \times 10^{-6}$  and  $1.5 \times 10^{-7}$  Torr of base pressure, which is critical factor in controlling the quality of film.

### 3.2 Structural Characterization

Symmetric and asymmetric x-ray diffraction spectra (XRD) were collected on a Panalytical MRD X'pert system using Cu K $\alpha$  radiation to identify crystal structure and quality. The standard settings for the X-ray generator were 45 kV at 40 mA.

Fig. 3-1 compares the grazing incidence angle geometry used for thin film with the conventional  $\theta$ - $2\theta$  symmetric geometry used for bulk analysis. In the grazing incidence XRD geometry for the thin film arrangement, the incident and diffracted beams are prepared nearly parallel using a mirror and a narrow slit on the incident beam ( $1/8^\circ$  divergence slit for experiments of this study) and a parallel plate collimator ( $0.27^\circ$  divergency) on the detector side. In addition, a very small angle of incidence beam to the sample surface (typically  $1^\circ$  to  $3^\circ$ ) increases the path length of the X-ray beam through the film. This increases the diffracted beam intensity from the film, while that from the substrate is reduced. During the collection of the diffraction spectrum, only the detector moves along the angular range, while keeping the incident angle fixed. Thus the beam path length and the irradiated area are constant.

For more detail observation of highly textured ZrC thin films, omega rocking curves were collected. The geometry is represented in fig. 3-2. The peak broadening along  $\theta$ - $2\theta$  direction is caused by variation in d-spacing with depth for thick films or by use of non-monochromatic beam. On the other hand, the peak broadening in omega direction is due to mosaic spread, lateral incoherence, high uniform dislocation density, or sample curvature.

Also pole figure method was used to confirm not only in-plane texture, but also out-of-plane texture as well as crystal quality and orientation relationship between film and substrate. A schematic diagram of pole figure geometry and relation with microstructure are shown in fig. 3-3. The incidence beam angle and diffracted beam angle is set to specific angle which is satisfying Bragg's law. All of reflections in projection area are from specific faces at the Bragg angle, but the geometry of the sample is changing by rotation and by tilting during scanning. Thus, we can obtain the orientation distribution.

### **3.3 Film Thickness and Roughness**

For the measurement of film thickness and roughness, mainly x-ray reflectometry (XRR) was employed and compared with spectroscopic ellipsometry (SE, Woollam M-88). XRR method is to record the intensity of the x-ray beam reflected by a sample at grazing angles. The operation mode is the same as regular powders XRD setup which always make the incident angle half of the angle of diffraction. The reflection at the surface and interfaces is due to the different electron densities in the different layers in film, which correspond to different refractive indexes.

For incident angles  $\theta$  below a critical angle ( $\theta_c$ ), total external reflection occurs. The critical angle for most materials is less than  $0.3^\circ$  in  $\theta$ . Above  $\theta_c$ , the reflections from the different interfaces interfere and give rise to interference fringes. The period of the interference fringes and their decrease in intensity are related to the thickness and the roughness of the layers. The reflection spectra can be analyzed with the aid of the WinGIXA software, which is based on the Parratt formalism modified to include roughness [Par54 and Név80]. The typical ranges for these measurements are between  $0.1^\circ$  and  $5^\circ$  in  $2\theta$ . For the detail analysis of x-ray reflection, WinGixa software was used

for fitting x-ray reflection curves. To get an accurate fit for the acquired data, a three layers model was used, which consists of a topmost contamination layer, then the deposited layer, and an interfacial layer located between the deposited layer and substrate. The measurable ranges and resolution for this measurement are listed in table 3-2 [Auc01].

Table 3-2 Typical XRR values for the resolution and ranges.

Parameter	Resolution	Range
Thickness	$\pm 0.1\sim 5\%$	2~200 nm
Surface roughness	$\pm 0.2$ nm	0.1~3 nm
Interface roughness	$\pm 0.2$ nm	0.1~3 nm
Density	1-10%	-

Atomic force microscope (AFM) images were taken with a Digital Instruments Dimension 3100. Images were acquired in the tapping mode with a scan range  $5 \times 5 \mu\text{m}$ . Before roughness analysis was performed, an automatic ‘plane fit’ and a ‘flatten’ command were applied to the images to level the image and to reduce slope associated with measurement drift.

### 3.4 Surface Chemistry Analysis

For Auger electron spectroscopy (AES) investigation, a Perkin-Elmer PHI 660 instrument was used for the surface analysis. Survey spectra were obtained from as-deposited film, also after removing the topmost layer by Ar ion sputtering. X-ray photoelectron spectroscopy (XPS) spectra were acquired on a PHI model 5100 ESCA system using Mg  $K\alpha$  X-ray source (1253.6 eV). Argon ion was used to remove surface contaminants and to remove atomic layers into the thin films. The multiplex data were used during peak deconvolution. Background was subtracted, and peaks were fitted with

one or more component Gaussian-Lorentzian functions to determine accurate chemical bonding.

### 3.5 Electrical Measurement

The electrical measurement was taken on an Alessi four point probe. A probe head having tungsten carbide tips with a point radius of 0.002" and a probe spacing of 0.05" was used for all measurements. Current was supplied by a Crytronics model 120 current source with a range of applied currents between 30  $\mu\text{A}$  to 100  $\mu\text{A}$ . Eq. (3-1) was used to determine resistivity ( $\rho$ ,  $\Omega\cdot\text{cm}$ ).

$$\rho = \frac{4.5324 \times V \times t}{I} \quad (3-1)$$

Based on the dimensions of the sample and probe head, no geometrical correction factors were applied. The term  $t$  is film thickness (cm), and  $V$  is the voltage measured at the supplied current ( $I$ ).

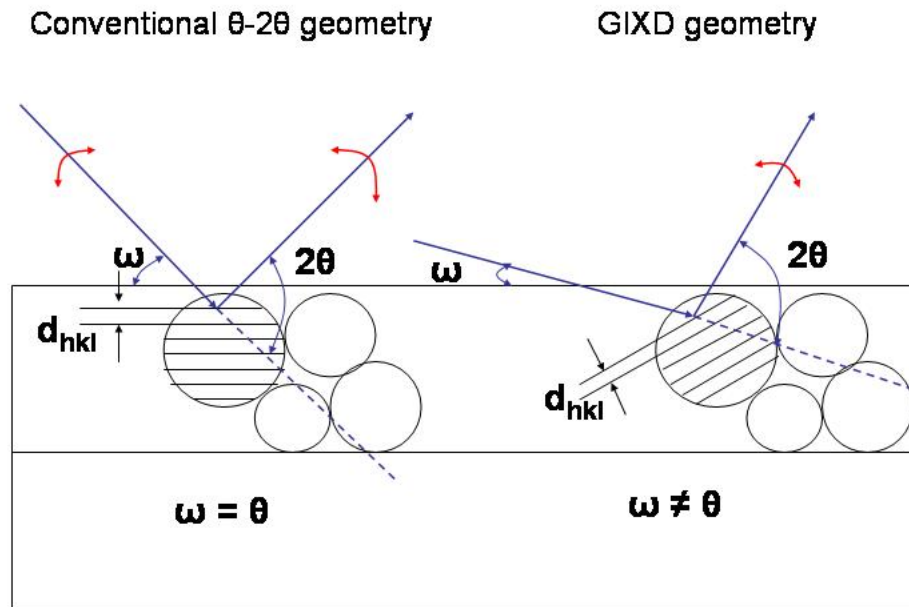


Figure 3-1. A schematic diagram of symmetric and asymmetric GIXD geometry.

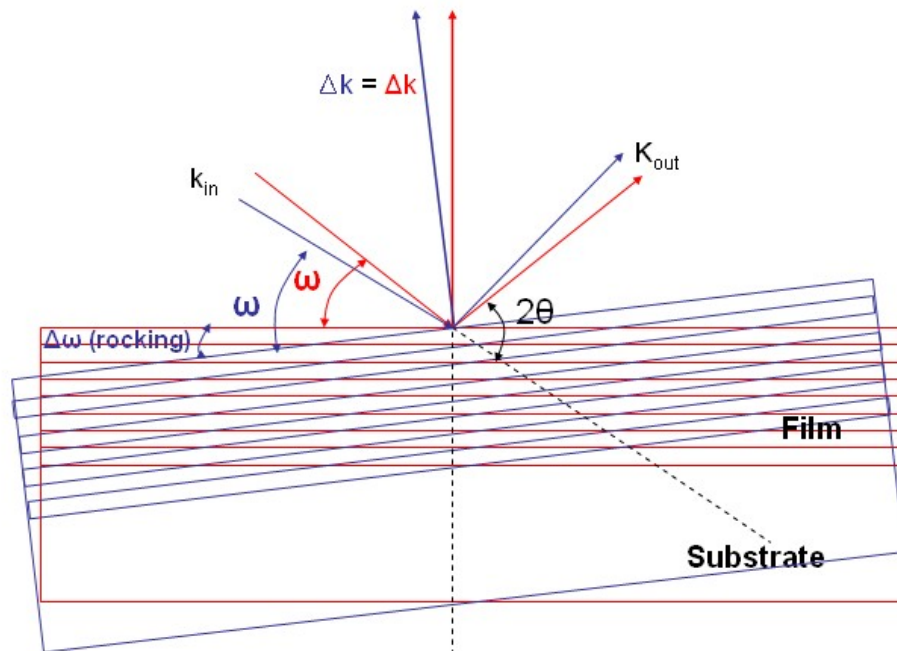


Figure 3-2. A schematic diagram of omega rocking curve geometry.

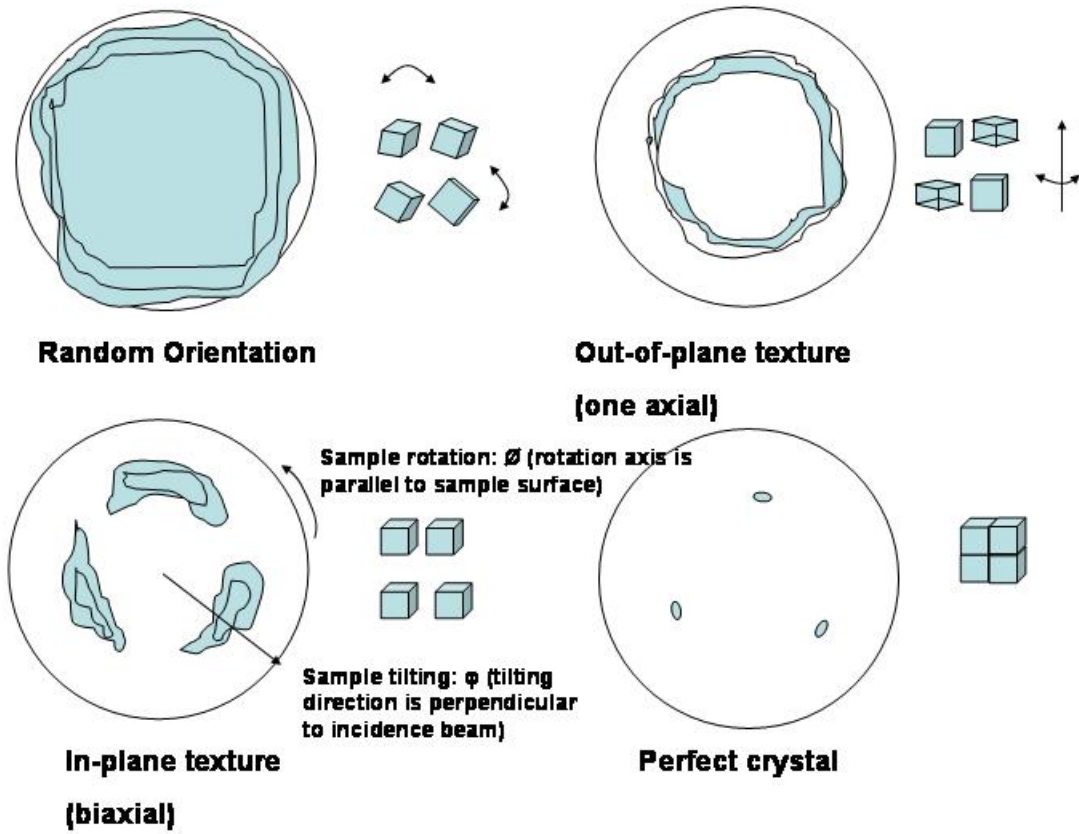


Figure 3-3. An example of a schematic reflections on pole figure related to crystal quality.

CHAPTER 4  
GROWTH AND CHARACTERIZATION OF HIGH CRYSTALLINE QUALITY  
ZIRCONIUM CARBIDE FILMS

**4.1 Introduction**

Zirconium carbide (ZrC) is a refractory compound, characterized by a high melting temperature of 3530 °C [Zai84], excellent thermal stability, high mechanical hardness and strength [Che05a], and chemical inertness. In addition, electrical conductivity is comparable to metals [Zai84], and work function for electron emission is low [Mac95]. The common applications are the chemical- and wear-resistant coating, and ultra-high temperature applications. Thin films of ZrC also have important application in vacuum electronics or micromechanics [Xie96, Tem99, and Cha01]. Particularly, the epitaxial growth of ZrC is specially important because it could allow the growth of various types of nanostructure by using anisotropic etching, that would exhibit high performance, efficiency, and compactness, such as short response and high brightness flat displays, and electron beam lithography. ZrC also exhibits lower lattice mismatch and thermal expansion coefficient difference with Si than ZrN, making it a potential good candidate for metallization or diffusion barriers structures for Si-based electron devices. Despite of the considerable attractive applications, relatively few studies describing ZrC film growth have been published so far. The growth of ZrC film by thermal evaporation [Tes93], reactive magnetron sputtering deposition [Brü93], vacuum plasma spray process [Var94], chemical vapor deposition (CVD) [Ber95], pulsed laser deposition (PLD) [Ale00], and tri-ion beam-assisted deposition [He98] has been reported. However, it seemed to be

quite difficult to obtain high crystalline quality ZrC films, because of its high melting temperature, low vapor pressure, and Zr atoms affinity for oxygen. Pulsed laser deposition (PLD) is recognized as a techniques that can overcome these difficulties with respect to other techniques. PLD was successfully employed to grow high crystalline ZrC films in this study. By optimizing the deposition conditions, epitaxial ZrC films on silicon and sapphire substrate were obtained. The structure, stoichiometry, and optical and electrical properties of these films are described in this chapter.

## 4.2 Experiment

The film depositions were conducted in an all-metal vacuum chamber using a KrF excimer laser ( $\lambda=248$  nm). First of all, experiments were focused on studying the effects of growth conditions (or process parameters) on the deposited films. Especially an effort was made for growing crystalline ZrC films. Within the range of 2 ~ 10 J/cm<sup>2</sup> laser fluences with 5 Hz laser pulse repetition rate, the ZrC films were deposited on Si (001) at the temperature range of 200 ~ 700 °C. Si (001) substrates were cleaned chemically by acetone, methanol, and rinsed in de-ionized water in turn, then dipped in 1 % HF solution for 1 min, blown dry by high purity nitrogen gas, and immediately loaded into the deposition chamber. Depositions were performed under residual vacuum or a low C<sub>2</sub>H<sub>2</sub> atmosphere. The study was continued to produce high quality films by optimizing growth parameters and to study growth behavior on various substrates. At this time, special care was taken to maintain low water vapor pressures below  $\times 10^{-8}$  Torr during depositions, as measured with a residual gas analyzer (RGA) attached to the deposition chamber. Additionally, Si substrates were heated to 900 °C and maintained for 20 min under high vacuum to remove the passivation layer on the substrate. The laser parameters used were 10 J/cm<sup>2</sup> fluences and 10 Hz repetition rate at substrate temperatures around 750°C.

The films surface and interfacial roughness, mass density and thickness were obtained by simulating the measured x-ray reflectivity (XRR) spectra acquired with a Panalytical X'Pert MRD system. The same instrument was used for structural characterization in symmetric and grazing incidence x-ray diffraction (XRD and GIXD). Pole figure measurements were acquired both from the films and substrates for texture characterization. Omega rocking curve method was used to evaluate quality of epitaxial films. The thickness and optical properties of the films were measured by spectroscopic ellipsometry (SE, Woollam M-88). The chemical composition of the films was investigated by Auger electron spectroscopy (AES, Perkin-Elmer PHI 660). To analyze the bonding structure of ZrC, X-ray photoelectron spectroscopy (XPS, Perkin-Elmer PHI 5100 ESCA) was used. Focused Ion Beam (FIB) Strata DB 235 technique was employed to make cross-sectional samples for high resolution transmission electron microscopy. Bright field image and electron diffraction pattern were obtained from high resolution JEOL TEM 2010F to analyze microstructure and quality of deposited thin films. Details of each experiment are described in chapter 3.

### **4.3 Results and Discussion**

#### **4.3.1 Laser Fluence and Temperature Effect on Deposited Films**

ZrC films were deposited on Si (001) substrates to study the effect of substrate temperatures and laser fluences on the grown films. The films were grown for 20 minutes at various growth conditions, which resulted in estimated thickness around 400 Å. The deposited films were analyzed by surface sensitive grazing incidence XRD, and the results at 1° of an incidence beam angle are displayed in fig. 4-1. The growth conditions of the films are listed in table 4-1. Under low temperature conditions of 200 ~ 600 °C and/or low laser fluence range of 2 ~ 6 J/cm<sup>2</sup>, GIXD spectra did not show any diffraction

peak (ZC05 and ZC06 in fig. 4-1), indicating that the deposited films under these conditions were amorphous. By increasing the laser fluence to 8 J/cm<sup>2</sup> and substrate temperature at 600 °C, the deposited films started to show some crystallinity (ZC11 in fig. 4-1).

Table 4-1. Growth conditions of deposited films, showing GIXD spectra in fig. 4-1.

	Pressure during deposition	Substrate temperature	Laser fluence	Repetition rate
ZC06	1×10 <sup>-3</sup> Torr C <sub>2</sub> H <sub>2</sub>	500 °C	6 J/cm <sup>2</sup>	5 Hz
ZC05	1×10 <sup>-5</sup> Torr C <sub>2</sub> H <sub>2</sub>	600 °C	3 J/cm <sup>2</sup>	5 Hz
ZC11	1×10 <sup>-5</sup> Torr C <sub>2</sub> H <sub>2</sub>	600 °C	8 J/cm <sup>2</sup>	5 Hz
ZC24	1×10 <sup>-4</sup> Torr C <sub>2</sub> H <sub>2</sub>	600 °C	10 J/cm <sup>2</sup>	5 Hz
ZC26	8.5×10 <sup>-4</sup> Torr C <sub>2</sub> H <sub>2</sub>	600 °C	10 J/cm <sup>2</sup>	5 Hz
ZC25	1×10 <sup>-4</sup> Torr C <sub>2</sub> H <sub>2</sub>	700 °C	10 J/cm <sup>2</sup>	5 Hz

When the ZrC target was not pre-ablated for at least 1 min, GIXD pattern (incidence beam angle = 1°) of as-grown films in fig. 4-2 (a) showed some additional diffraction peaks other than those obtained from target in fig. 4-3, which were crystalline with diffraction lines corresponding to cubic and stoichiometric ZrC ( $a_0 = 4.69 \text{ \AA}$ , JCPDS PDF# 35-0784 [Pcp94]). Those additional diffraction peaks (vertical solid lines) in as-grown films were assigned to substoichiometric ZrC<sub>0.7</sub> compound ( $a_0 = 9.38 \text{ \AA}$ , cubic (space group: P), JCPDS PDF# 32-1489 [Pcp94]), which was probably caused by the oxidation of target surface. So the target was pre-ablated for 1 min hereafter, ahead of the growth processes to remove any surface oxide layer on target. Resulting GIXD spectra in fig. 4-2 (b) showed a stoichiometric Zr<sub>1</sub>C<sub>1</sub> compound (JCPDS PDF# 35-0784 [Pcp94]),

which is indicated as dashed vertical lines. In addition, it should be mentioned here that a low pressure ( $\times 10^{-5} \sim \times 10^{-3}$  Torr) of acetylene ( $C_2H_2$ ) gas was used as background gas for this study because GIXD spectrum from a film deposited at low  $C_2H_2$  atmosphere in fig. 4-4 showed a little improvement of crystallinity in the film. Other deposition conditions except background gas pressure were all same ( $T_s=600$  °C,  $8J/cm^2$ , and 5Hz).

At laser fluence at  $10 J/cm^2$ , resulting deposited films showed better crystallinity, evidenced by clear peaks in GIXD spectra (ZC24, ZC25, and ZC26 in fig. 4-1). All observed the diffraction lines corresponded to a stoichiometric cubic ZrC (JCPDS PDF# 35-0784 [Pcp94]), which were identical to those from the pure ZrC target in fig. 4-3. The crystallinity of the films deposited at higher substrate temperature was much improved at laser fluence of  $10 J/cm^2$  (from ZC24,  $600$  °C to ZC25,  $700$  °C in fig. 4-1). Therefore it is apparent that the deposition of crystalline films requires the simultaneous use of high substrate temperatures and high laser fluences.

#### **4.3.2 Deposition Rate and Thickness Uniformity of Deposited Films**

The effect of deposition time was investigated on density and roughness of the ZrC film grown on silicon (001) substrate at  $700$  °C under residual vacuum ( $1 \times 10^{-6}$  Torr) for 7, 14, and 20 min. The used laser parameters were  $10 J/cm^2$  fluence, and 5 Hz repetition rate. The layer thicknesses and roughness of these films were extracted by fitting the acquired x-ray reflectivity (XRR) spectra using the WinGIXA software from Panalytical, which is based on the Parratt formalism modified to include roughness [Par54 and Név80]. Instead of using only one ZrC layer model for fitting, a three-layer model was used that resulted in a better fitting: an interfacial layer, a ZrC layer, and a contaminated surface layer such as oxygen and hydrogen oxide. Also, thicknesses measured by spectroscopic ellipsometry were compared with those obtained by XRR data. From the measured x-ray reflectivity

spectra in fig. 4-5, the critical angles indicating the density of films [Rus02 and Zab94] were quite similar for all deposited films, and as high critical angle indicated ( $\theta_c \sim 0.35$ ), high density values around  $6.7 \text{ g/cm}^3$  were obtained. The thickness, roughness, and density parameters obtained from x-ray reflectivity curves are listed in table 4-2. The thickness change of deposited film was linearly time dependent as shown in fig 4-6. The average deposition rate was  $0.34 \text{ \AA/sec}$  (or  $0.068 \text{ \AA / pulse}$ ). This was a rather low deposition rate for PLD, implicating rather low vaporized ZrC concentration in a plasma plume.

Table 4-2. Thickness, density, and surface roughness values of the ZrC films deposited at  $700 \text{ }^\circ\text{C}$  for different times.

Deposition time (min)			7	14	20
XRR	Surface layer ( $\text{ZrC}_x\text{O}_y$ )	Thickness ( $\text{\AA}$ )	17	18	18
		Roughness ( $\text{\AA}$ , rms)	3.3	5.3	5.3
	ZrC layer	Thickness ( $\text{\AA}$ )	127	297	376
		Density ( $\text{g/cm}^3$ )	6.74	6.69	6.73
	Interfacial layer	Thickness ( $\text{\AA}$ )	0.6	2.3	2.0
Ellipsometry	Surface layer	Thickness ( $\text{\AA}$ )	10	10	9
	ZrC layer	Thickness ( $\text{\AA}$ )	125	310	382
	Interfacial layer	Thickness ( $\text{\AA}$ )	1.0	1.5	1.0

The GIXD (incidence angle  $\omega = 1^\circ$ ) spectra of these films shown in fig. 4-7 indicate that all crystalline orientations are present in the films. The intensities of these peaks slightly increased with an increase of thickness, indicating some increase in the volume of the randomly oriented grains. However, these diffraction peaks did not appear in the corresponding symmetric XRD spectra displayed in fig. 4-8, that is, the amount of these randomly oriented grains was rather small. According to the XRD results (fig. 4-8),

the deposited films under this condition grew with a (001) texture. It is also clear that, based on XRR data from table 4-2, there are no significant changes in the film density or surface morphology when the deposition time was changed.

The thickness uniformity of the deposited films was checked by acquiring XRR spectra at various positions from the same samples that were grown under identical condition. According to the data extracted from these XRR spectra, a ZrC film thickness uniformity of around 5% in the central  $1.5 \times 1.5 \text{ cm}^2$  area of the deposited film was estimated.

Table 4-3. Degree of out-of-plane texture of ZrC films at various growth conditions.

Substrate	ID	P <sub>0</sub> (Torr)	P <sub>d</sub> (Torr)	T <sub>s</sub> (°C)	Texture	FWHM (Omega-Rocking)
Si (001)	ZC202	$3.0 \times 10^{-7}$	$6.2 \times 10^{-6} \text{ C}_2\text{H}_2$	775	(001)	2.53
	ZC104	$2.6 \times 10^{-6}$	$1.2 \times 10^{-5} \text{ C}_2\text{H}_2$	750	(001)	3.37
	ZC103	$2.4 \times 10^{-6}$	$4.0 \times 10^{-6} \text{ C}_2\text{H}_2$	750	(001)	4.47
	ZC208*	$1.5 \times 10^{-7}$	$2.2 \times 10^{-6} \text{ CH}_4$	750	(001)	4.62
	ZC106	$9.0 \times 10^{-7}$	$1.0 \times 10^{-5} \text{ C}_2\text{H}_2$	750	(001)	5.45
Si (111)	ZC104	$2.6 \times 10^{-6}$	$1.2 \times 10^{-5} \text{ C}_2\text{H}_2$	750	$I_{111}/I_{200}=9.08$	4.82
	ZC107	$8.0 \times 10^{-7}$	$6.7 \times 10^{-6} \text{ C}_2\text{H}_2$	750	1.3	-
	ZC210*	$1.4 \times 10^{-7}$	$9.0 \times 10^{-7} \text{ CH}_4$	750	-	-
	ZC208*	$1.5 \times 10^{-7}$	$2.2 \times 10^{-6} \text{ CH}_4$	750	-	-
Sapphire (0001)	ZC107	$8.0 \times 10^{-7}$	$6.7 \times 10^{-6} \text{ C}_2\text{H}_2$	750	(111)	0.46
	ZC104	$2.6 \times 10^{-6}$	$1.2 \times 10^{-5} \text{ C}_2\text{H}_2$	750	(111)	0.68
	ZC208*	$1.5 \times 10^{-7}$	$2.2 \times 10^{-6} \text{ CH}_4$	750	(111)	2.31
	ZC204	$1.3 \times 10^{-7}$	$7.2 \times 10^{-6} \text{ C}_2\text{H}_2$	755	(111)	2.53

\* Titanium was contaminated unintentionally for (\*) marked samples.

### 4.3.3 ZrC Films Growth at High Temperature and High Laser Fluence

In this section, ZrC film growth was carefully controlled at higher substrate temperature and higher laser fluence growth conditions based on previous study. Also films were deposited on Si (001), Si (111), and sapphire (0001) single crystal substrates at high temperatures around 750 °C to investigate texture, quality, and properties of grown films. The representative growth conditions and results used for ZrC films growth are presented in table 4-3. Special care was taken to maintain low water vapor pressures during depositions by monitoring partial residual gas pressure. Also the Si substrates were heated up to 900 °C and maintained for 20 min under high vacuum to remove the passivation layer on the substrate before deposition.

Table 4-4. Structure information of ZrC , Si, and sapphire and lattice mismatch.

	ZrC	Silicon	Sapphire
Unit Cell	Cubic (NaCl)	Cubic (Dia.)	Rhom. (Hex.)
Space Group	Fm3m (225)	Fd3m (227)	$R\bar{3}c$ (167)
Lattice Parameter (Å)	4.6930 (JCPDS PDF#: 35-0784) [Pcp94]	5.4309 (JCPDS PDF#: 27-1402) [Pcp94] 5.4449 (750 °C) [Yim74]	a = 4.7592, c = 12.992 (JCPDS PDF#: 43-1484 ) [Pcp94] a = 4.7828 (750 °C) [Yim74]
Lattice mismatch (%) with ZrC	-	13.59 at RT 13.41 at 750 °C ( $a_{ZrC} < a_{Si}$ )	39.45 at RT 39.41 at 750 °C (calculated with $<110>_{ZrC}$ , $a_{ZrC} <110> > a_{Sapphire}$ )

Structural information for ZrC and substrates is presented in table 4-4, and the lattice mismatch is calculated with respect to the substrates. For sapphire, since its basal plane has same geometry as ZrC (111) plane, lattice mismatch was calculated with  $<11\bar{2}0>$  of sapphire parallel to  $<110>$  of ZrC. Lattice mismatches to Si and sapphire are

13.4 % and 39.4 %, respectively. For such a large lattice mismatch, definitely elastic theory can not be applied for epitaxial growth because critical thickness for that big mismatch will be less than 2 Å [Hu91]. However, the resulted grown films on Si and sapphire were epitaxial. This epigrowth of ZrC could be explained by ‘coincidence-site lattice (CSL)’ or ‘translational symmetries’ assumptions [Zur84]. The details were investigated by X-ray techniques and TEM, and oxidation problem was also considered in this section. In addition, electrical resistivity of these films was measured.

#### **4.3.3.1 Growth behaviors of ZrC films deposited on Si and sapphire substrate**

In fig. 4-9, symmetric theta-2theta XRD spectra acquired from the films (ZC104 samples in table 4-3) grown on Si (001), Si (111), and sapphire (0001) substrates are presented. For the ZrC films deposited on Si substrates, XRD spectra showed that growth planes of the films were the same as Si substrate surface planes, that is, ZrC (001) films were grown on Si (001) substrates, and ZrC (111) films were grown on Si (111) substrates. Besides, ZrC (111) films were grown on the sapphire (0001) basal plane. For all the films grown on Si (001) and sapphire substrates, no other peaks were found other than one peak in theta-2 theta symmetric XRD scan as shown in fig. 4-9, indicating that the films were highly out-of-plane textured. For the films grown on Si (111) substrate, the XRD peaks (top three spectra in fig. 4-10) showed two out-of-plane textures of (111) and (001). Due to high degree of texture, GIXD spectra at incidence angle of 1° (bottom three spectra in fig. 4-10) showed that the films deposited on Si (111) substrates exhibited barely visible humps, indicating a very small amount of grains possessing other crystalline orientations.

To check the texture degree, omega-rocking curves of the either ZrC (111) or ZrC (002) peaks were recorded for the ZrC films grown under the same conditions (ZC104

samples) but different substrates. As one can see in fig. 4-11, the films deposited on sapphire exhibited the highest texture with FWHM (full width at half maximum) of the omega-rocking curves of only  $0.68^\circ$ . The films deposited on Si (001) exhibited a FWHM of the ZrC (002) peak of  $3.37^\circ$ , while those deposited on Si (111) exhibited the rather large FWHM value of  $4.82^\circ$  for the ZrC peak (111). The Growth conditions of samples and measured FWHM of omega-rocking results are presented in table 4-3.

The growth conditions of samples were similar except small change of background gas pressures ( $2.2 \times 10^{-6} \sim 12 \times 10^{-6} \text{ C}_2\text{H}_2$ ). However, the FWHM values of omega-rocking curves were dramatically changed from  $2.53^\circ$  (ZC202, lowest) to  $5.45^\circ$  (ZC106, highest) for the films deposited on Si (001), whereas the FWHM values of the films deposited on sapphire (0001) do not seem to be sensitive to the change of background gas pressure (ZC104 and ZC107 in table 4-3). Measured omega-rocking curves for the films deposited on Si (001) and sapphire (0001) are displayed in fig. 4-12 and fig. 4-13, respectively. The reason of the rather high FWHM value for ZC204 sample in fig. 4-13 was due to accidentally discontinued growth.

To clarify the causes which affected crystal quality, lattice parameters for the films grown on Si (001) were calculated from ZrC (002) reflection of symmetric XRD in fig. 4-14, because crystal quality could be changed by strain energy in films during growth. As one can see in fig. 4-15, lattice parameter was linearly changed rather rapidly ( $\Delta a = \sim 1\%$ ) to a small change of background gas pressure ( $\Delta P = \sim 1.0 \times 10^{-5} \text{ C}_2\text{H}_2$ ). On the basis of the lattice parameter ( $a = 4.6930$ ) of reference powder diffraction (JCPDS PDF#: 35-0784 [Pcp94]), the closer measured lattice parameter, the better crystal quality in terms of rocking curve measurements, as it is shown in fig. 4-16.

In-plane texture was observed by phi-scan for  $\{111\}$  in-plane of ZrC (001) film (ZC202 in table 4-3) as displayed in fig. 4-17 (a). For cubic structures such as ZrC, four peaks should appear at the x-ray diffractometer configuration of phi-scan as displayed in fig. 4-17 (b), if in-plane texture exists. Details of the in-plane orientation were investigated by pole figure measurement of several crystalline orientations for both the films and the substrates. Typical results for ZrC films deposited on Si (001), Si (111), and sapphire with their substrates are displayed from fig. 4-18 to fig. 4-20. In these figures, the orientation relationships between films ((a) of each fig.) and substrates ((b) of each fig.) are also represented together, by starting the rotation of film and substrate from the same angular position. As one can see in these figures, the films were exhibiting a rather good in-plane texture, therefore, being epitaxial.

From (111) pole figures in fig. 4-18, which are obtained from both ZrC film deposited on Si (001) substrate and Si (001) substrate, very clear four in-plane  $\langle 111 \rangle$  pole reflections were only showed. The angular directions of the four  $\langle 111 \rangle$  poles are the same as  $\langle 111 \rangle$  pole directions of their substrates. This fact clearly indicates that  $(100)_{\text{ZrC}} // (100)_{\text{Si}}$  and  $[100]_{\text{ZrC}} // [100]_{\text{Si}}$  orientation relationship between film and substrate, which follows the concept of coincidence-site lattice (CSL), because when there is a good lattice match between film and substrate, high quality epitaxial growth is possible. Also the (100) pole figure of ZrC films grown on Si (111) substrate showed in-plane texture as indicated red circles in fig. 4-19 (a), but rather contained small fraction of randomly oriented inhomogeneous grains (displayed as blue contour), while the pole figure of ZrC films grown on Si (001) substrate showed cube on cube growth.

In case of ZrC films grown on sapphire (0001) substrate, (100) pole figure (fig. 4-20 (a)) from film and  $(1\ 1\ \bar{2}\ 6)$  pole figure (fig. 4-20 (b)) from sapphire substrate were examined to clarify the orientation relationship between the sapphire substrate and ZrC film. In the cubic system, three in-plane (100) reflections are formed by an angle of  $120^\circ$  with each other for a single crystal having (111) surface plane, thus the presence of six in-plane (100) reflections in fig. 4-20 (a) suggests the existence of two different in-plane crystal orientations, which are  $60^\circ$  rotated relatively to the other crystal orientation on same  $\langle 111 \rangle$  axis as indicated by red and blue circle in fig. 4-20 (a). This epigrowth was not expected for the interface having big mismatch ( $\sim 39\%$ ) between sapphire  $\langle 11\ \bar{2}\ 0 \rangle$  direction and ZrC  $\langle 110 \rangle$  direction. However, this fact could be well explained by ‘translational symmetries’ on both sides of the interface. We can define two lattices to match by translational symmetry, instead of comparing the bulk lattice parameters [Zur84]. As orientation relationship between ZrC and sapphire was presented in a schematic diagram (fig. 4-21), the superlattice mismatch is less than 0.6% between five atomic distances of film along the  $\langle 110 \rangle$  direction and four atomic distances of substrate along the  $\langle 01\ \bar{1}\ 0 \rangle$  direction. When superlattice mismatch is less than 1%, lateral movement of  $\pm 0.5\%$  of every atom on both sides of the interface can accommodate this superlattice mismatch [Zur84].

For two different crystallographic orientations of ZrC (111) grown on sapphire, it can be seen that there is only one possible nucleation site for atoms of the first monolayer at the interface, which is shown as A in fig. 4-22. However for the second layer, there are two different sites for atomic array, since the binding energy differences for adatoms occupying B sites or C sites are very small. As long as the island growth model is

considered where there are many nucleation sites on the surface of the substrate during the initial stage of growth, some nuclei grow in the ABCABC order; and other nuclei grow in ACBACB order. Thus two twin boundaries can be possibly formed. One is perpendicular to the surface when these crystallites with different orientations come together. The boundary is usually semicoherent or noncoherent depending on the habit plane [Bra66]. Also this fact is responsible for the rather large reflection area in pole figure in fig. 4-20 (a), indicating in-plane mosaicity. The other one is a parallel twin boundary, which is parallel to the surface of the film. During perpendicular growth, the stacking sequence of the (111) atomic planes could be lost by accident. In this case, the crystallites will grow in twin relation to the previous crystallite, and the boundary is coherent. Due to relatively small boundary energy in coherent twin boundary, its normal stacking sequence of (111) plane can be easily lost.

#### **4.3.3.2 TEM analysis of ZrC films grown on Si and sapphire substrate**

For further understanding of growth behavior and crystal structure of ZrC on Si and sapphire, cross-sectional specimens were prepared by FIB (focused ion beam) process. Before the FIB process, a carbon layer was coated on the surface of films to protect ion beam damage on film and to avoid electron charging. Just before FIB process, Pt was coated again to prevent from high energetic ion beam induced damage.

In fig. 4-23, a high resolution bright field image taken from the cross-section of the film grown on Si (111) substrate (ZC104 sample in table 4-3) is displayed. As it was expected from GIXD investigation, some random oriented grains were observed as inhomogeneous particles in continuously well stacked (111) ZrC film matrix rather than completely random oriented polycrystalline or columnar structure. These random grains were grown from very initial stage of growth, as they were located right at the interface,

indicating that chemical contribution to interfacial energy is much higher than that of ZrC grown on Si (001) substrate, assuming structure contribution to the interfacial energy is the same due to same lattice mismatch as ZrC grown on Si (001). An electron diffraction pattern of this sample was taken from the region shown in fig. 4-24 (a). Beam direction was defined by strong diffracted electron beam reflections from fig. 4-24 (b). Therefore, the cut plane was identified as  $(11\bar{2})$  plane, which is perpendicular to surface plane, meaning strong (111) texture. In addition, diffused electron diffraction pattern identified as (110) plane also can be seen in fig. 4-24 (b), indicating co-existing (001) texture with (111) texture other than random orientations.

From ZrC film grown on Si (001) substrate (ZC202 sample in table 4-3) in fig. 4-25 (a), a selected area diffraction pattern (SADP) was obtained in fig. 4-25 (b) to confirm the quality of the epitaxial film, and the orientation relationship between the film and Si substrate. As good epitaxial quality was expected from four clear and small (111) reflections in fig. 4-18 (a), SADP confirmed ZrC (001) was well aligned on Si (001) substrate as a single crystal with cube on cube relationship. In a pair of spots, the inner spots are coming from Si substrate, while the outer spots are from ZrC film. High resolution image in fig. 4-26 of this film showed clean lattice fringes without any Moiré lattice fringes.

Several cross-sectional TEM pictures taken from ZC104 film grown on sapphire (0001) were analyzed to verify the previously suggested twin structure used to explain the pole figure results. Suggested two types of twin structure were found in the regions marked as 'A' and 'B' from fig. 4-27. In a magnified image (fig. 4-28 (a)) of the region 'A', twin boundary parallel to the surface was observed as mirror image was observed by

drawn lines along atomic arrangements. A twin boundary perpendicular to the surface was also observed in region B in fig. 4-28 (b). The parallel twin boundary was very coherent by matching lattices of both sides, while the other showed an incoherent perpendicular twin boundary with atomic displacement at boundary.

#### 4.3.4 Surface analysis of ZrC films

The density and surface roughness of films were estimated by modeling acquired XRR spectra using the Wingixa™ software from Panalytical, described in section 4.3.2 and chapter 3. Regardless of the substrate type, similar density values of around  $6.7 \text{ g/cm}^3$  were obtained (ZC208 and ZC210 samples were excluded for estimation due to Ti contamination), and film surface was atomically flat with rms roughness value of  $0.4 \sim 0.7 \pm 0.2 \text{ nm}$ . The measured density values which are identical to tabulated values [Lid05] suggest that films are compact ZrC. The surface contamination layer density was around  $4 \sim 5 \pm 0.2 \text{ g/cm}^3$ , indicating the presence of an oxide or hydroxide compound or a mixture of both. The secondary electron (SE) images obtained by field emission SEM showed that surface morphology was very smooth at  $\times 10 \text{ K}$  for most deposits, and only at very high magnification ( $\times 50 \text{ K}$ ), surface roughness was discerned. SE images taken from ZrC film surfaces on Si and sapphire substrate are displayed, respectively in fig. 4-29 (ZC202 sample) and fig. 4-30 (ZC204 sample). Density and roughness values of as-grown films are listed in table 4-5. The rms values obtained from AFM height images from fig. 4-31 to fig. 4-36 confirmed that roughness of surface was less than 1 nm for all samples. But surface morphology was little different depending on growth direction of growing films. That is, ZrC (001) surface showed many small cluster looking features as shown in fig. 4-31 ~ fig. 4-33, whereas ZrC (111) surface was atomically very flat

enough not to be discerned by AFM image as displayed in fig. 4.34 ~ fig. 4.36 under all experimental growth conditions.

Table 4-5. Surface roughness and density of as-grown films.

Substrate	ID	$P_d$ (Torr)	$T_s$ (°C)	Thickness (Å)	Density (g/cm <sup>3</sup> )		Roughness (Å)
					Film	Topmost	
Si (001)	ZC106	$1.0 \times 10^{-5}$ C <sub>2</sub> H <sub>2</sub>	750	714	6.7	4.1	6
	ZC107	$6.7 \times 10^{-6}$ C <sub>2</sub> H <sub>2</sub>	750	376	6.7	4.3	7
	ZC202	$6.2 \times 10^{-6}$ C <sub>2</sub> H <sub>2</sub>	775	1034	6.8	5.8	5
	ZC208	$2.2 \times 10^{-6}$ CH <sub>4</sub>	750	368	6.9	4.3	4
	ZC210	$9.0 \times 10^{-7}$ CH <sub>4</sub>	750	714	6.8	5.6	5
Si (111)	ZC107	$6.7 \times 10^{-6}$ C <sub>2</sub> H <sub>2</sub>	750	333	6.7	4.3	6
	ZC208	$2.2 \times 10^{-6}$ CH <sub>4</sub>	750	381	6.9	4.9	7
Sapphire (0001)	ZC208	$2.2 \times 10^{-6}$ CH <sub>4</sub>	750	383	6.8	5.6	5
	ZC210	$9.0 \times 10^{-7}$ CH <sub>4</sub>	750	656	6.8	5.2	5

As mentioned before in chapter 2, one of problems in ZrC film growth is oxygen contamination due to high zirconium atoms affinity for oxygen. As an example, when laser was stopped during ZrC deposition (discontinuous growth), a bright layer (atomic contrast) was formed due to high oxygen contamination as displayed in a cross-sectional bright field TEM image (fig. 4-37).

For quantitative x-ray microanalysis of a ZrC film which was grown on Si (001), a scanning transmission electron microscope (STEM) equipped with an x-ray energy dispersive spectrometer (XEDS) was used. Sample ZC106 was chosen because it showed most distinguishable three different layer structures among samples as shown in fig. 4-38. The result is shown by TEM-EDX analysis in fig. 4-39. From line spectra, carbon and oxygen elements were almost constant through thickness and detected a little more near surface. Oxygen content was 9.6 atomic % near Si/ZrC interface (spot 3), a little lower

value of 5.2 % in bulk (spot 4), and again higher value of 13.8 % at surface layer (spot 5). For carbon content, a higher value (~70%) was detected. But this could not be true because the characteristic x-ray absorption by carbon counted too low, and due to carbon supported TEM grid behind sample and protecting carbon coating near surface. However, the ratio of Zr to carbon was quite constant near interface (spot 3) and in bulk (spot 4), implying stoichiometric composition.

For detail surface composition analysis, XPS investigations were performed. These investigations revealed the presence of several C 1s lines on the surface of the deposited ZrC films. Since the binding energies of the XPS peaks are usually referenced to the binding energy of adventitious carbon, this fact could introduce errors in this case. Thus pure ZrO<sub>2</sub> films deposited on Si by PLD [How02] were analyzed to accurately determine the position and shape of Zr 3d and O 1s peaks to avoid this problem.

In fig. 4-40, high resolution XPS scans of the Zr 3d region acquired at 45° and 90° take-off angles from a sample deposited at 600 °C under vacuum ( $5 \times 10^{-6}$  Torr) are shown. The used laser parameters were 8 J/cm<sup>2</sup> fluence, and 5 Hz repetition rate. It is apparent that the surface contains a rather high percentage of Zr-O bonds [Coc98] (peaks denoted by B located at 184.5 eV and D at 186.9 eV, respectively). From a sample that was deposited at 600 °C under  $1 \times 10^{-4}$  Torr of C<sub>2</sub>H<sub>2</sub>, XPS spectra are shown in fig. 4-41 after 5 min sputtering with 4 keV Ar<sup>+</sup> ions, which removed the first 4 nm of the outermost layer. For this sample, there is a minimal angle dependence of the ratio of Zr-O to Zr-C peaks, indicating a homogeneous bulk composition. The percentages of the Zr atoms bonded to carbon are shown in table 4-6, which is estimated from the XPS measurements for a series of samples. Based on XRD data in fig. 4-4, the use of a low C<sub>2</sub>H<sub>2</sub> atmosphere

appeared to have a beneficial effect on crystallinity too. However, the oxygen concentration was rather high in the surface region of these films.

Table 4-6. The relative percentage of Zr 3d XPS areas corresponding to Zr-C bonds at different take-off angles.

Deposition Pressure	As-received		Sputtered	
	45°	90°	45°	90°
$5 \times 10^{-6}$ Torr	20.6 %	31.5 %	44.9 %	45.2 %
$1 \times 10^{-4}$ Torr of $C_2H_2$	14.6 %	24.8 %	47.2 %	49.1 %
$7 \times 10^{-4}$ Torr of $C_2H_2$	1.0 %	3.8 %	22.4 %	29.0 %

Table 4-7. Resistivity of as-deposited ZrC films

		I( $\mu$ A)	V(mV)	$\rho_1$ (from t1)	$\rho_2$ (from t2)	t1(nm) (TEM)	t2(nm) (XRR)
ZC104i1 (111)Si	1	30	0.302	1.87E-04	1.83E-04	41	40
	2	30	0.292	1.81E-04	1.76E-04	41	40
	3	30	0.282	1.75E-04	1.70E-04	41	40
Z202 (100)Si	1	30	0.115	1.63E-04	1.79E-04	94	103
	2	30	0.113	1.60E-04	1.76E-04	94	103
	3	30	0.106	1.51E-04	1.65E-04	94	103
	4	30	0.105	1.49E-04	1.63E-04	94	103
Z204a (Sapphire)	1	30	0.115	1.55E-04	1.51E-04	89	87
	2	30	0.116	1.56E-04	1.52E-04	89	87
	3	30	0.12	1.61E-04	1.58E-04	89	87
	4	100	0.3855	1.56E-04	1.52E-04	89	87
	5	100	0.383	1.54E-04	1.51E-04	89	87

AES investigations were performed to analyze the bulk composition of the film. The results confirmed that the first 2.0 ~ 3.0 nm (surface region) of the ZrC films were heavily contaminated with oxygen as one can see in fig. 4-42, which was a typical depth profile acquired from an as-deposited film. However, once the topmost layer was

removed by Ar ion sputtering, the oxygen content dramatically decreased to values below 7 ~ 8 % as shown in fig. 4-43 (ZC202). Despite relatively the high levels of oxygen contamination, the deposited ZrC films were very conductive, and similar values were obtained in table 4-7. Under best vacuum conditions ( $P_0 = 1.3 \sim 1.5 \times 10^{-7}$  Torr) and using a low pressure of high purity  $\text{CH}_4$  during deposition, oxygen concentration was less than 2.5 % within the bulk, as shown in fig. 4-44 (ZC107).

According to residual gas analysis by RGA (residual gas analyzer), just right before deposition and after introducing  $\text{C}_2\text{H}_2$  and  $\text{CH}_4$  gas,  $\text{C}_2\text{H}_2$  gas contained rather high oxygen concentration when compared with pre-vacuum condition as displayed in fig. 4-45. So it is thought that oxygen contamination of the films deposited under  $\text{C}_2\text{H}_2$  atmosphere is caused by the limited purity of the used gas.

#### 4.4 Summary

In summary, ZrC thin films were deposited on Si and sapphire substrates by the pulsed laser deposition technique. A combination of high laser fluence and high substrate temperature (600 ~ 700 °C) was required to obtain crystalline films on Si (001) substrates.

Under very low water vapor pressures ( $\sim 10^{-8}$  Torr), high substrate temperatures ( $\sim 750$  °C), and high laser fluence ( $10 \text{ J/cm}^2$ ), epitaxial ZrC films were deposited on single crystalline substrates. The ZrC films grew along the [001] axis on Si (001), while they grew along the [111] axis on Si (111) and sapphire (0001). Pole figure measurements showed that ZrC films exhibited in-plane orientation too, depending on the type of substrates. Grazing incidence x-ray diffraction investigations evidenced the presence of a rather small fraction of randomly oriented crystallites. The films mass density was around the tabulated value of  $6.7 \text{ g/cm}^3$ , while the surface morphology was very smooth, with a roughness value (rms) of  $0.4 \sim 0.7 \pm 0.2 \text{ nm}$ .

$C_2H_2$  as background gas increased a chance to bond Zr with C, and improved crystallinity and stoichiometry. Lattice parameter of deposited ZrC film was changed by small variations of  $C_2H_2$  pressure. There exists an optimum pressure value for good crystal quality.

Contamination of mainly Zr-O was found in the surface layers deposited under  $C_2H_2$  or residual atmosphere, whereas the oxygen content dramatically decreased to values below 7 ~ 8 % after topmost layers were removed by Ar ion sputtering. Despite the high levels of oxygen contamination, the deposited ZrC films were very conductive. Under best vacuum conditions ( $P_0 = 1.3 \sim 1.5 \times 10^{-7}$  Torr) and using a low pressure of high purity  $CH_4$  during deposition, oxygen concentration was dramatically reduced to less than 2.5 %.

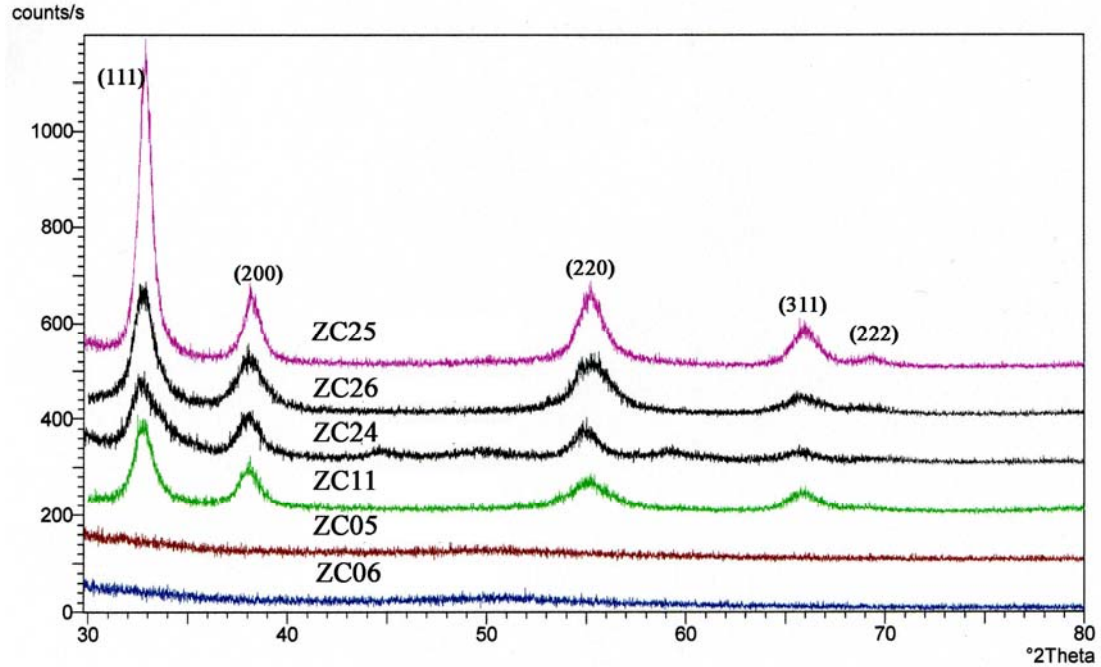


Figure 4-1. GIXD spectra (incidence beam angle,  $\omega = 1^\circ$ ) of ZrC films deposited under various conditions.

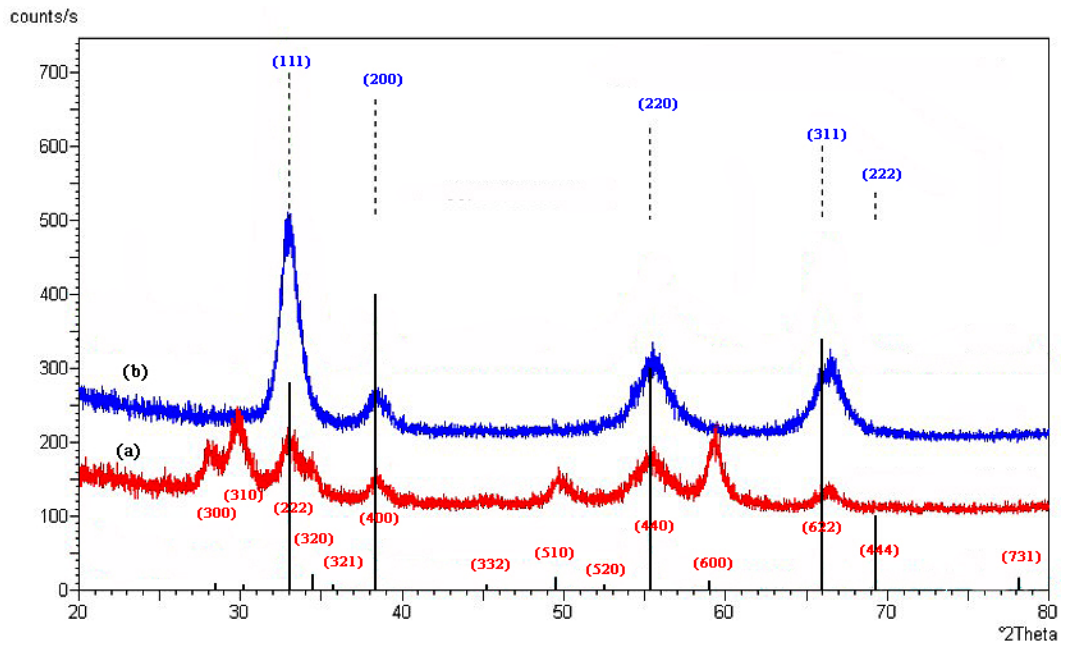


Figure 4-2. Comparison of GIXD spectra obtained from ZrC deposited films at same deposition conditions (a) without pre-ablated target (red) and (b) with pre-ablated target (blue).

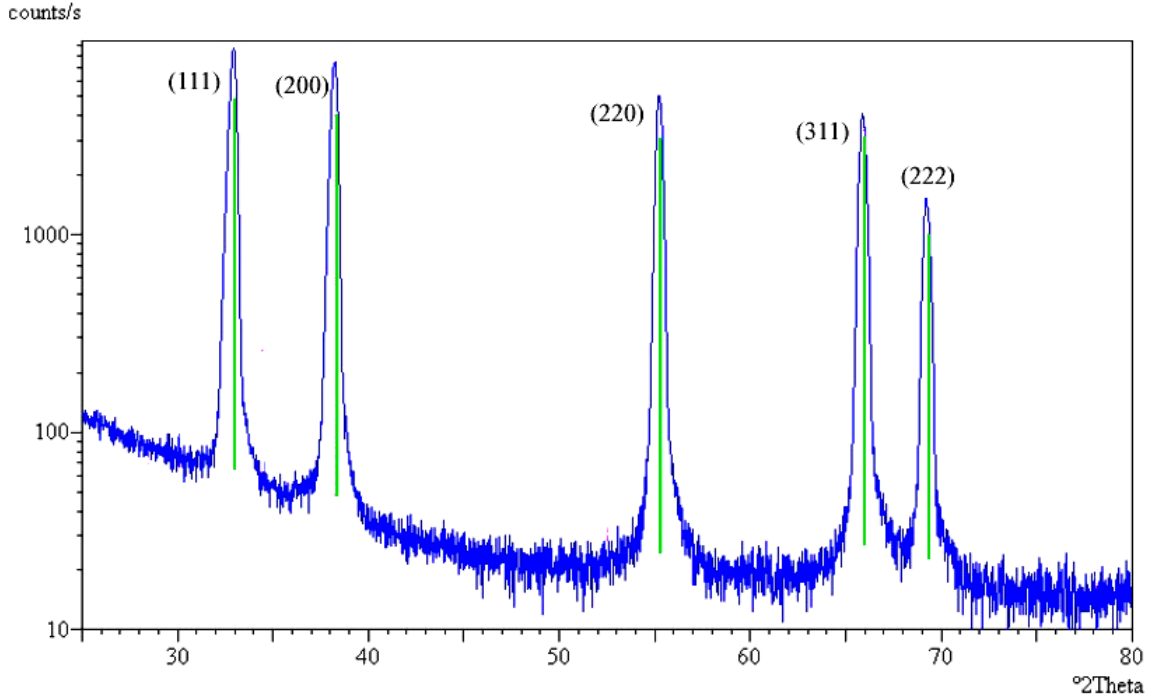


Figure 4-3. XRD spectra obtained from ZrC target; vertical lines represent position and intensity for stoichiometric ZrC, JCPDS PDF# 32-1489.

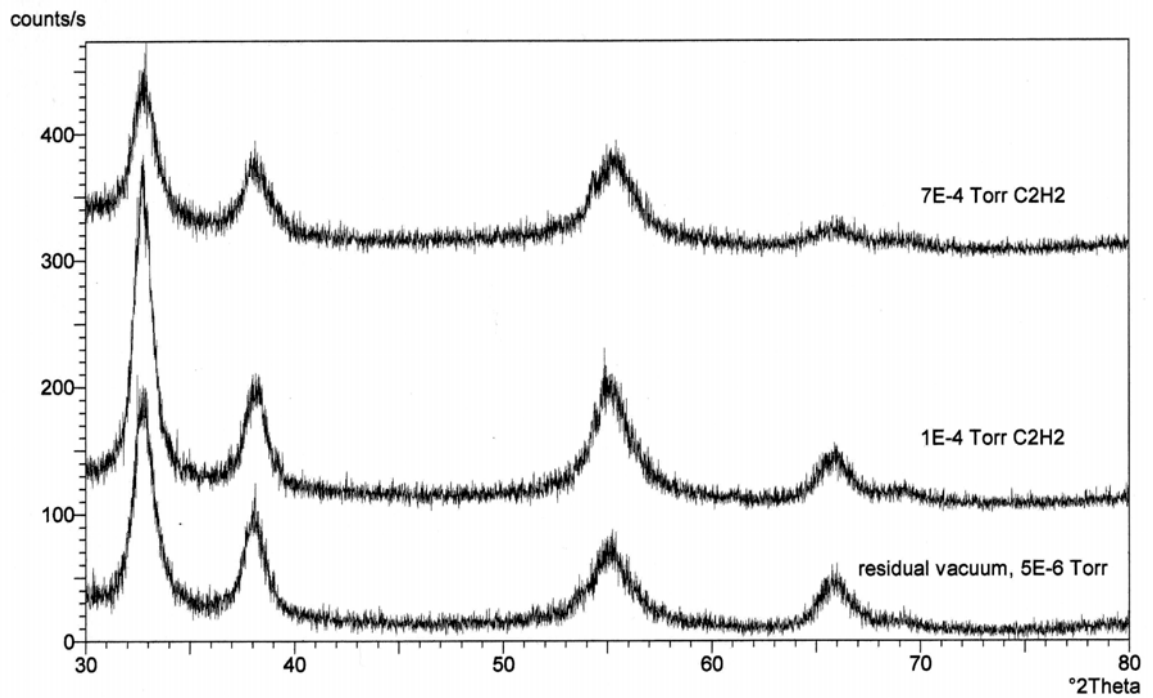


Figure 4-4. GIXD spectra obtained from films deposited under residual vacuum and different  $C_2H_2$  gas pressures.

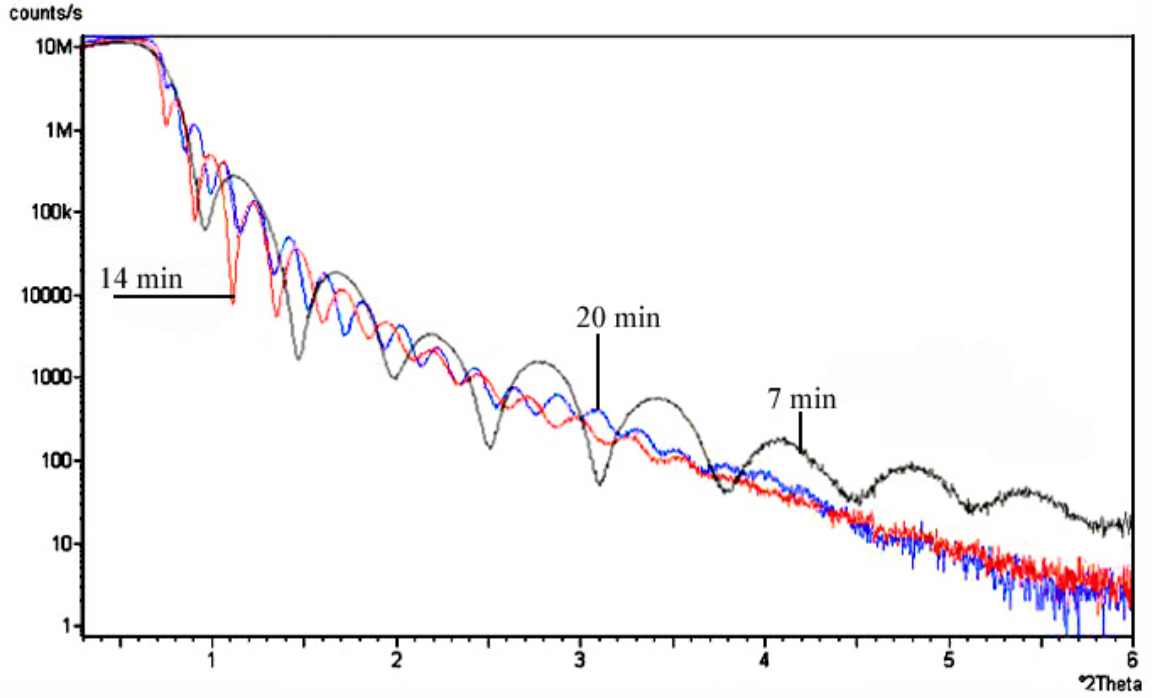


Figure 4-5. XRR spectra of ZrC films deposited for various times at 700 °C and 10 J/cm<sup>2</sup> under vacuum.

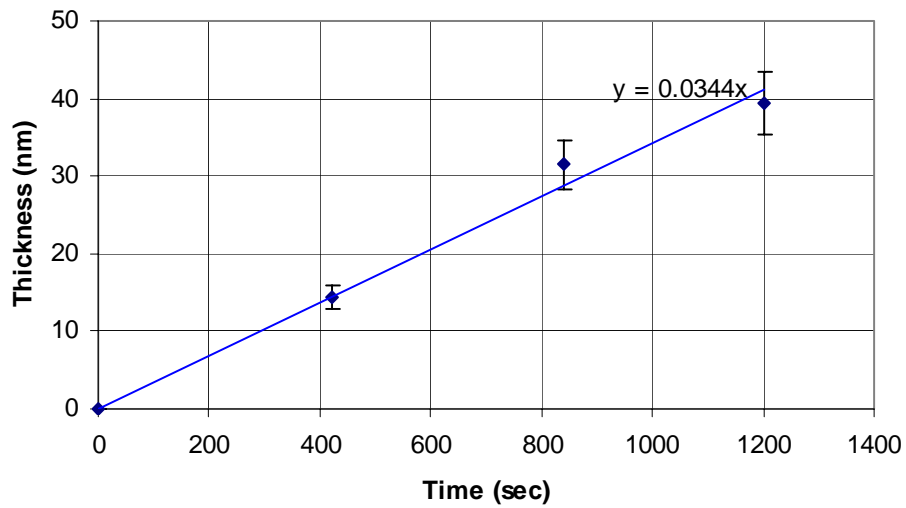


Figure 4-6. ZrC film deposition rate at  $T_s = 700^\circ\text{C}$ ,  $P_d = 1.0 \times 10^{-6}$  Torr, 10 J/cm<sup>2</sup>, and 5Hz.

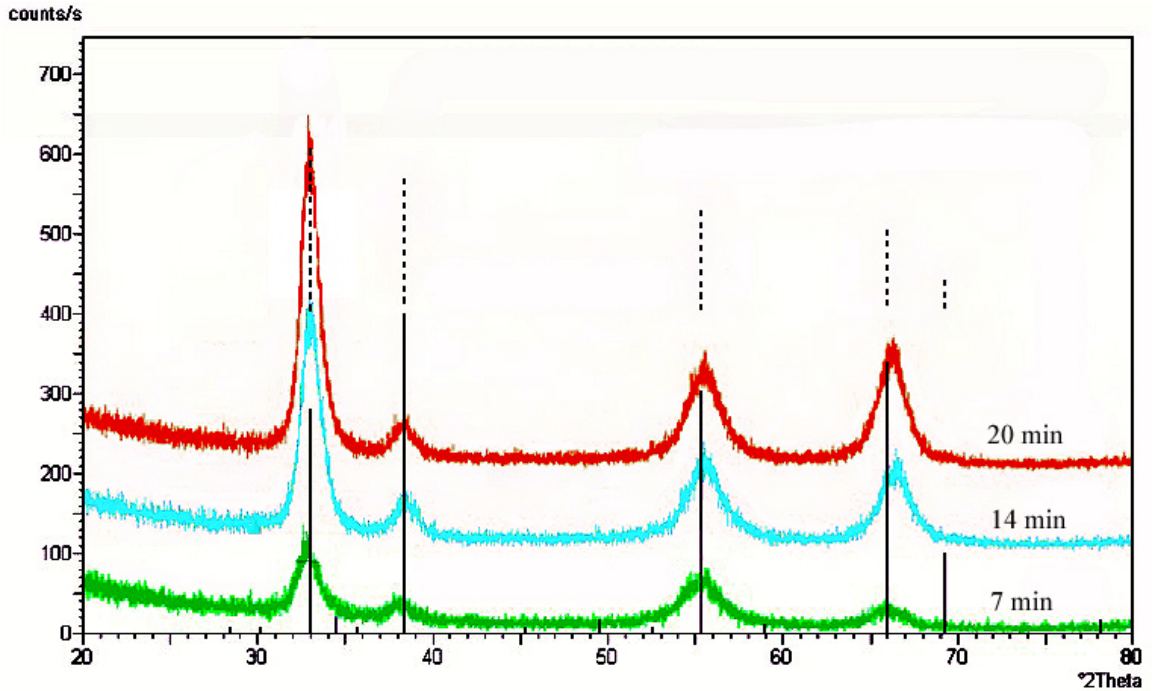


Figure 4-7. GIXD spectra of ZrC films deposited for various times at 700 °C and 10 J/cm<sup>2</sup> under vacuum; the standard position of diffraction lines from ZrC (dashed lines) and ZrC<sub>0.7</sub> (solid lines) are also shown.

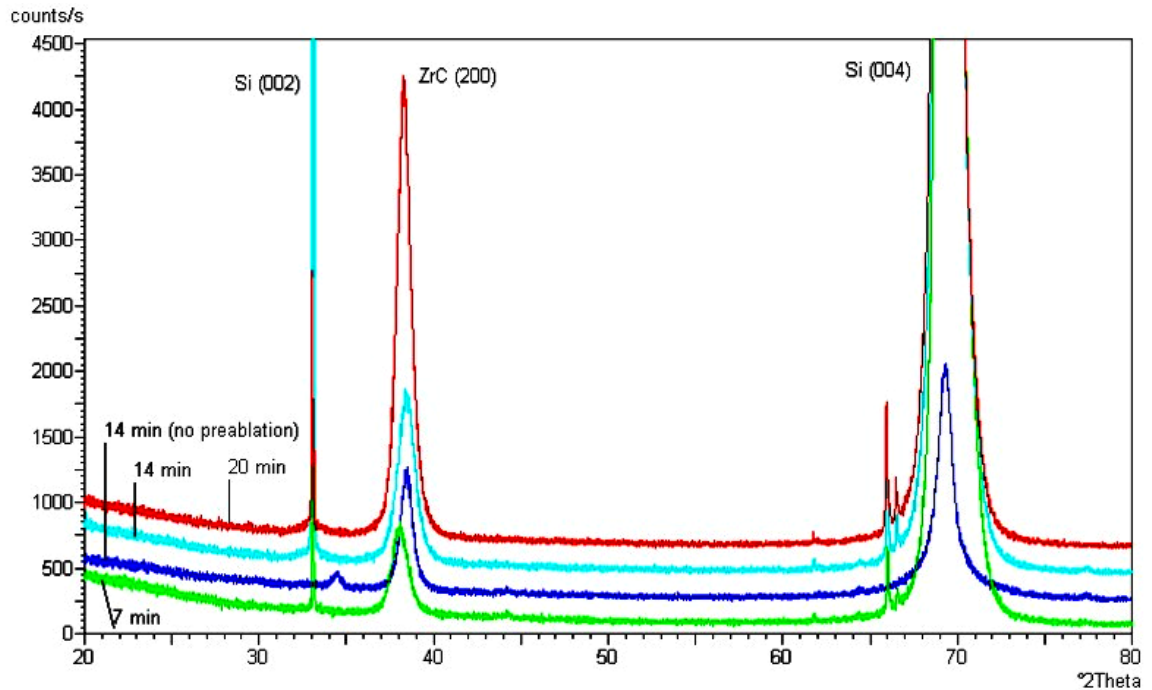


Figure 4-8. XRD spectra of ZrC films deposited for various times at 700 °C and 10 J/cm<sup>2</sup> under vacuum.

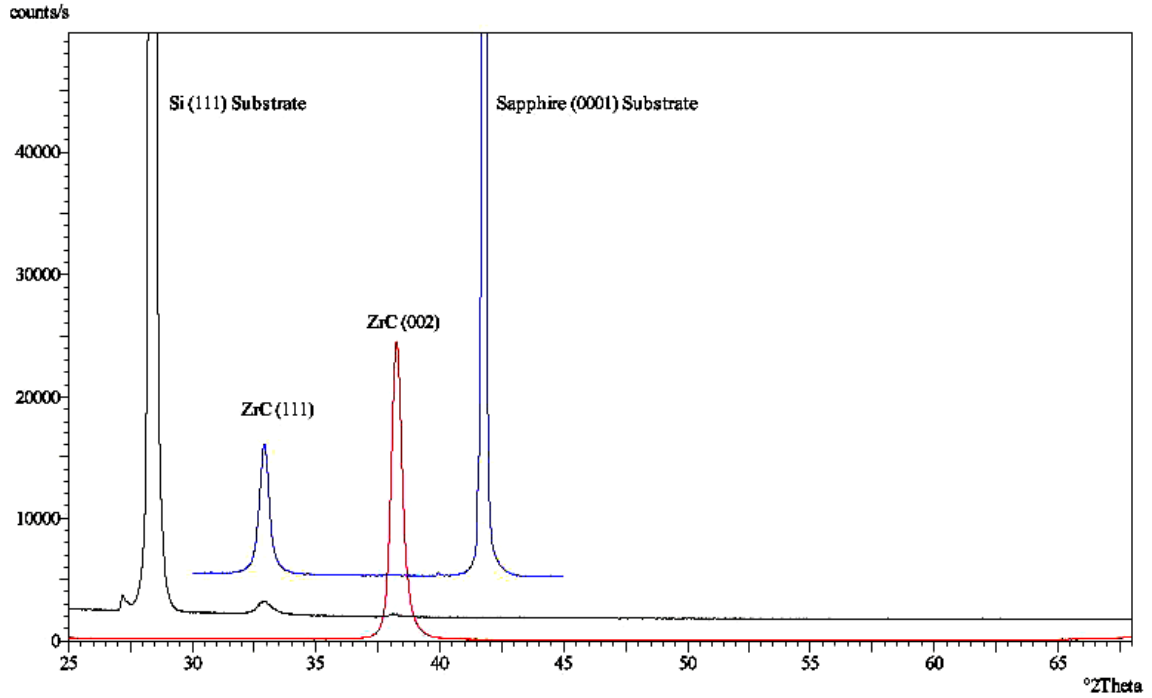


Figure 4-9. XRD spectra of ZrC films deposited at 750 °C on various substrates

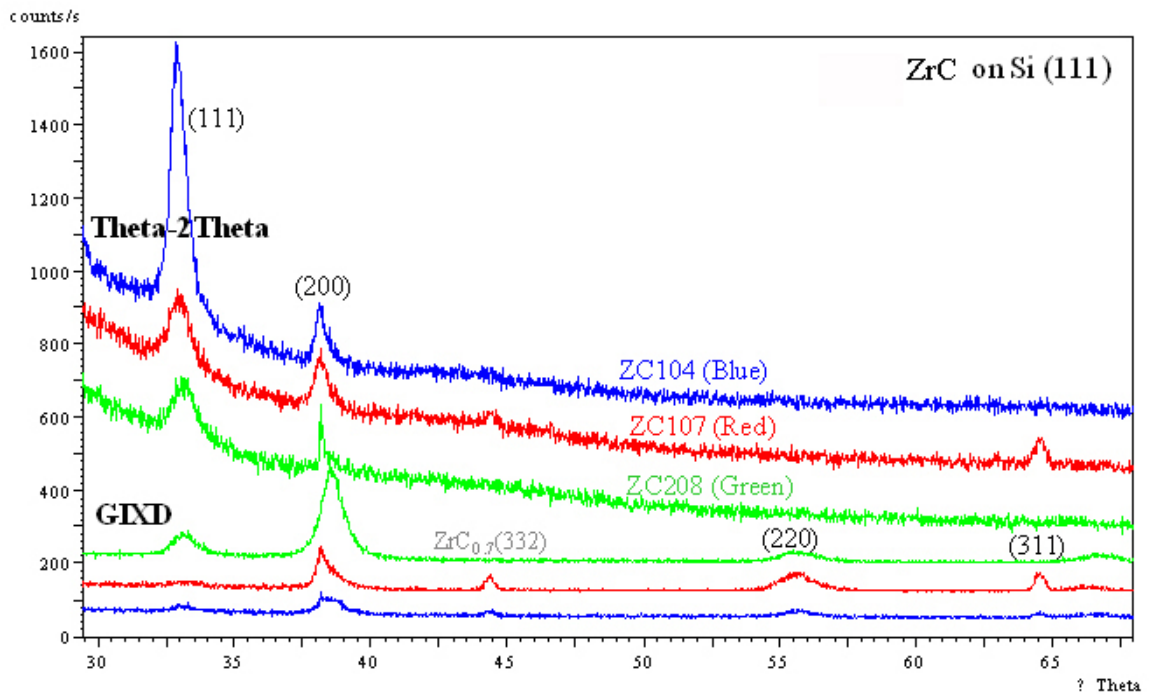


Figure 4-10. XRD and GIXD spectra (incidence beam angle = 1°) of ZrC films deposited on Si (111) substrates.

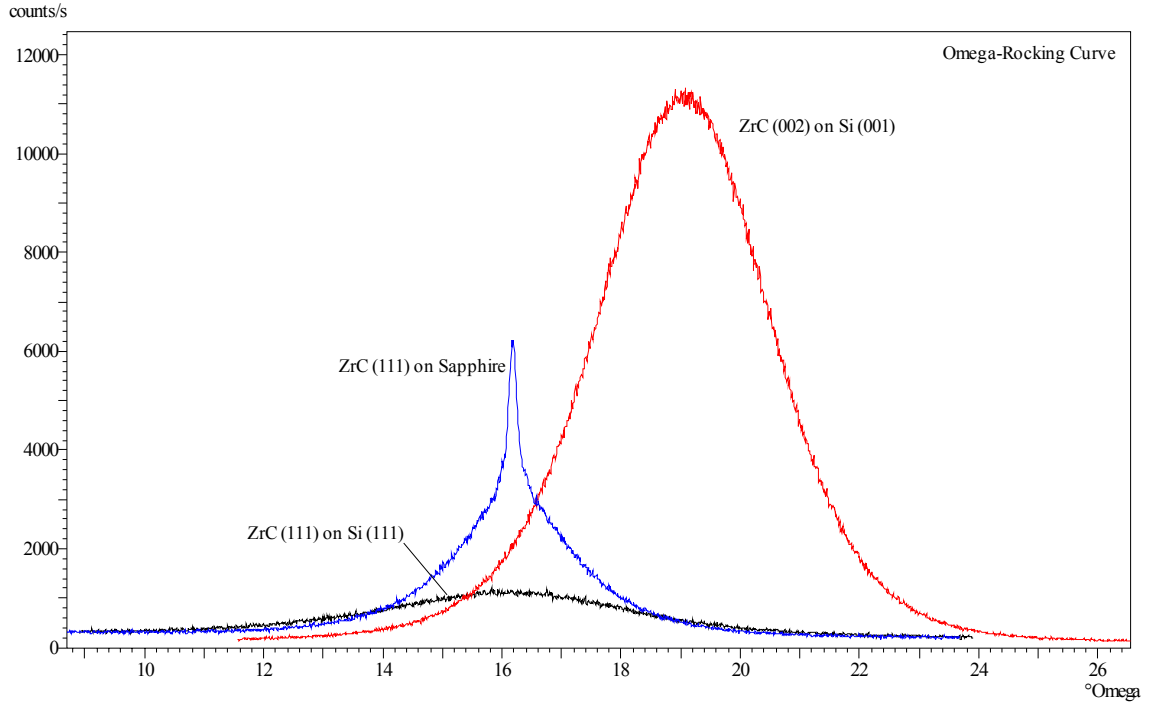


Figure 4-11. Omega-rocking curves of ZrC (111) or (200) peaks recorded from ZC104 films deposited at 750 °C on various substrates.

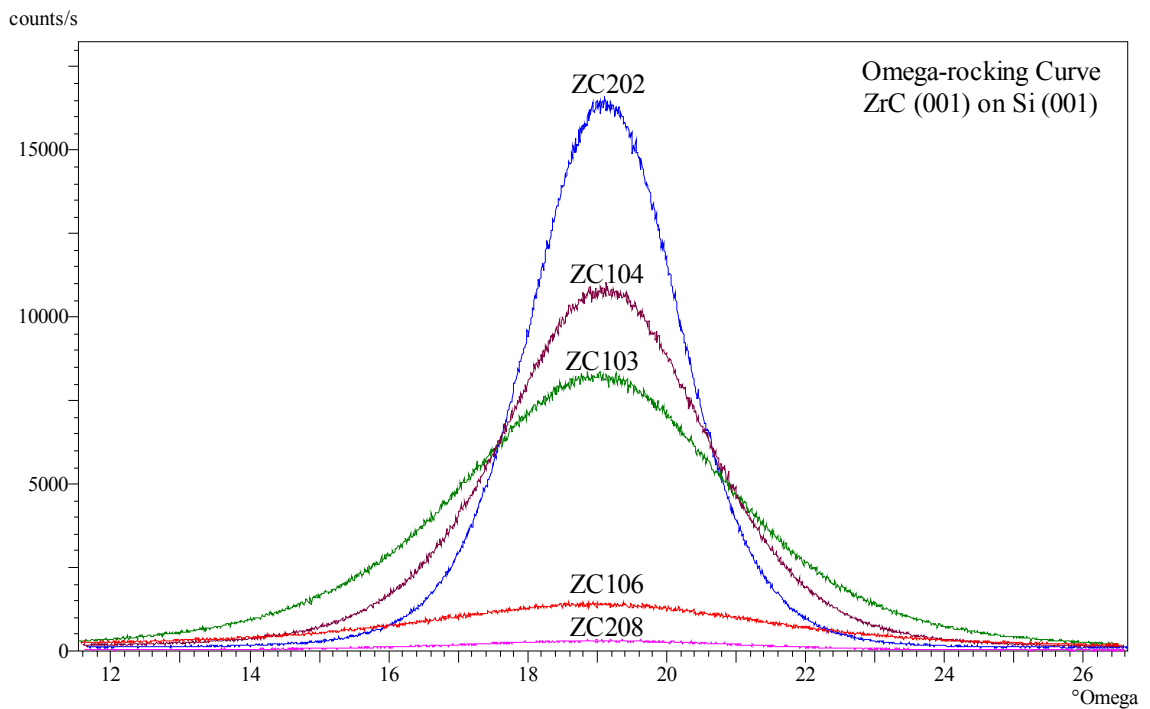


Figure 4-12. Omega-rocking curves of ZrC (002) peaks recorded from the films deposited on Si (001) substrate at various background gas pressures.

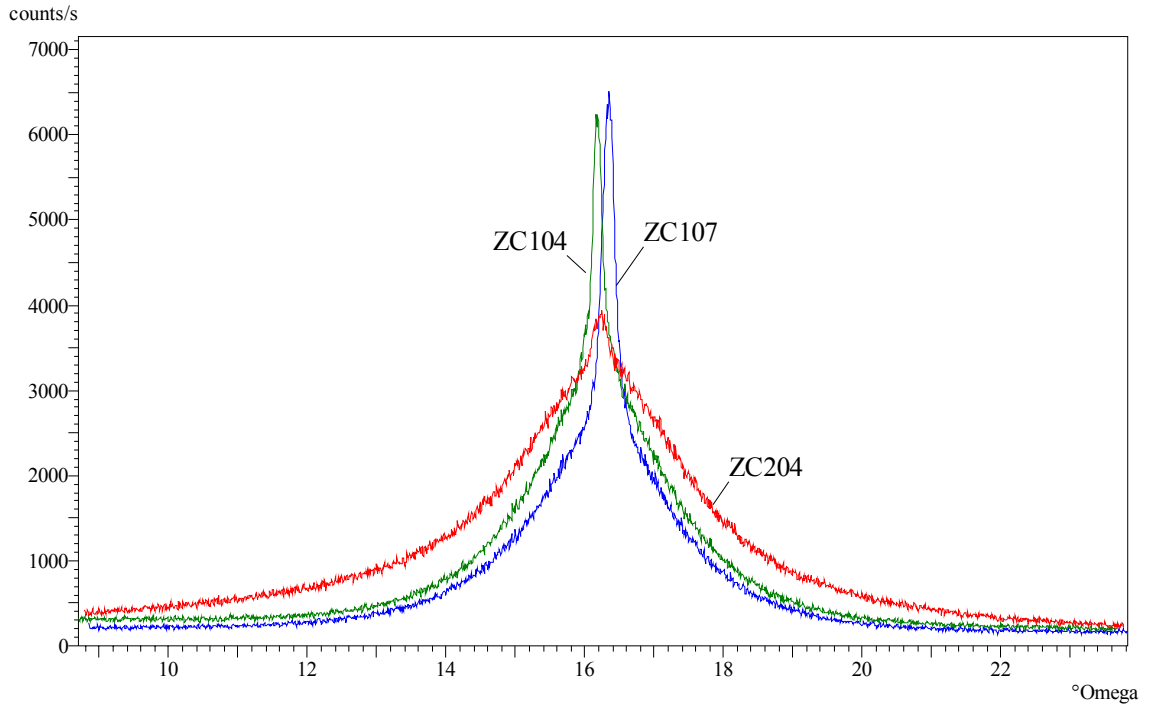


Figure 4-13. Omega-rocking curves of ZrC (111) peaks recorded from the films deposited on sapphire (0001) substrate at various different gas pressures

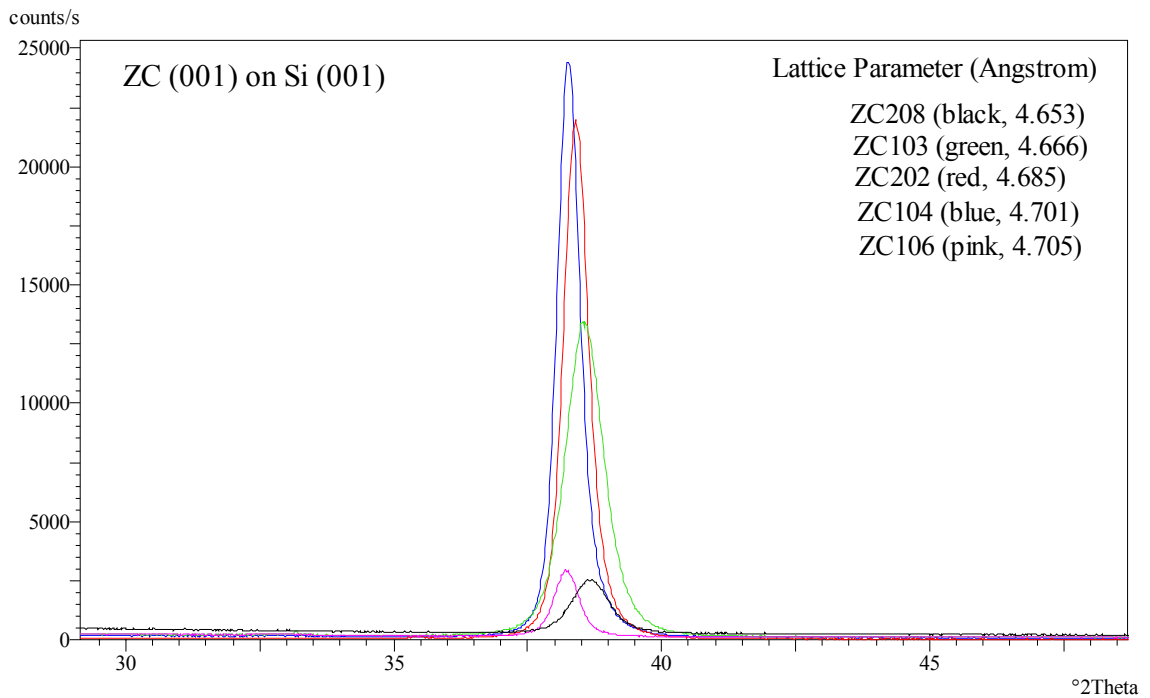


Figure 4-14. XRD spectra of (002) reflection from the films deposited on Si (001) and calculated lattice parameters.

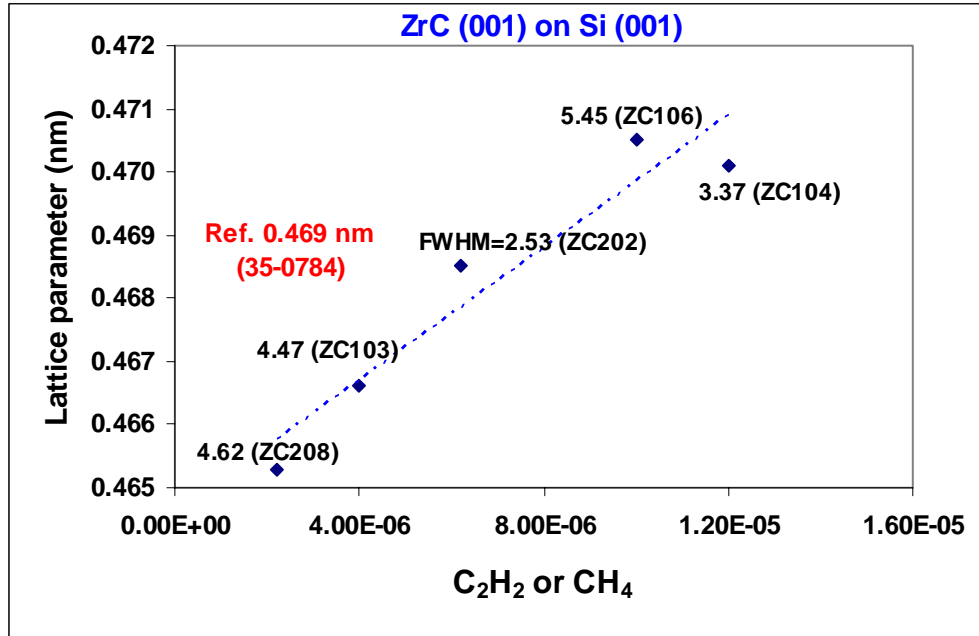


Figure 4-15. Background gas effect on lattice parameter of the films deposited on Si (001) substrate.

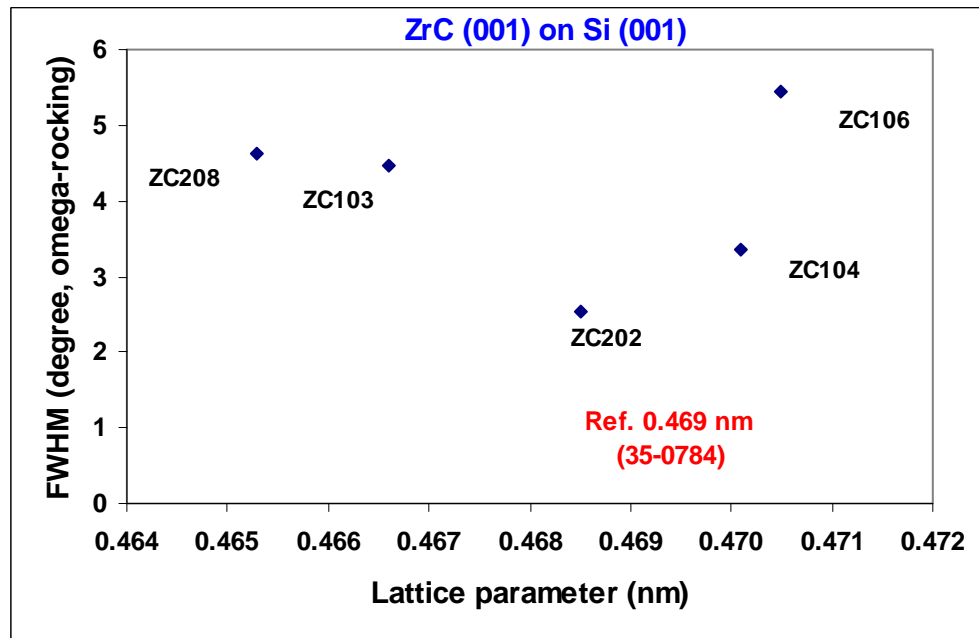


Figure 4-16. The relationship between deposited films on Si (001) and texture degree of the films measured by omega-rocking curve.

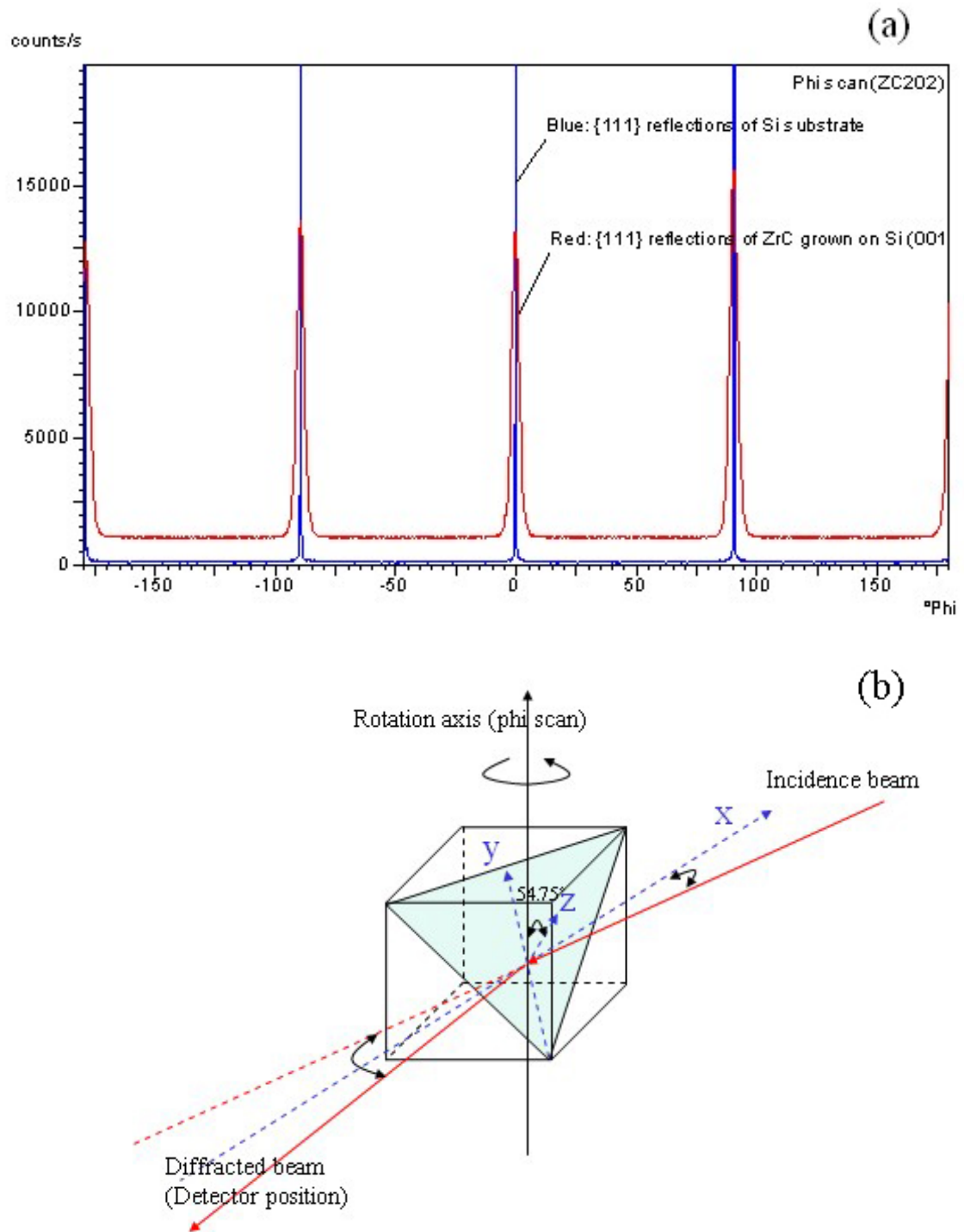


Figure 4-17. Phi-scan of {111} in-plane obtained from (a) ZrC film and Si (001) substrate of sample ZC202 and (b) phi-scan diffractometer configuration.

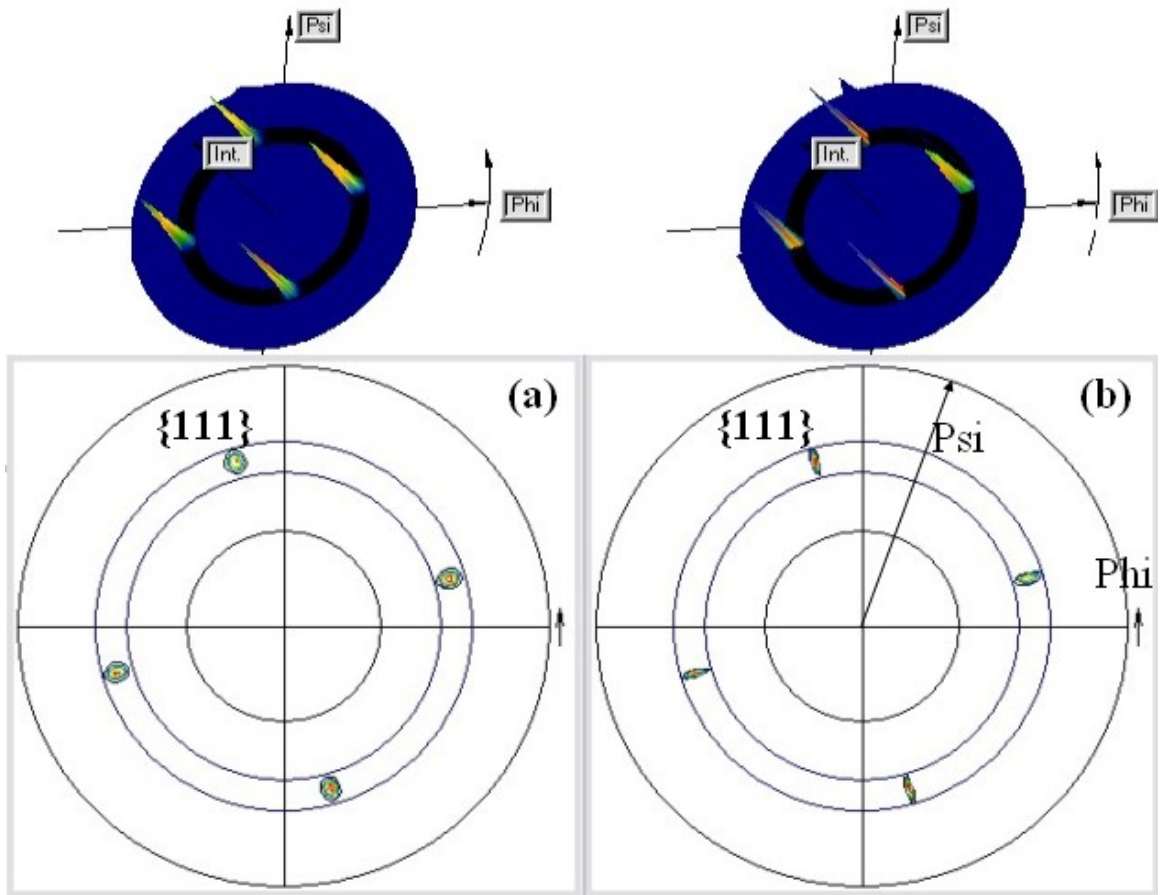


Figure 4-18. (111) pole figures of (a) ZrC film and (b) Si (001) substrate obtained from sample ZC202.

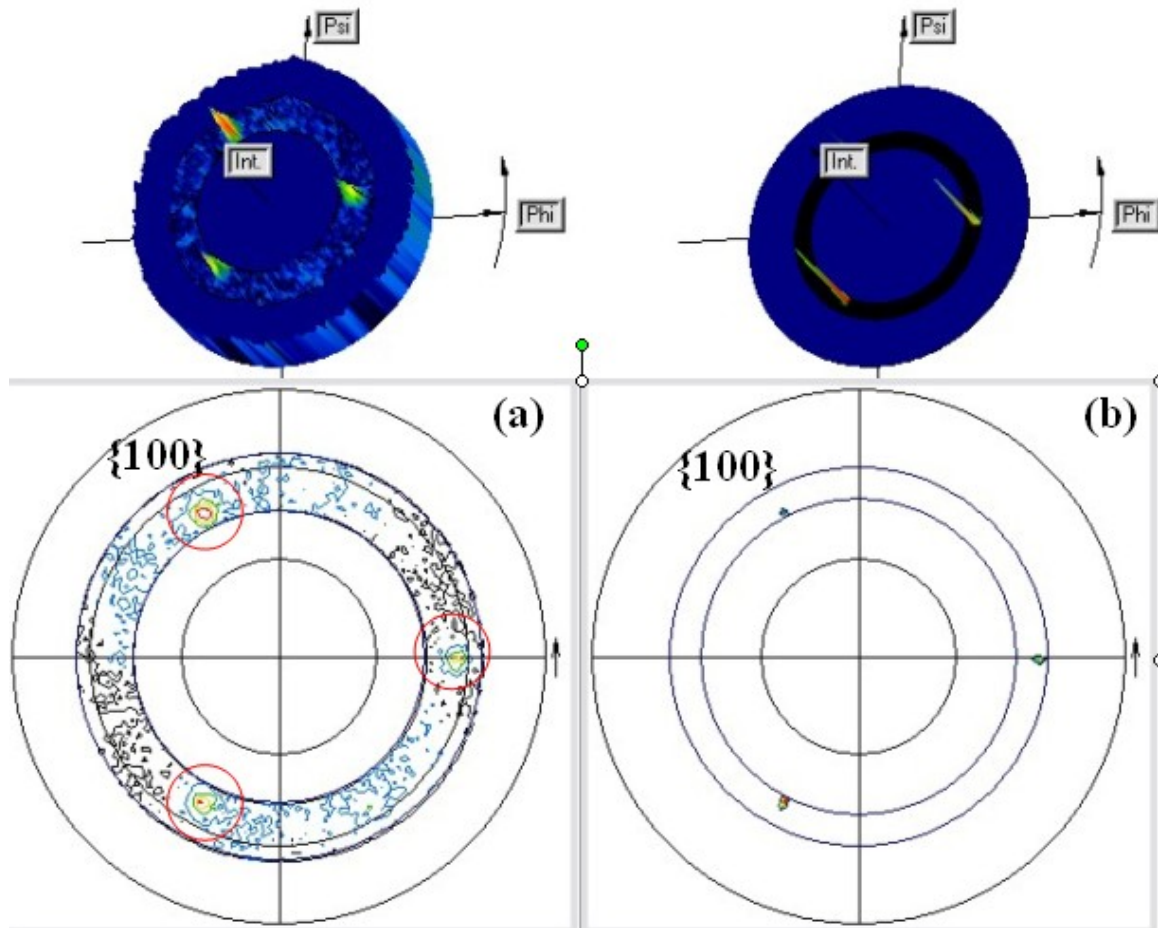


Figure 4-19. (100) pole figures of (a) ZrC film and (b) Si (111) substrate obtained from sample ZC104.

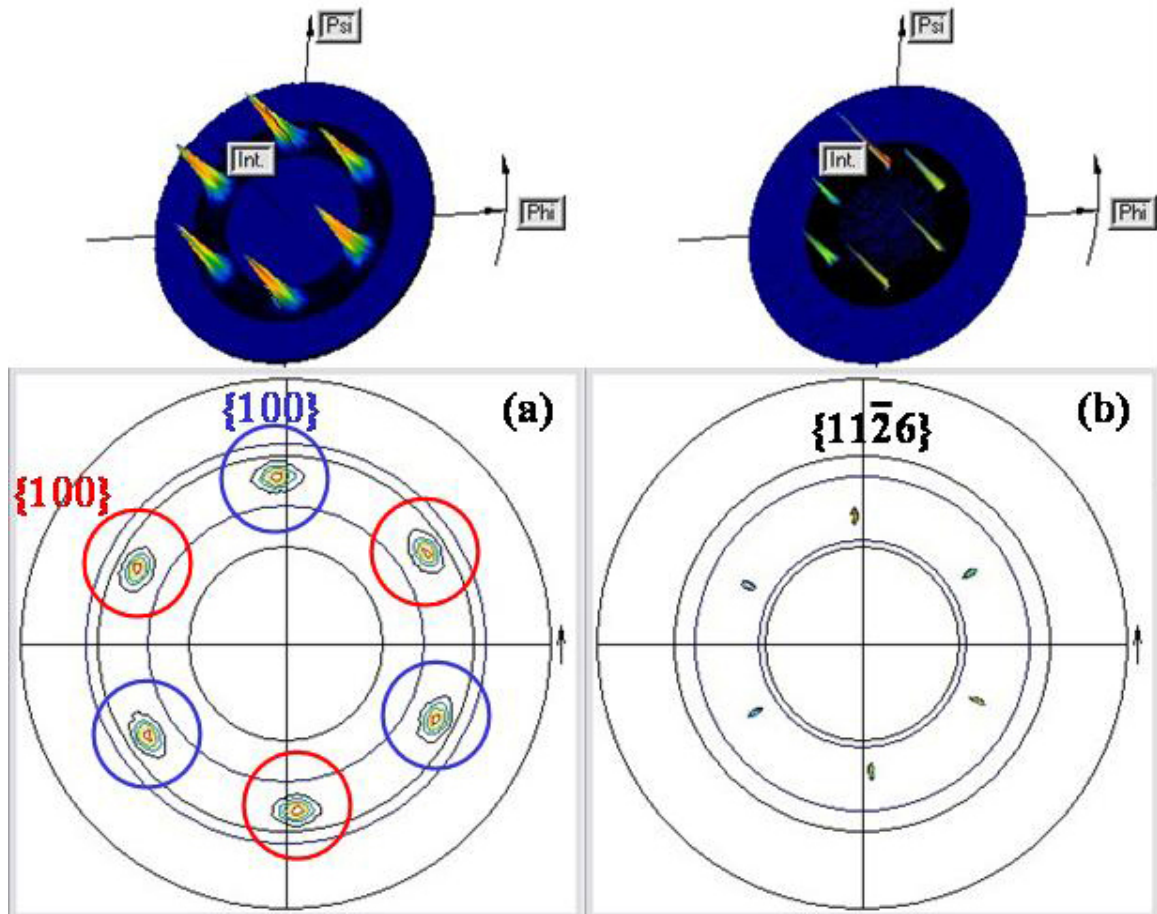


Figure 4-20. Pole figures showing (a)  $\{100\}$  pole figures of ZrC film, and (b)  $\{11\bar{2}6\}$  pole figure of sapphire (0001) substrate obtained from ZC104.

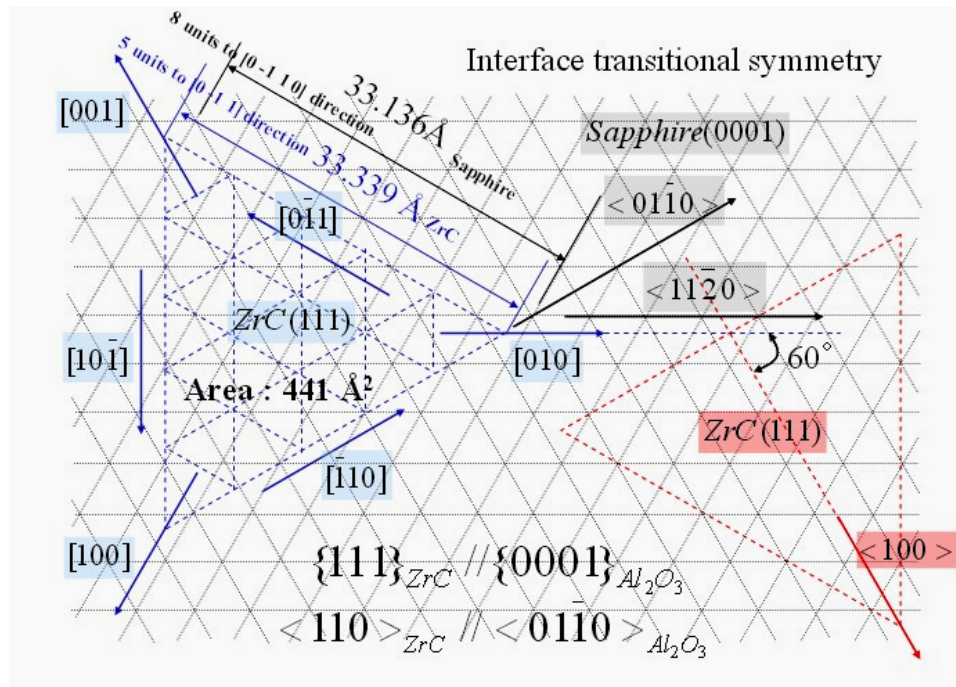


Figure 4-21. Projection view for two crystallographic orientations of ZrC grown on sapphire (0001), and orientation relationship between ZrC film and sapphire substrate.

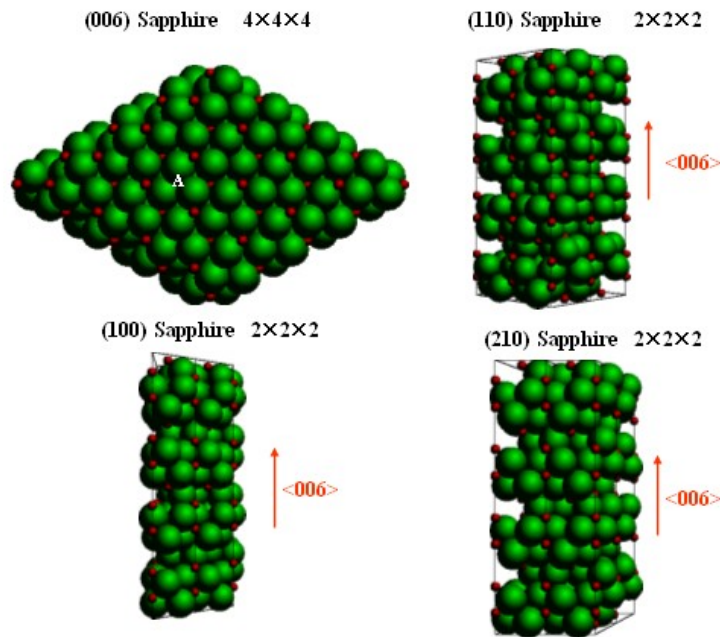


Figure 4-22. Possible nucleation site (marked as A) for the first monolayer on sapphire (0001).

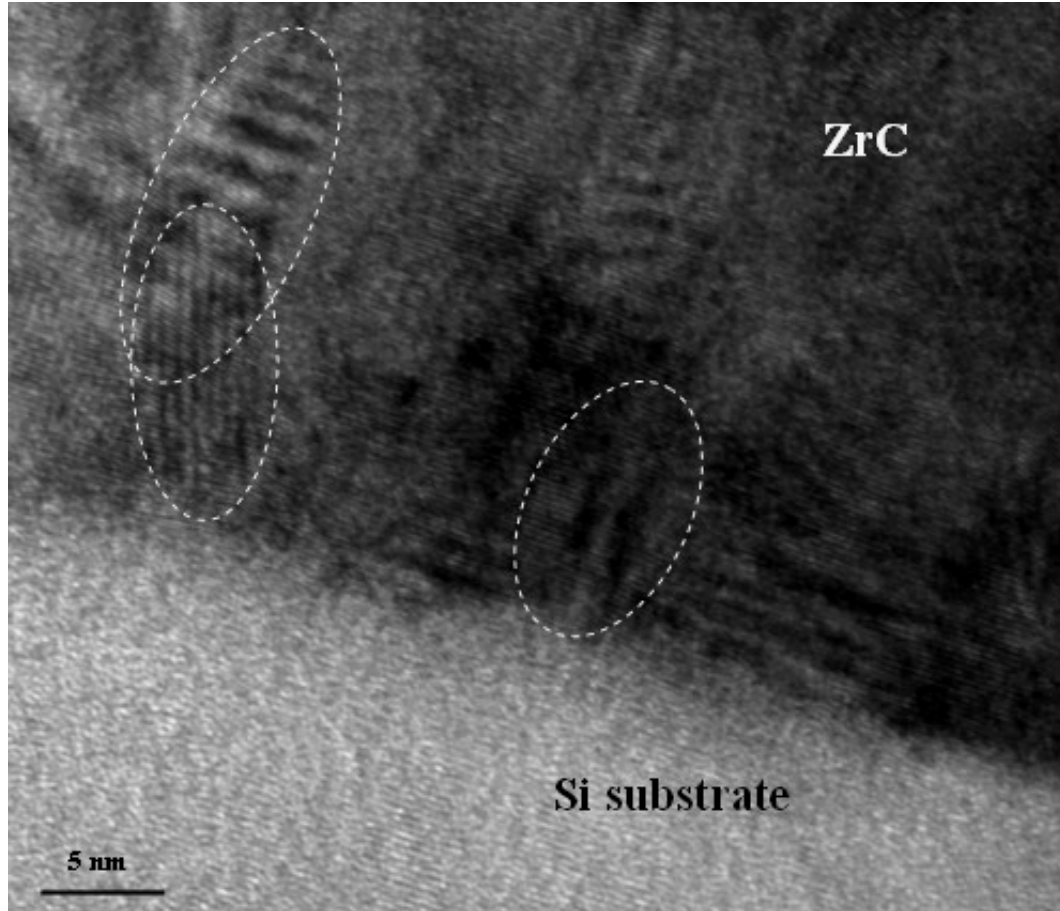


Figure 4-23. Bright field TEM image obtained from cross-section of ZrC film grown on silicon (111) substrate; the regions showing inhomogeneous random grains are marked.



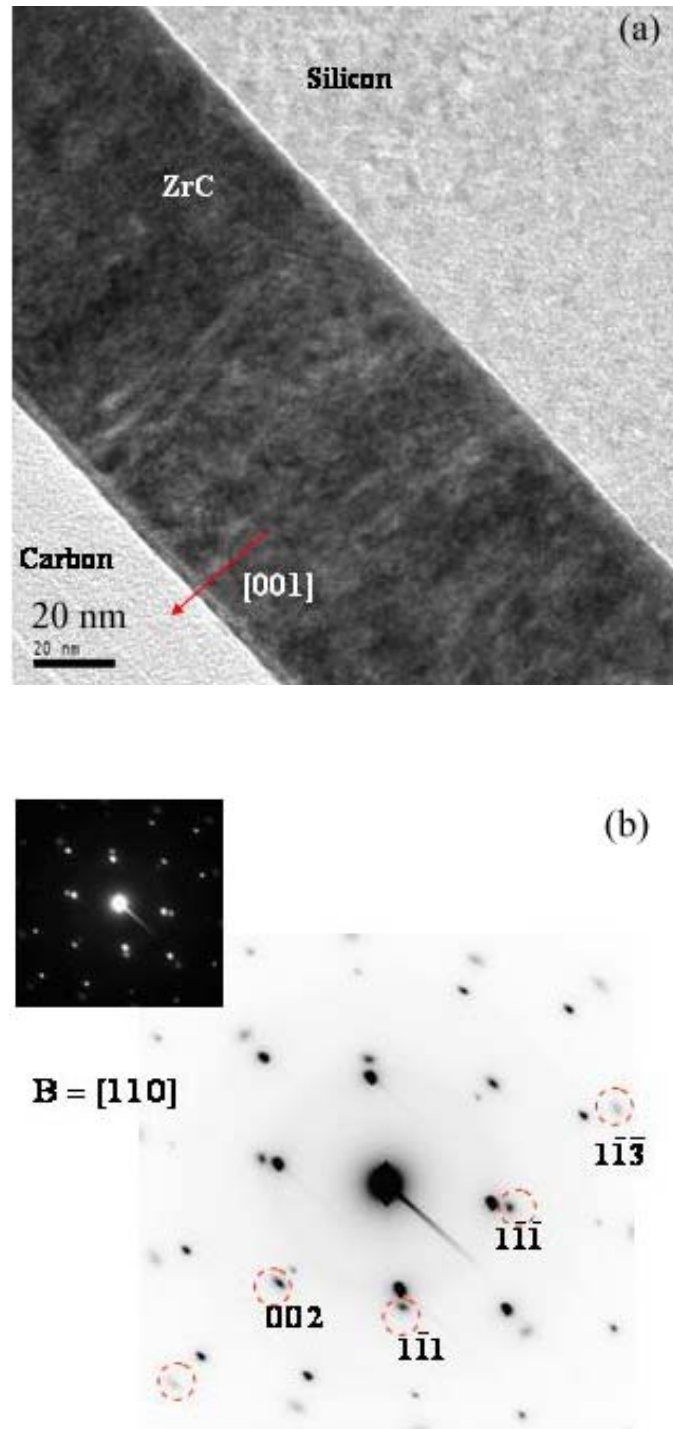


Figure 4-25. TEM (a) bright field image and (b) SADP (selected area electron diffraction pattern) obtained from cross-section of ZrC film grown on silicon (001) substrate; diffraction pattern obtained from ZrC film is marked by circles.

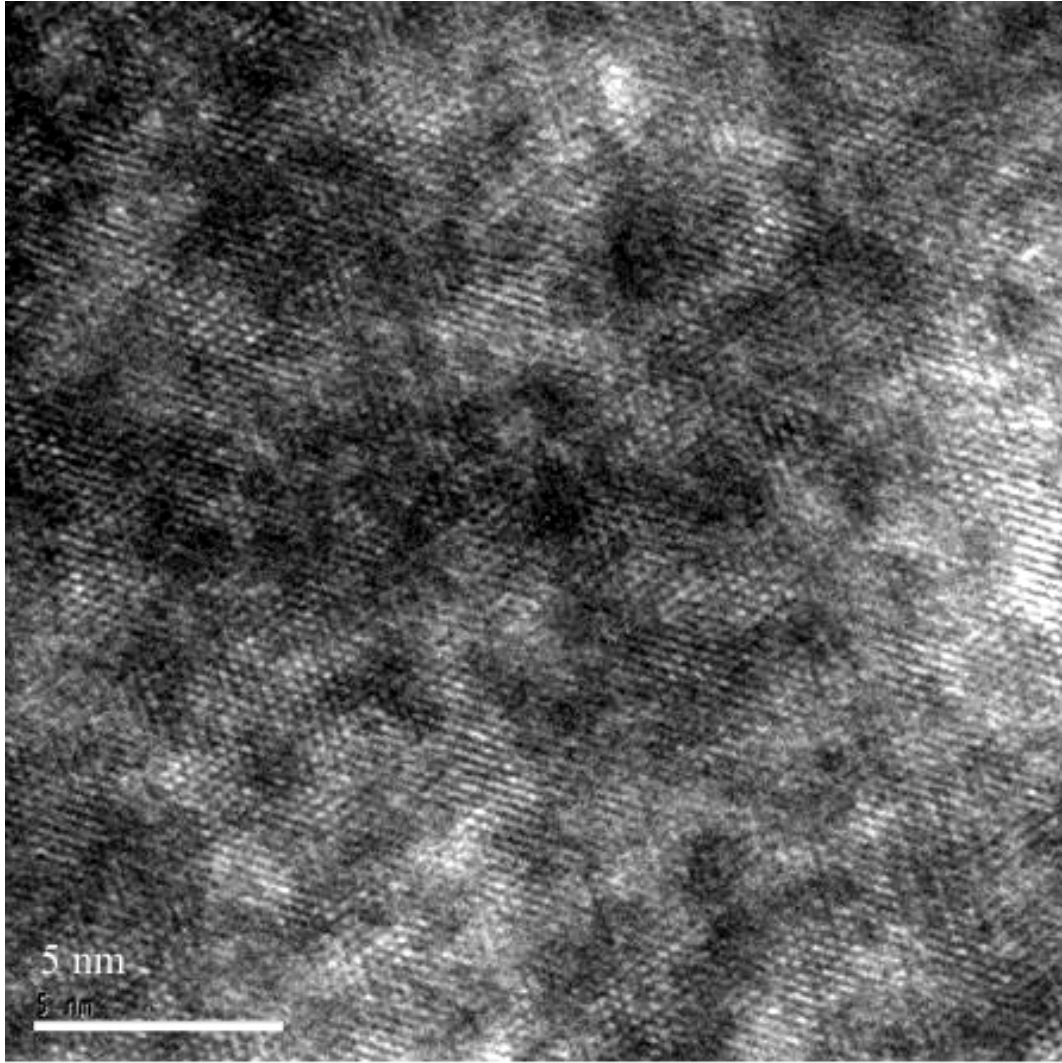


Figure 4-26. Bright field TEM image obtained from cross-section of ZrC film grown on silicon (001) substrate exhibiting clear lattice fringe.

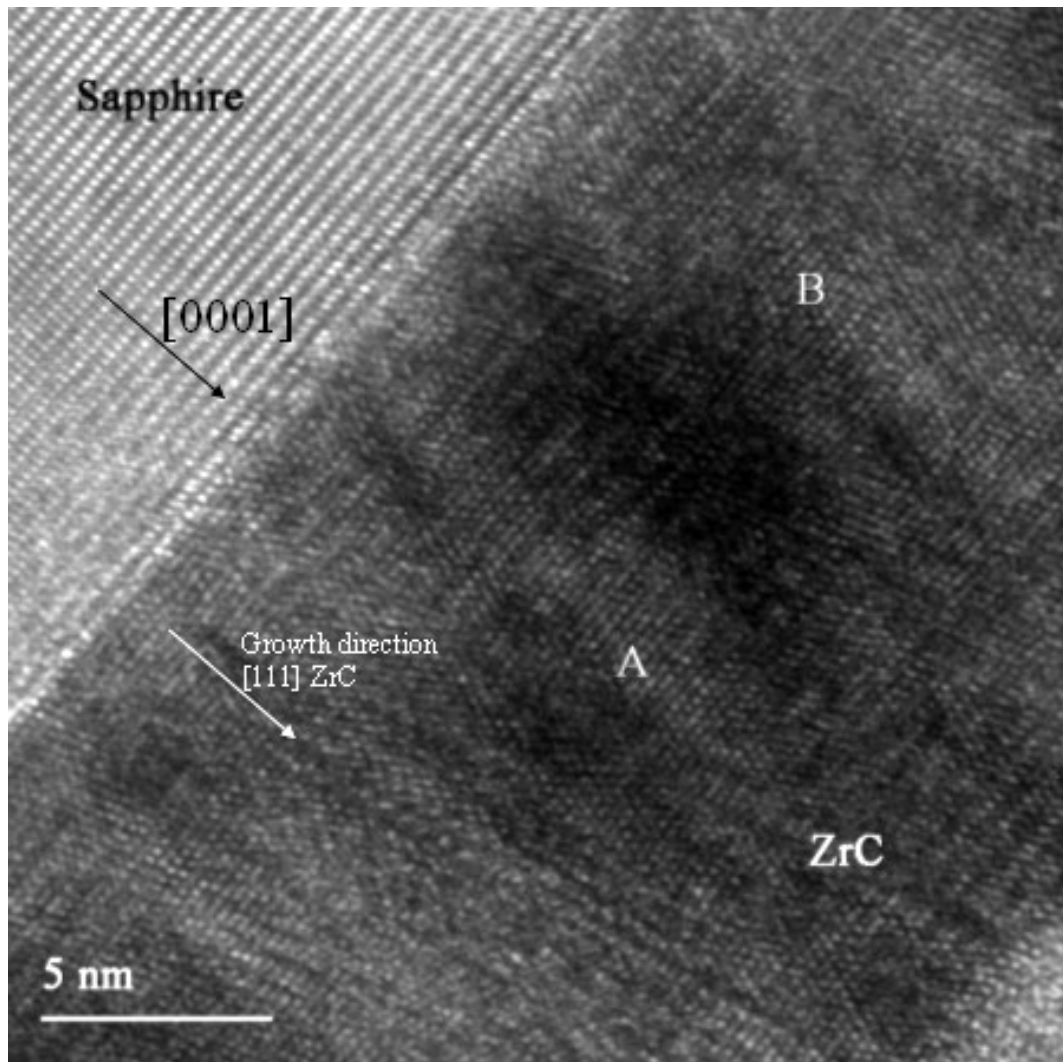


Figure 4-27. Bright field TEM image obtained from cross-section of ZrC film grown on sapphire (0001) substrate showing sharp interface; the regions marked as A and B are magnified in figure 4-28 for observation of twinning.

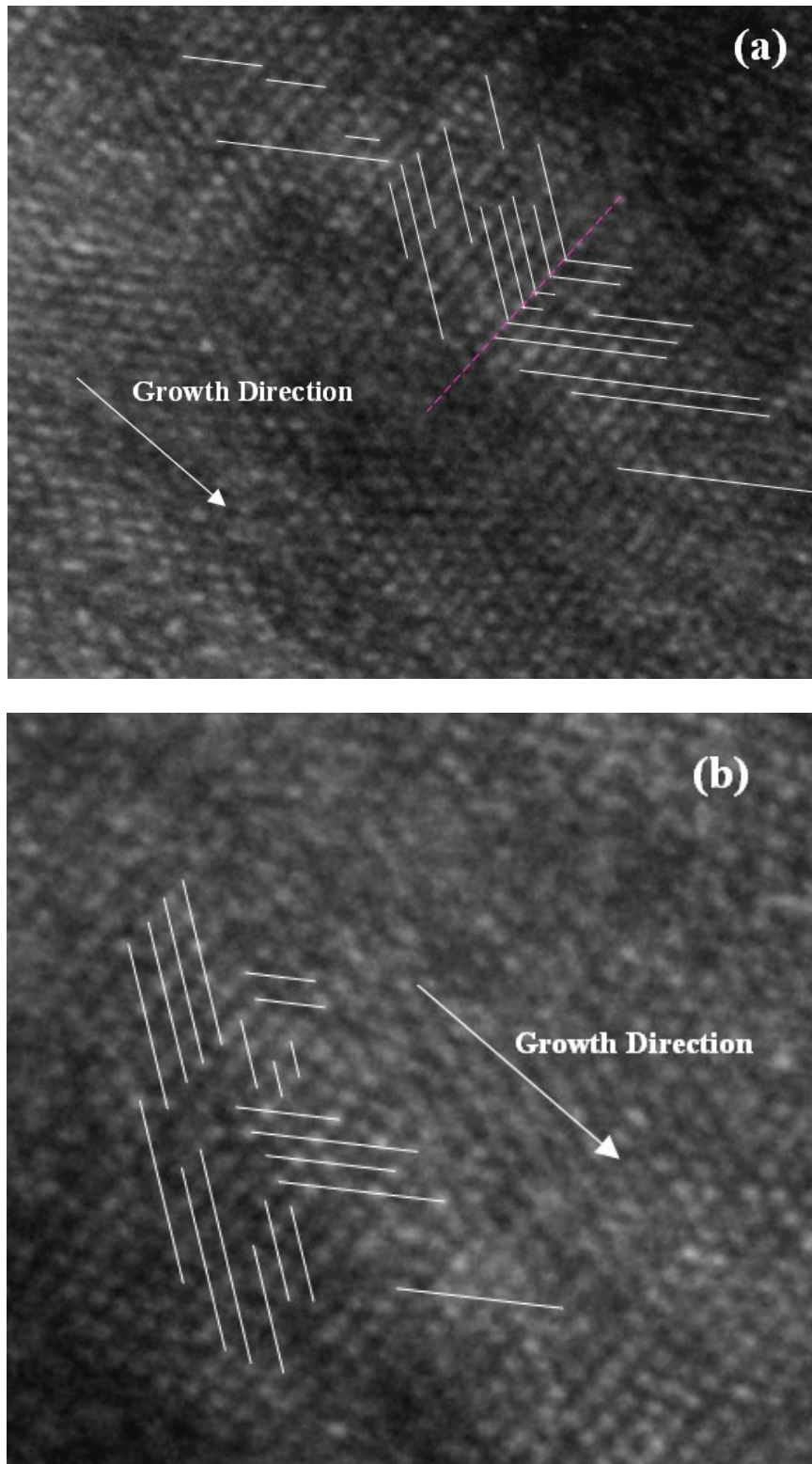


Figure 4-28. High resolution TEM image of (a) 'A' region in fig. 4-26, showing parallel twin to the surface of film; (b) 'B' region in fig. 4-26, showing perpendicular twin to the surface of film.

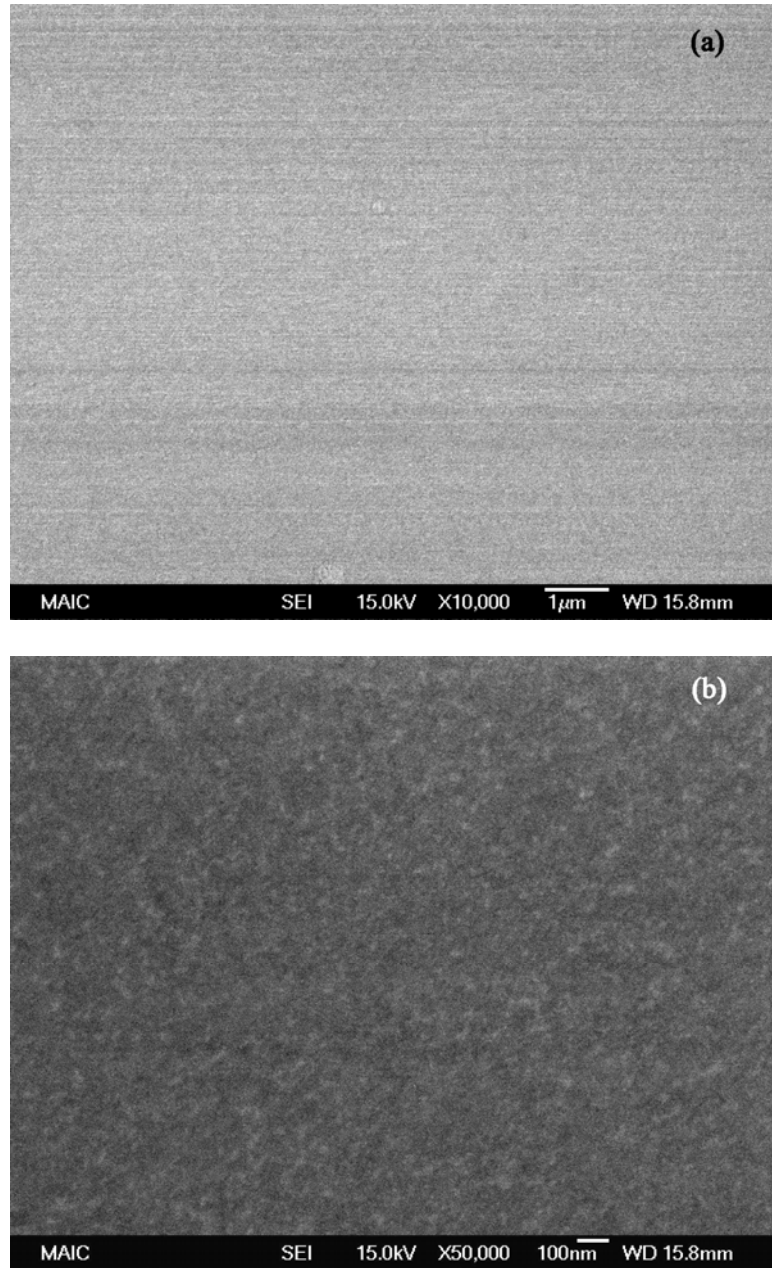


Figure 4-29. Secondary electron images of ZrC surface grown on Si (001) substrate, at  $\times 10\text{K}$  (a), and  $\times 50\text{K}$  (b).

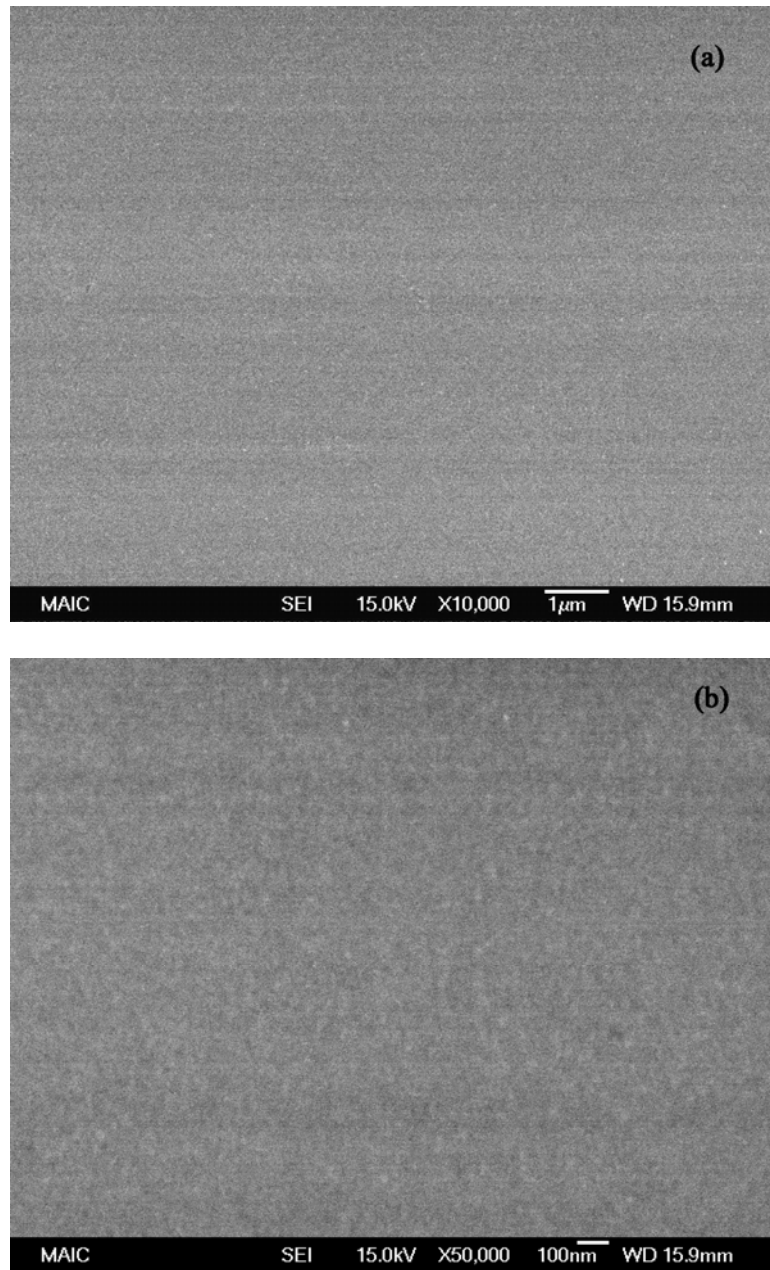


Figure 4-30. Secondary electron images of ZrC surface grown on sapphire (0001) substrate, at  $\times 10K$  (a), and  $\times 50K$  (b).

Peak Surface Area Summit Zero Crossing Stopband Execute Cursor

Roughness Analysis

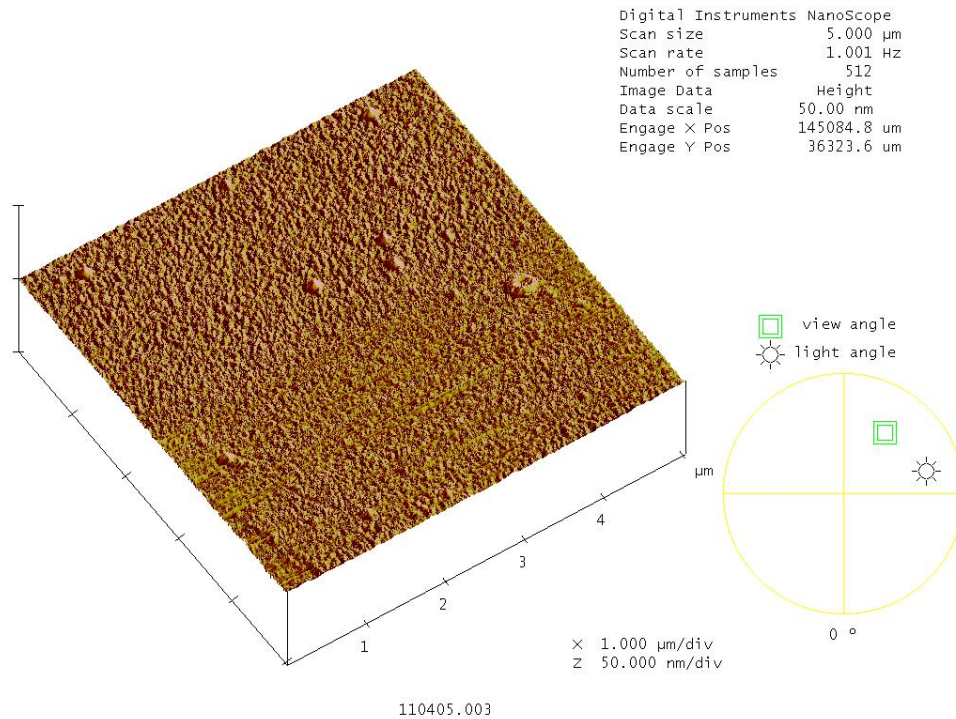
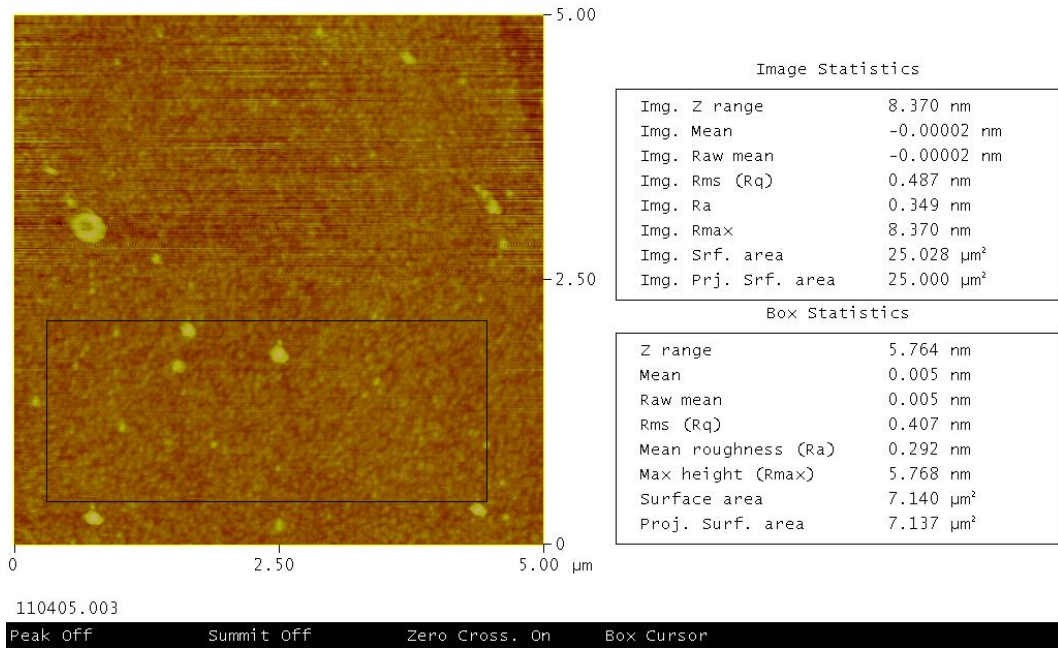


Figure 4-31. AFM height images obtained from the surface of ZC106 sample (ZrC (001) layer grown on Si (001) substrate)

Peak Surface Area Summit Zero Crossing Stopband Execute Cursor

Roughness Analysis

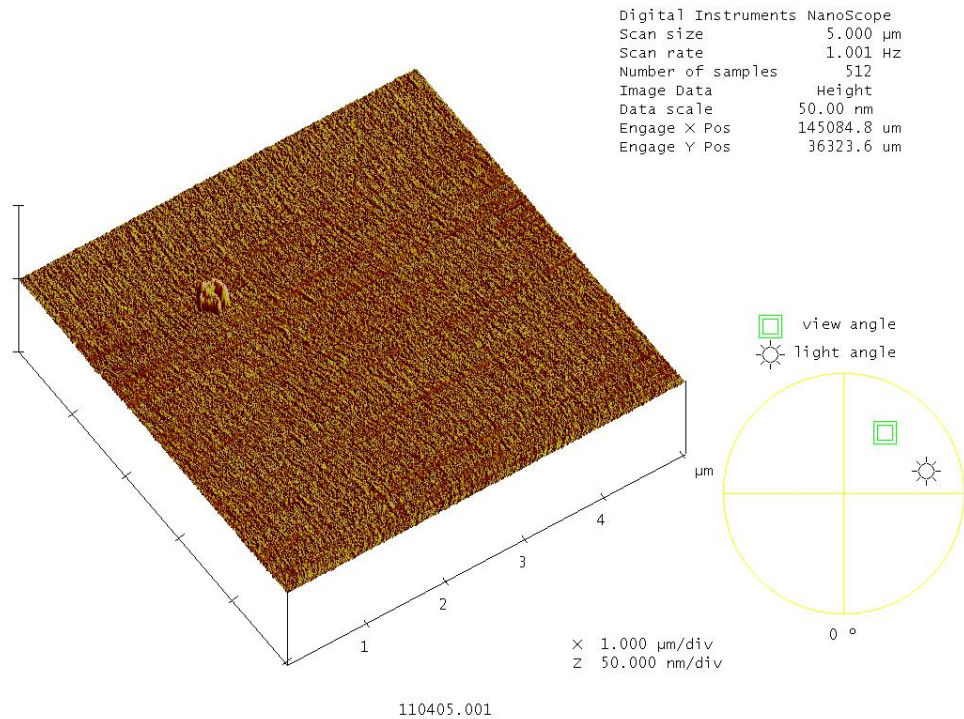
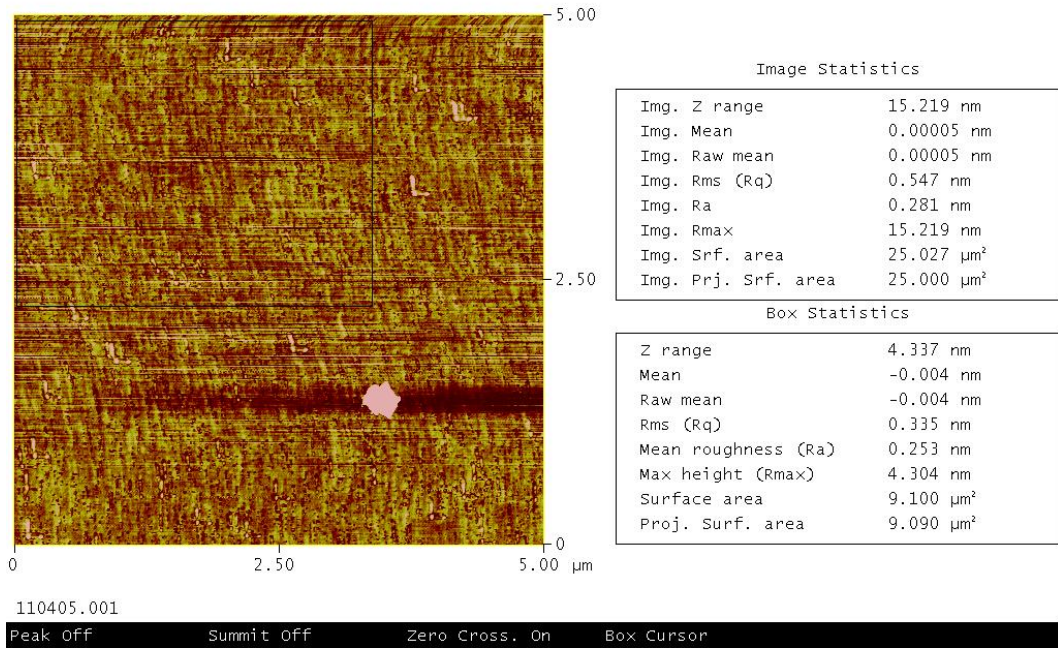


Figure 4-32. AFM height images obtained from the surface of ZC202 sample (ZrC (001) layer grown on Si (001) substrate)

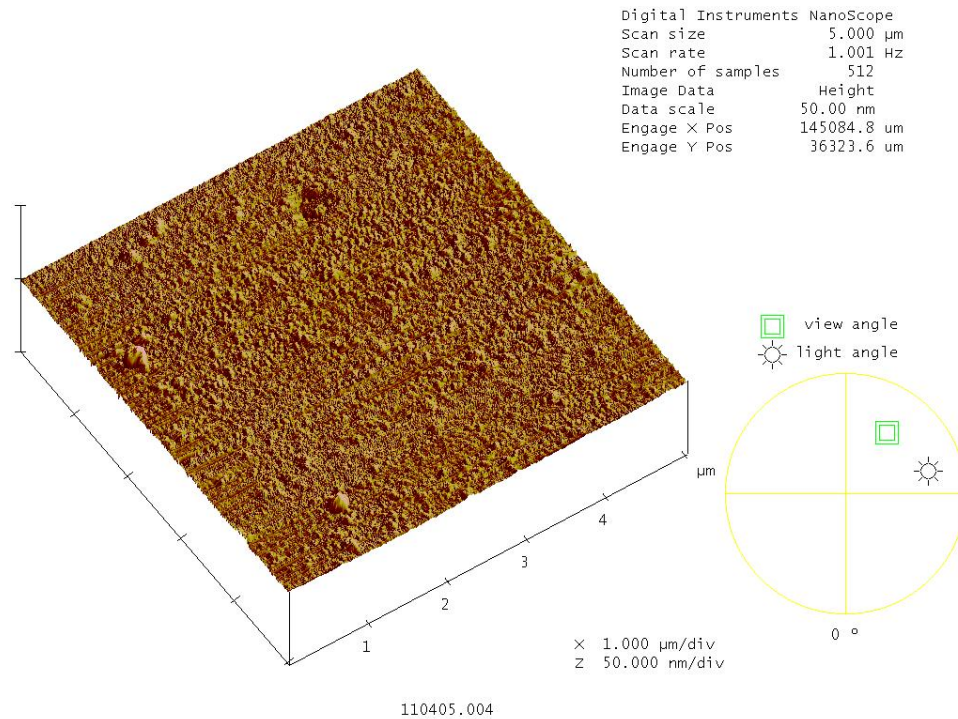
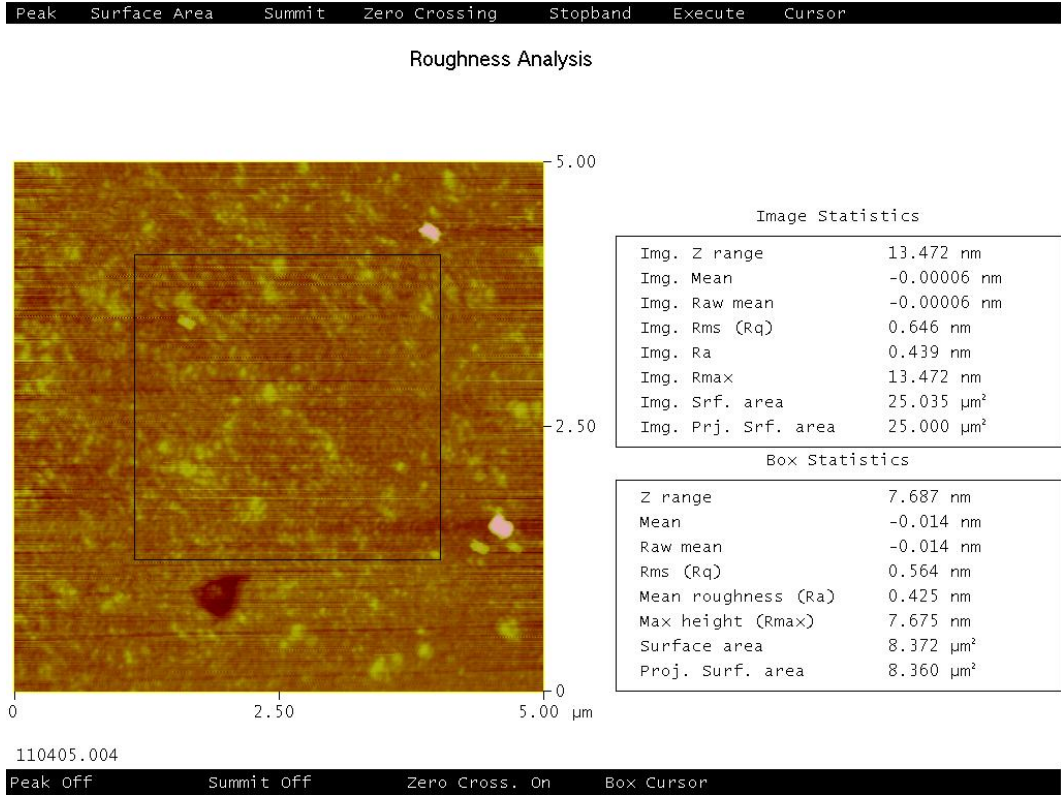


Figure 4-33. AFM height images obtained from the surface of ZC208 sample (ZrC (001) layer grown on Si (001) substrate)

Peak Surface Area Summit Zero Crossing Stopband Execute Cursor

### Roughness Analysis

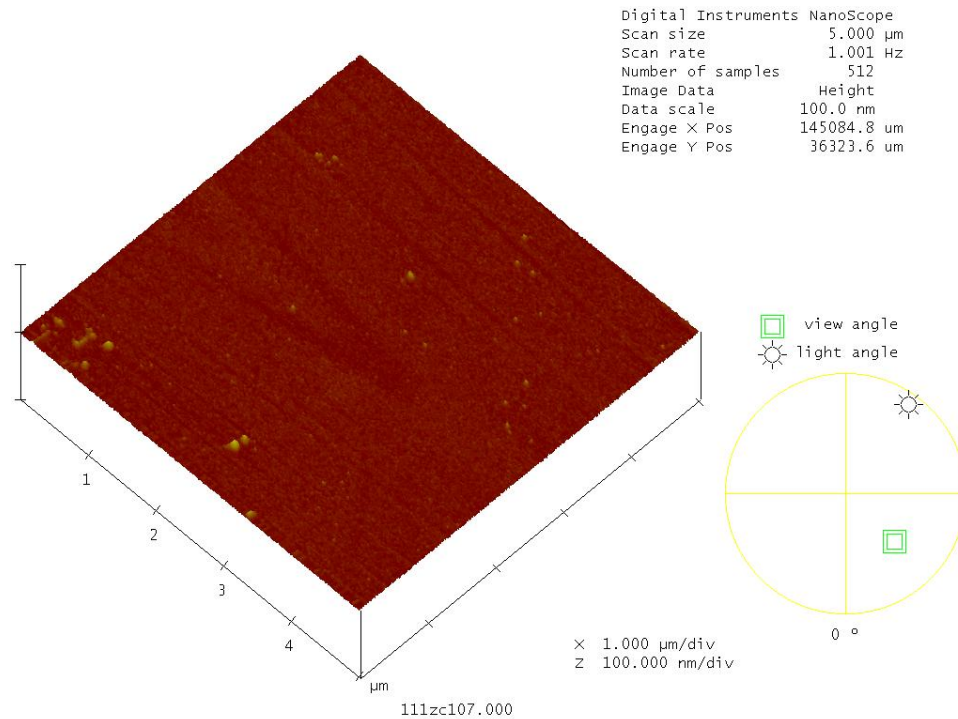
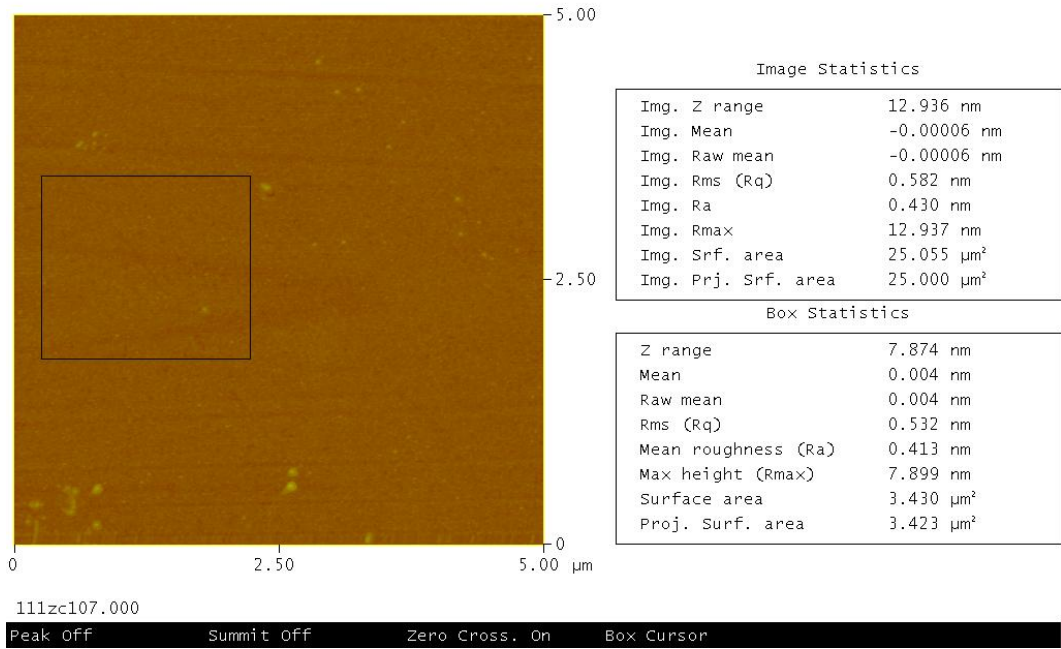


Figure 4-34. AFM height images obtained from the surface of ZC107 sample (ZrC (111) layer grown on Si (111) substrate)

Peak Surface Area Summit Zero Crossing Stopband Execute Cursor

Roughness Analysis

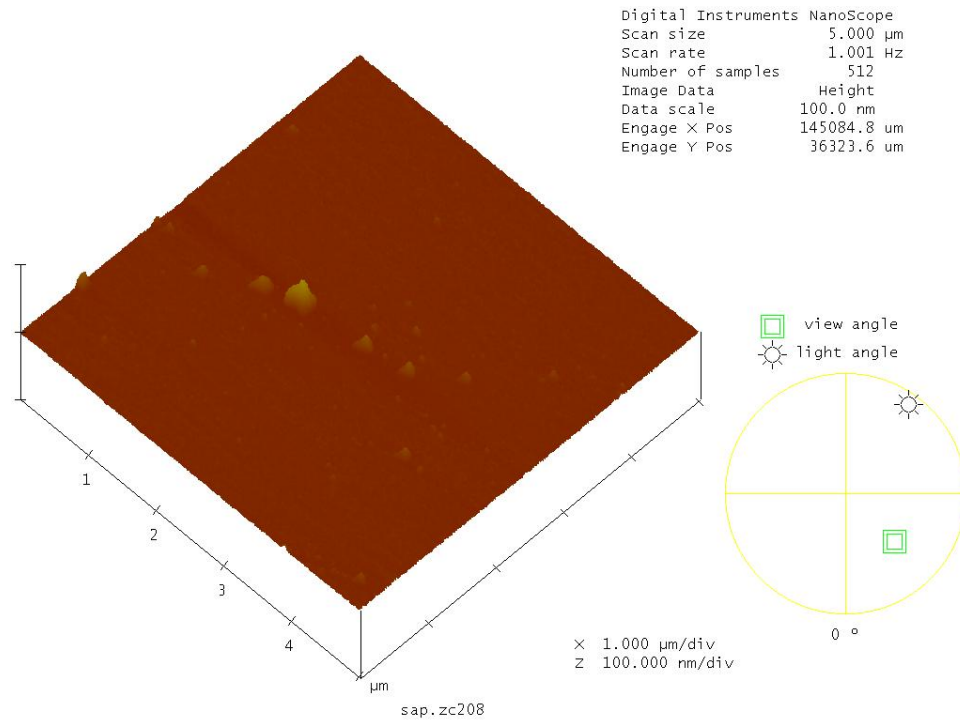
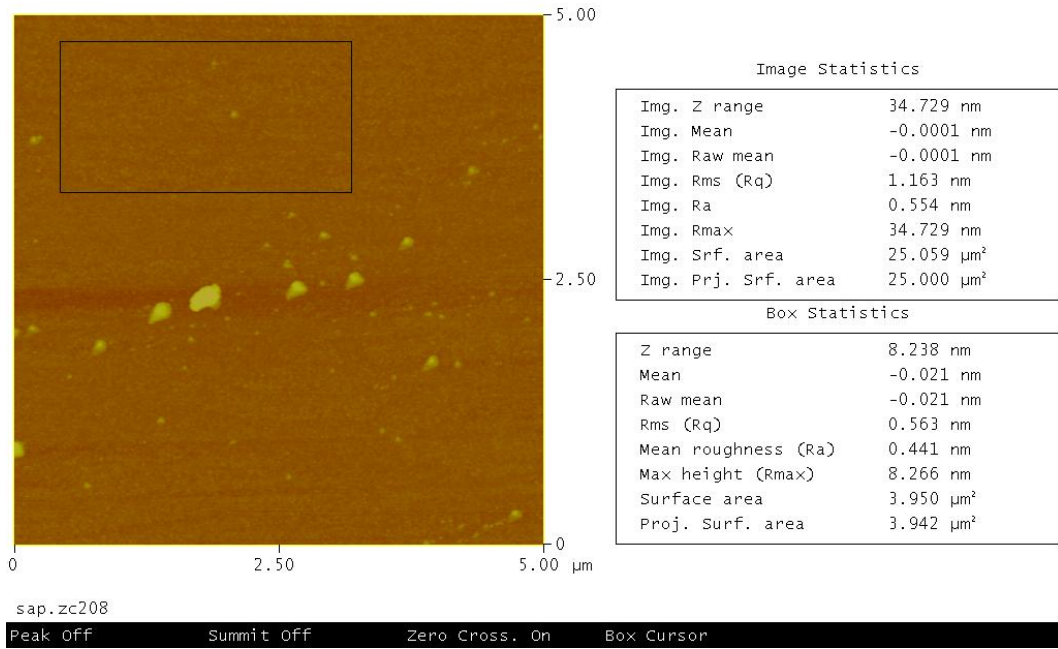


Figure 4-35. AFM height images obtained from the surface of ZC208 sample (ZrC (111) layer grown on sapphire (0001) substrate)

Peak Surface Area Summit Zero Crossing Stopband Execute Cursor

Roughness Analysis

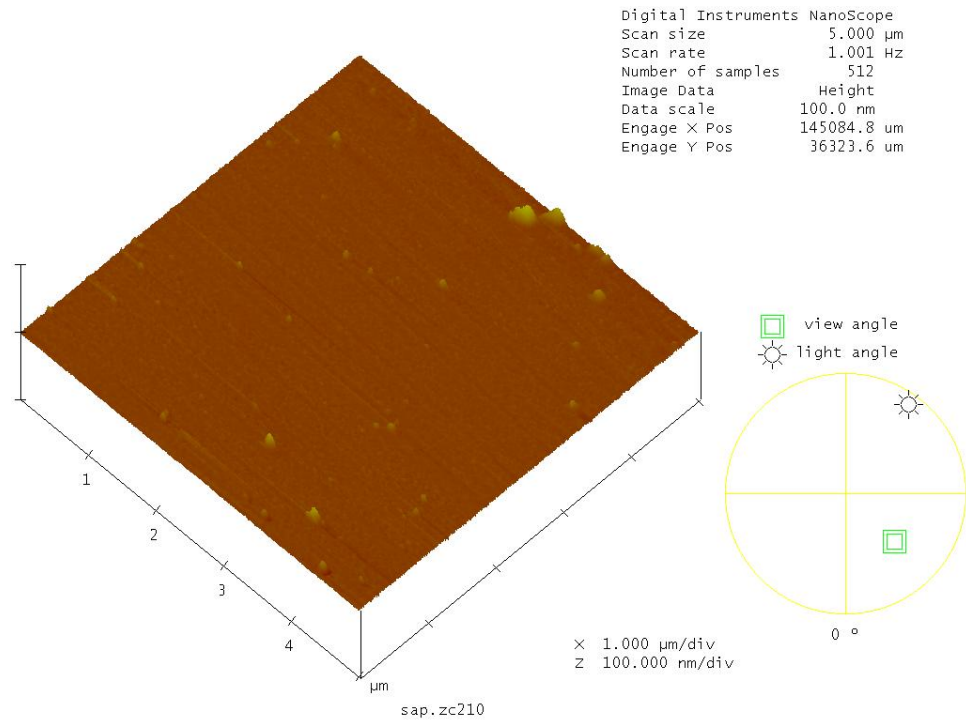
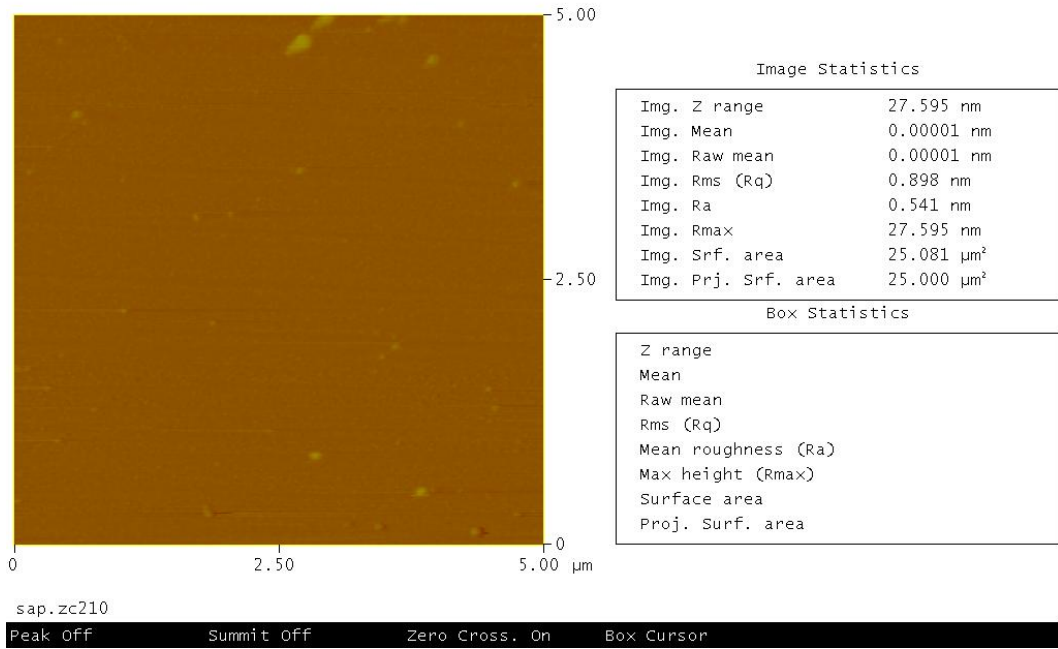


Figure 4-36. AFM height images obtained from the surface of ZC210 sample (ZrC (111) layer grown on sapphire (0001) substrate)

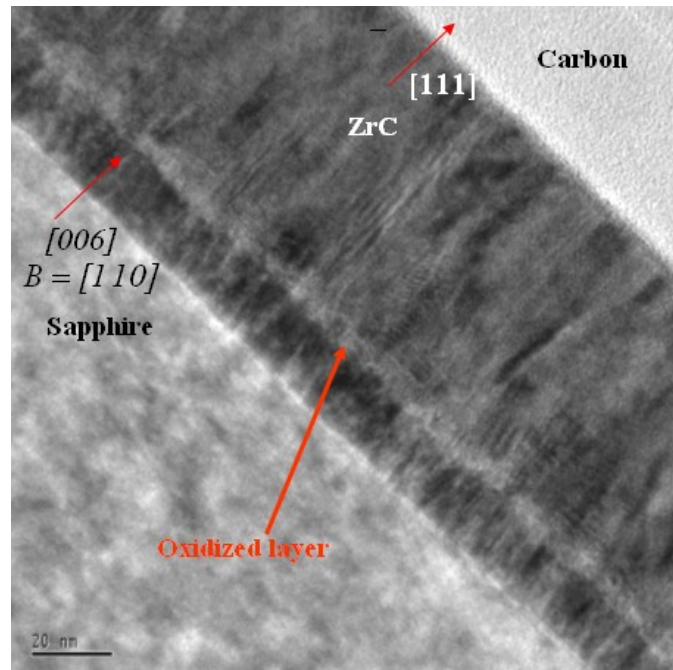


Figure 4-37. Cross-sectional bright field TEM image showing an oxidized layer due to discontinued growth.

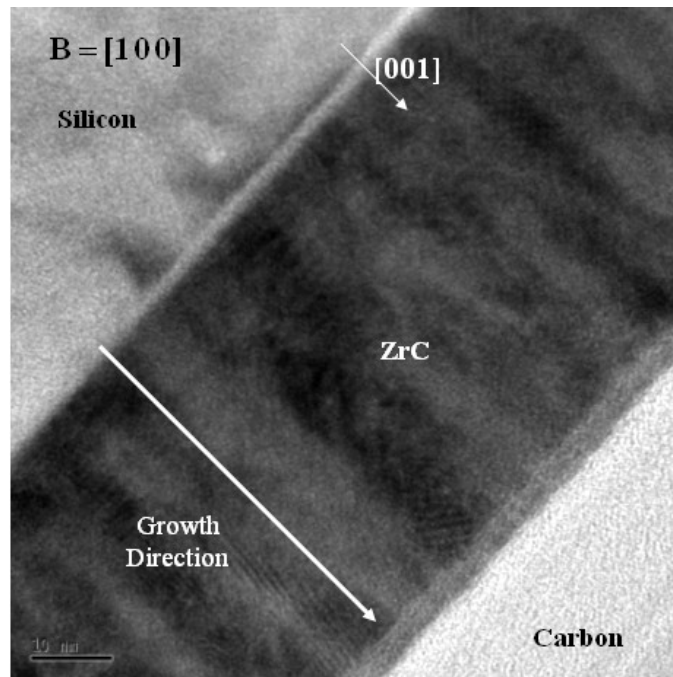


Figure 4-38. Cross-sectional bright field TEM image showing distinguishable three layers, also supporting a model used for XRR analysis.

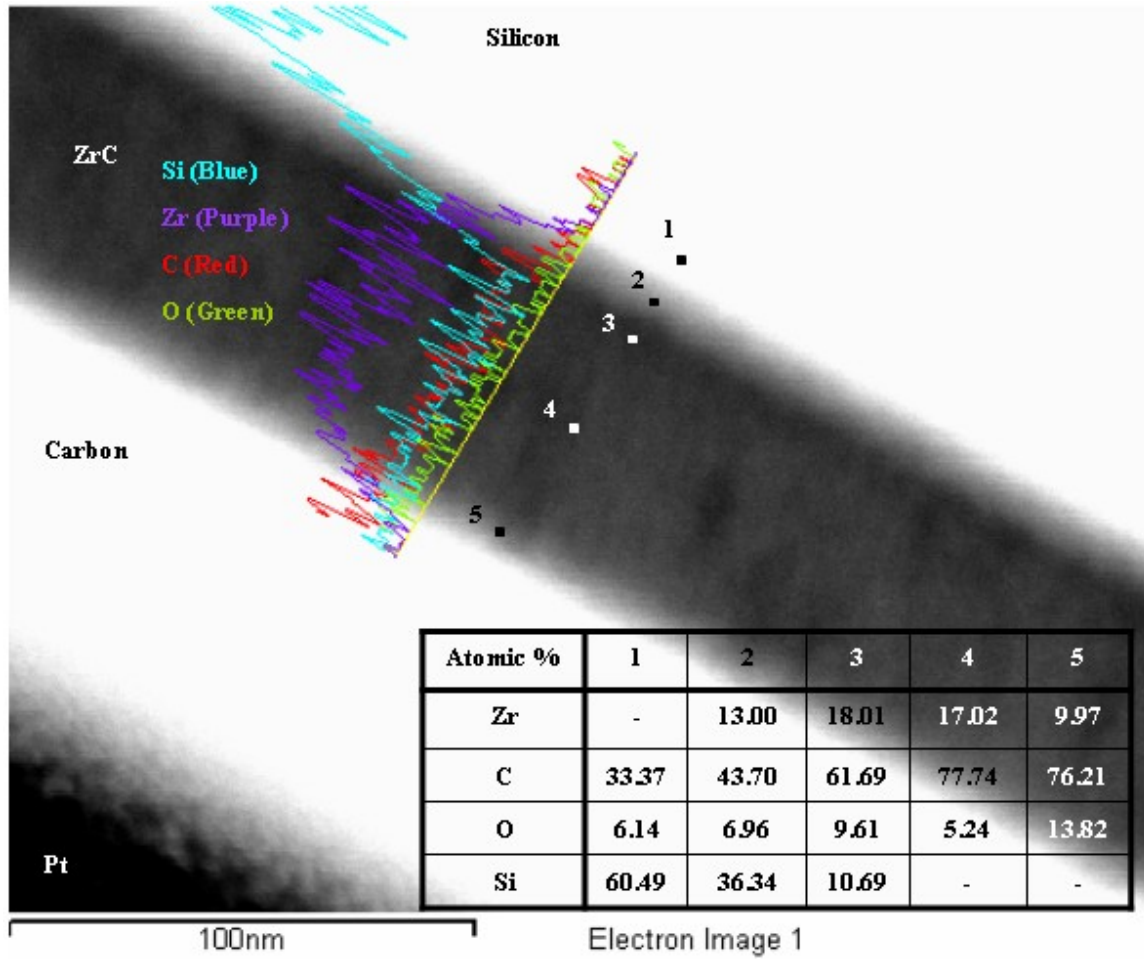


Figure 4-39. Z-contrast image of cross-sectional ZC106 sample for TEM-EDX analysis by line and point scan.

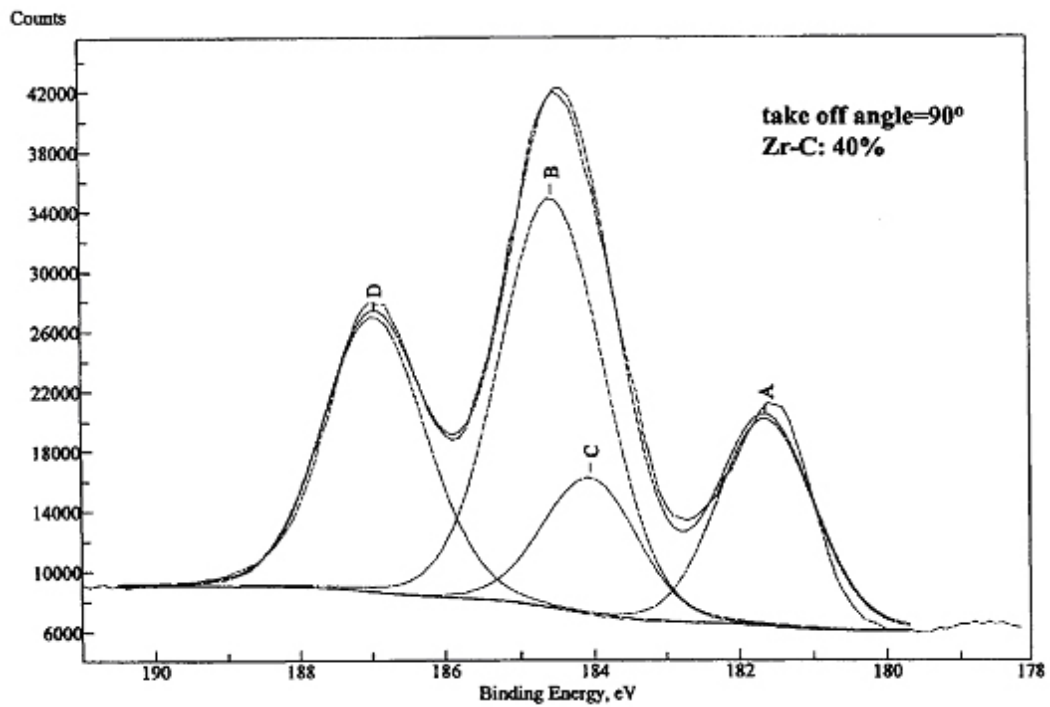
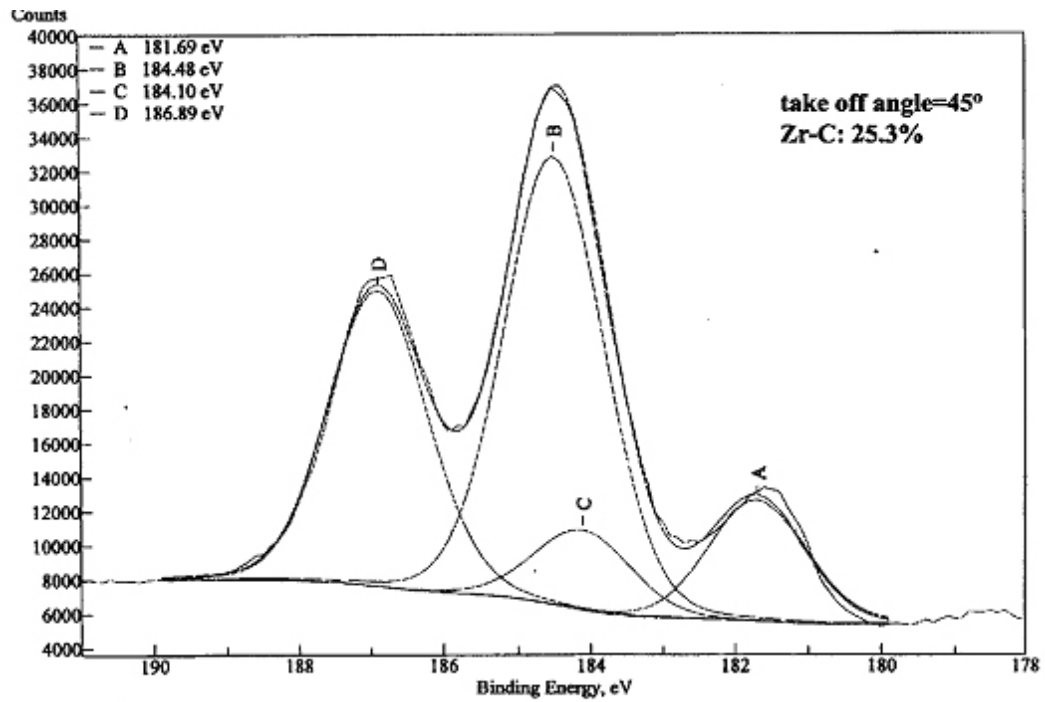


Figure 4-40. High resolution Zr 3d spectra acquired at 45° and 90° take off angles and their fitting for an as-received sample deposited at 600 °C under vacuum.

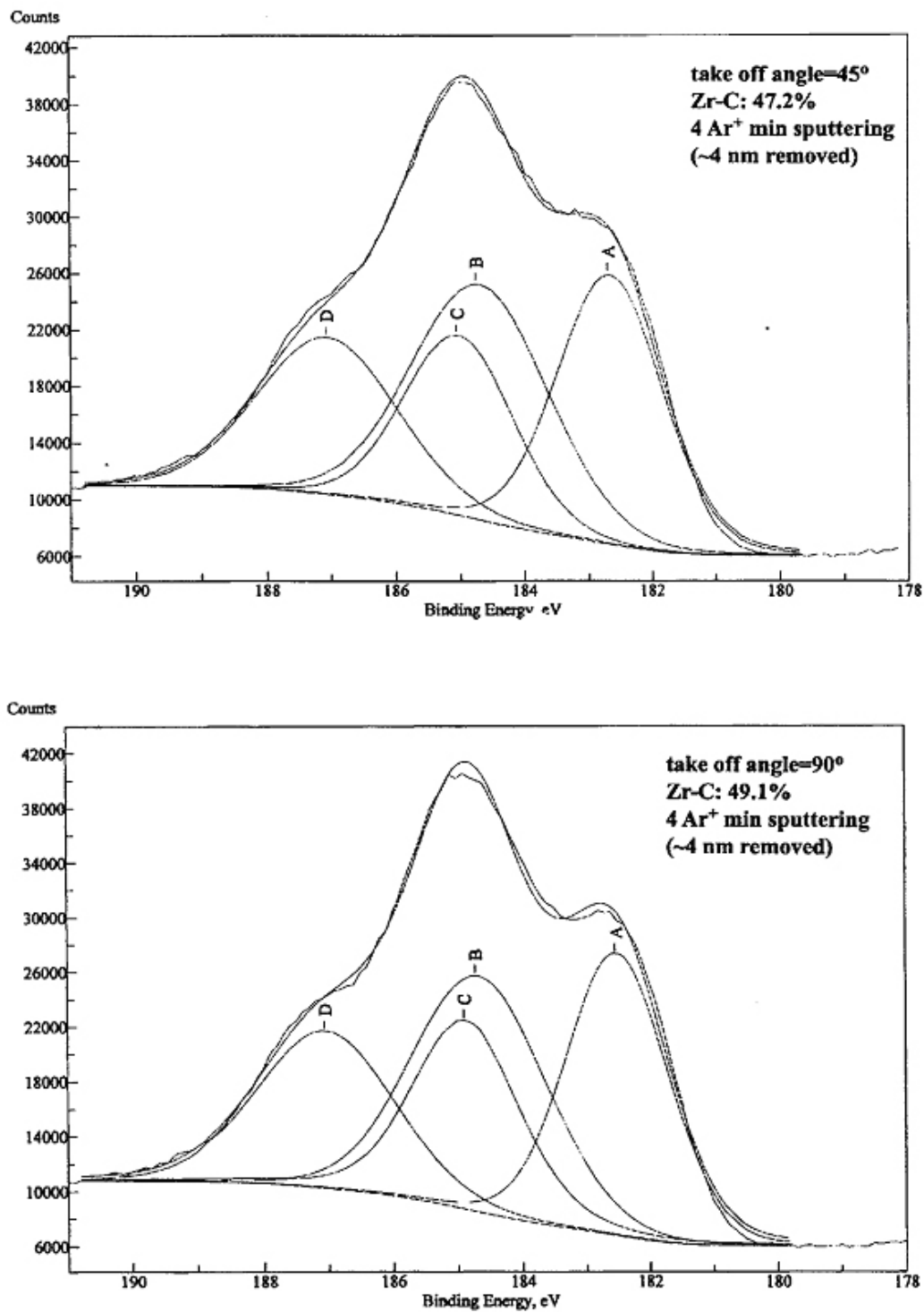


Figure 4-41. High resolution Zr 3d spectra acquired at 45° and 90° take off angles and their fitting for a sample deposited at 600 °C under  $1 \times 10^{-4}$  Torr of  $C_2H_2$  that was sputtered-clean by  $Ar^+$  bombardment.

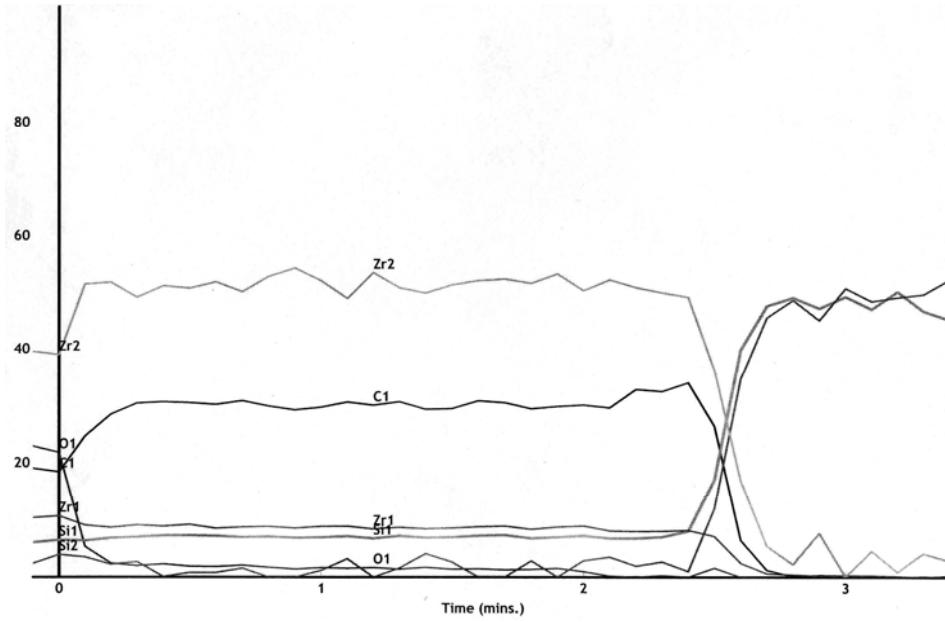


Figure 4-42. AES depth profile of an as-deposited ZrC film.

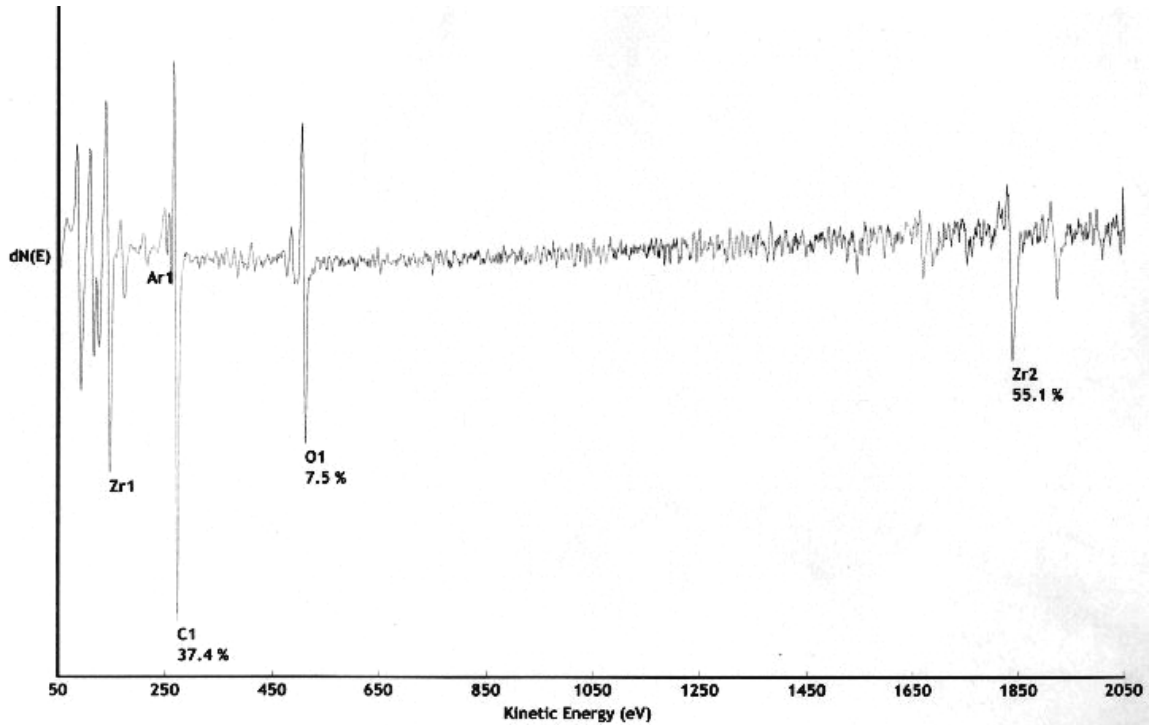


Figure 4-43. AES survey spectrum of a ZrC film (ZC202) sputtered with a 4 kV Ar ion beam.

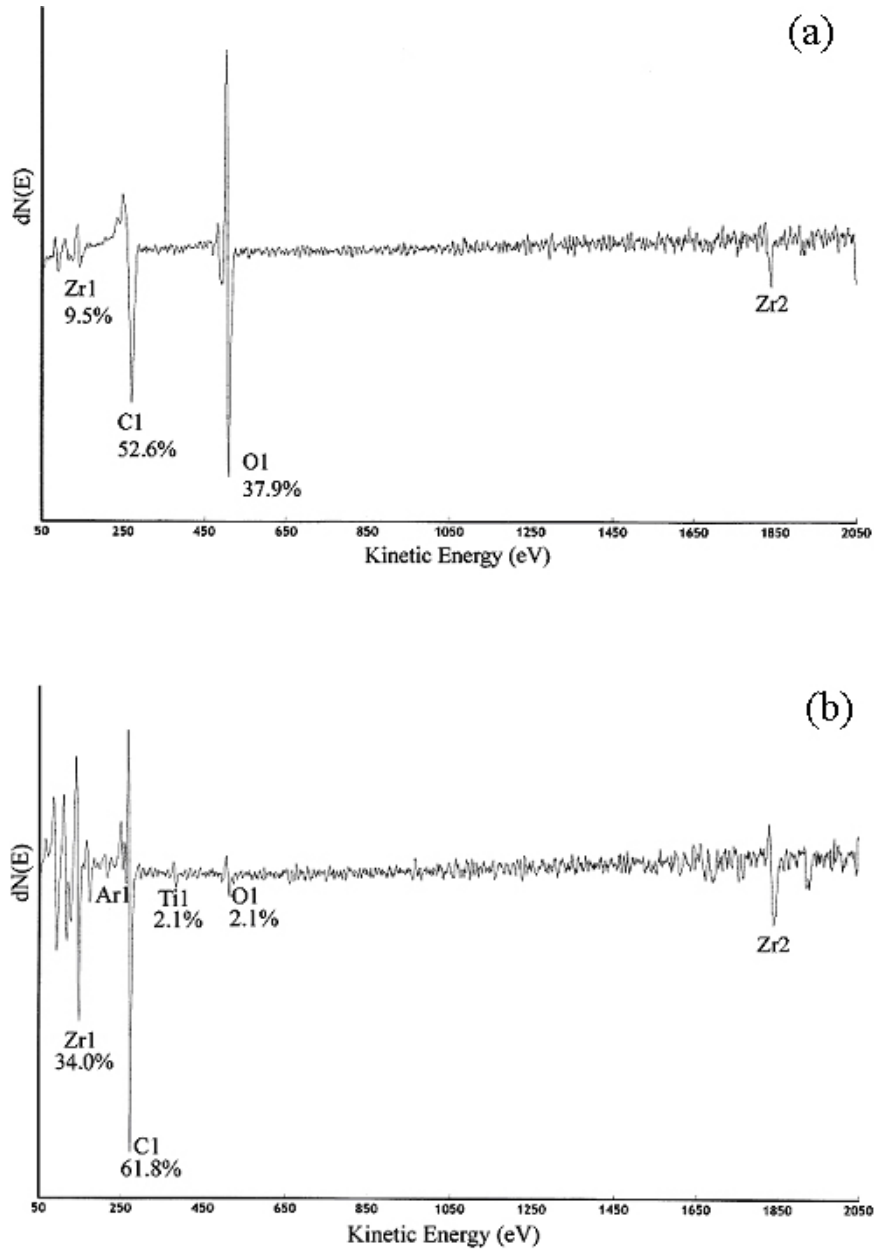


Figure 4-44. AES survey spectrum of (a) a as-deposited ZrC film under  $\text{CH}_4$  atmosphere and (b) the ZrC film sputtered for 1 min with a 4 kV Ar ion beam.

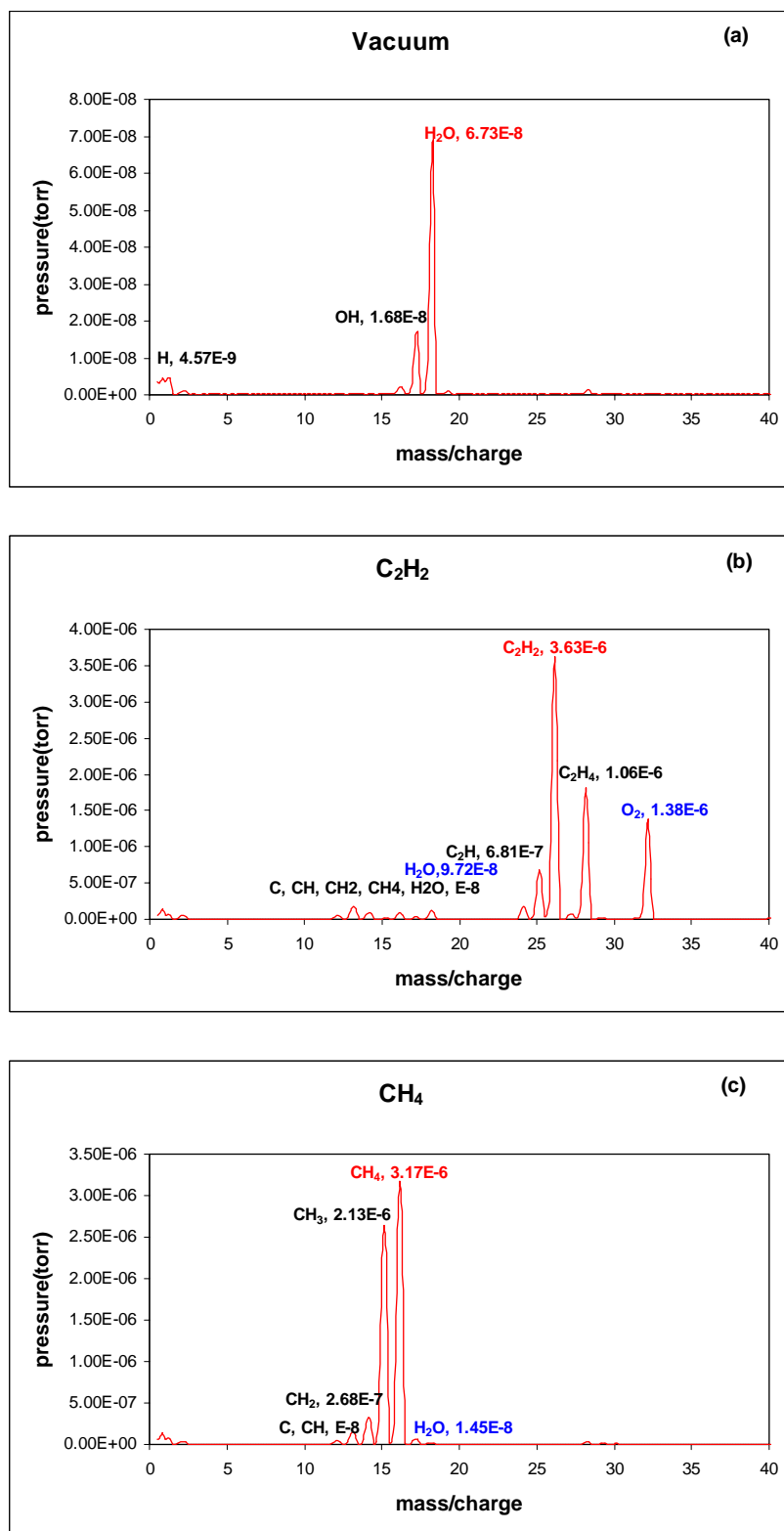


Figure 4-45. Residual gas partial pressure analyzed by RGA before deposition at (a) vacuum and right after introducing (b)  $\text{C}_2\text{H}_2$  and (c)  $\text{CH}_4$ .

CHAPTER 5  
MECHANICAL PROPERTIES OF ZIRCONIUM CARBIDE FILMS MEASURED BY  
NANOINDENTATION

**5.1 Introduction**

Zirconium carbide, as mentioned before, is a potentially important material for many applications because its properties including hardness, melting point, corrosion resistance, and abrasion resistance are outstanding. Therefore, ZrC films could be used for MEMS (micro electro-mechanical system) device as wear-resistant or protecting coating, or in electronic device. As one of examples as application in electronic device, ZrC deposited on Si can substitute currently using ZrN as a diffusion barrier in Cu-Si system for metallization application. ZrC also exhibits lower lattice mismatch and thermal expansion coefficient difference with Si compared to ZrN. In addition, epitaxially grown crystal ZrC could prevent copper diffusion into Si substrate along the localized defects in the barrier films. In consequence, the failure of Cu/ZrC/Si films could be avoided by retarding the formation of  $\text{Cu}_3\text{Si}$ . Also tip failure by ion bombardment in currently using Si and Mo field emitters is one of problems in stabilizing field emission for a long time. The impact of ion bombardment onto surface creates sharp nanoprotusions which are resulting in tip failure caused by high local field [Cha99, Cha01]. From this point of view, ZrC is promising material for a field emitter tip application because of its low work function as well as high resistance to ion bombardment. Therefore, it is important to investigate the mechanical properties of deposited thin film ZrC.

One of the most challenging for task applications of thin films is to evaluate their mechanical properties. The nanoindentation has been used as a very useful technique to quantify thin-film mechanical properties, such as Young's modulus and hardness, within a submicron scale [Cac99, Kuc00, Now99, Yu98]. In the standard indentation procedure, a Berkovich pyramid-shaped diamond tip using  $\mu\text{N}$  loads produces submicrometer indentation penetration depths, and allows the properties of thin films to be measured without removing the substrate. Apparently, this technique has become an important tool for material characterizations because one can easily obtain the reduced modulus and hardness values of thin films under different loads from their load-displacement (P-h) curves [Tsu99].

In this study, ZrC films grown on Si (100), Si (111), and sapphire (0001) substrates using pulsed laser deposition were investigated using nanoindentation measurement. The Young's modulus and hardness were calculated from loading-displacement (P-h) curves.

## 5.2 Experiment

The film depositions were conducted in a stainless steel vacuum chamber using a KrF excimer laser. The laser parameters used were  $10 \text{ J/cm}^2$  fluence and 10 Hz repetition rate. ZrC films were deposited on and Si (001), Si (111), and sapphire (0001) substrates. Depositions were performed under a low  $\text{C}_2\text{H}_2$  or  $\text{CH}_4$  atmosphere. Details for deposition procedures are described in chapter 4.

Automated indentation pattern grids with indentation spacing of  $5 \mu\text{m}$  were programmed to run on original substrates and coated substrates with a Hisitron TriboIndenter. Tests were run in displacement control with a total displacement range of 15 to 70 nm. The samples thicknesses used for nanoindentation test were around 70~100 nm. The sample surfaces were carefully cleaned before the measurements. A Berkovich

diamond indenter (a three-sided pyramidal-diamond tip) with a total included angle of 142.3°, a half angle of 65.3°, and a tip radius of 100~200 nm was used for indentation. A tip area function was generated by curve fitting a plot of area vs. contact depth from indentations on a fused quartz standard with modulus of 72 GPa and a Poisson's ratio of 0.168. Unloading force displacement curves were analyzed to determine reduced modulus and hardness using a method first described by Doerner and Nix [Doe86] and later refined by Oliver and Pharr [Oli92].

### 5.3 Nanoindentation Test

The term, the indentation or reduced modulus ( $E_r$ ), is introduced to balance the Young's modulus of specimen ( $E$ , film + substrate), and that of the diamond indenter ( $E_i$ ) [Oli92]. That is, elastic modulus is determined from:

$$E_r = \frac{\sqrt{\pi}}{2} S \frac{1}{\sqrt{A_c}} = \frac{(1-\nu^2)}{E} + \frac{(1-\nu_i^2)}{E_i} \quad (5-1)$$

$$S = \frac{dP}{dh} \quad (5-2)$$

where  $S$  is the slope at the beginning of the unloading curve, and  $A_c$  is the corresponding projected contact area, in addition,  $\nu$  and  $\nu_i$  are Poisson's ratio of specimen and indenter, respectively. For diamond,  $E_i = 1,070$  GPa and  $\nu_i = 0.07$ . The Poisson's ratios and Young's modulus was compared to reference data in table 5-1.

To determine the area function, a series of indents at various contact depths were performed on fused quartz specimen, and then the contact area was calculated using eq. (5-1). A fitting procedure is employed to plot the computed area as a function of contact depth ( $h_c$ ) to a sixth order polynomial of eq. (5-3).

$$A = C_0 h_c^2 + C_1 h_c + C_2 h_c^{1/2} + C_3 h_c^{1/4} + C_4 h_c^{1/8} + C_5 h_c^{1/16} \quad (5-3)$$

$C_0$  for a Berkovich tip is 24.5. Area function used for data calculation is displayed in fig. 5-1. Since this calculation is based on the assumption that Young's modulus of fused (or amorphous) quartz is constant and independent of indentation depth, and mathematical fitting is not perfect in whole range of depth, the result deduced could be erroneous especially in the thin depth region rather than in deep region. An example of an erroneous tip area function calculation is shown in fig. 5-2. Therefore, data below the contact depth of 5 nm were excluded in calculating mechanical properties.

Table 5-1. Poisson's ratio and Young's modulus of Al<sub>2</sub>O<sub>3</sub> (poly), Si, and diamond tip.

	E (GPa)	$\nu$
Al <sub>2</sub> O <sub>3</sub> (poly)	~400 [Asm01]	~0.23 [Asm01]
Si (111)	185 [Wor65]	0.18 [Wor65]
Si (001)	130 [Wor65], 179~202 [Bhu96]	0.279 [Wor65]
Diamond tip	1070	0.07

Hardness (H) in depth sensing indentation is determined by applying a maximum indentation load ( $P_{\max}$ ), while bulk hardness is calculated by residual contact area.

Hardness in nanoindentation measurement is defined by:

$$H = \frac{P_{\max}}{A_c} \quad (5-4)$$

In analyzing data, some erroneous data were removed, and a correction was conducted by shifting data points to set onset of the loading and displacement at zero.

## 5.4 Result and Discussion

### 5.4.1 Hardness and Young's Modulus of Substrates

To compare hardness and elastic modulus between substrate and film, hardness and elastic modulus of substrates was measured. Modulus of substrate can be calculated from

eq. (5-1) by replacing  $E$  and  $\nu$  with  $E_s$  and  $\nu_s$ , where  $E_s$  is Young's modulus of substrate, and  $\nu_s$  is Poisson's ratio of substrate. Calculated results of hardness and Young's modulus are shown in fig. 5-3 and fig. 5-4, respectively. The Poisson's ratios used in calculation were all 0.2. Error range of calculated Young's modulus by eq. (5-1) is only  $\pm 5\%$  in the range of  $0 < \nu_s < 0.3$ , when a diamond tip is used, and when  $\nu_s = 0.2$  is used (fig. 5-5).

The results of elastic modulus for silicon substrate were somewhat higher than theoretically calculated data [Wor65], but very similar to other empirical nanoindentation result [Bhu96] in table 5-1. Load vs. displacement curves of Si (001) and Si (111) substrate are displayed in fig. 5-6 and fig. 5-7, respectively. For sapphire substrate, there was a 'pop-in' phenomenon in load-displacement curve, as it is shown in fig. 5-8. The 'pop-in' phenomenon could be thought as creep behavior or yield of the material. But in displacement control method, it could be thought as yield of material because there is no dwell time at a certain load, contrary to load control method. Total elastic behavior before 'pop-in' in fig. 5-9 supports yield phenomenon. Therefore, hardness measurement can not be correct in the whole range because hardness measurement is based on plastic deformation of materials. To make corrections in the measurement, displacement curve should be shifted to left, to set the onset of load at the extended line from on-load curve after 'pop-in'. However, since knowing that the hardness of sapphire responded in the range of 20~50 GPa before yield was enough, the hardness of bulk sapphire was not obtained in this study. On the other hand, Young's modulus measurement is based on unloading curve, so this data is still available for analysis of elastic modulus of ZrC film.

#### 5.4.2 Hardness and Elastic Modulus of ZrC Films Deposited on Si (001), Si (111), and Sapphire

The elastic modulus of combined film and substrate as a function of contact depth was calculated from the measured reduced modulus using eq. (5-1), assuming that the compliance of specimen (film + substrate) and indenter is combined as springs in series [Oli92]. The value 0.2 as combined Poisson's ratio for film and substrate was used for elastic modulus calculation. The values measured from ZrC (001) films on Si (001) substrate and their load-displacement curve are displayed in fig. 5-10 ~ fig. 5-12. As one can see in fig. 5-10, as the contact depth is increased (hence applied force), the values of the elastic modulus are approaching the values measured for the substrates. Since the combined film and substrate modulus is strongly decreasing with the depth of penetration from the value of the modulus of the hard film towards that of the softer substrate system as shown in fig 5-13 [Men97], a value of over 450 GPa of elastic modulus can be estimated for the highest crystalline quality (001) ZrC (film thickness,  $t \sim 100$  nm) on Si (001). For relatively thinner and lower crystalline quality ( $t \sim 70$  nm) samples, a lower value of over 300 GPa of elastic modulus can be estimated. Similarly, a value of  $\sim 450$  GPa for the highest quality films grown on sapphire and a value of  $\sim 300$  GPa for films grown on Si (111) can be estimated. The resulting combined elastic modulus data are displayed in fig. 5-14, which are calculated from the load-displacement curves in fig. 5-15 and fig. 5-16. In this case, the substrate effect was very dominant due to thickness of film or high sapphire elastic modulus, and the films moduli barely influenced the measurements.

Fig. 5-17 shows the variations of hardness as a function of normalized depth (= indenter displacement / film thickness) for a ZrC films and substrate system. In hard film

on soft substrate system, hardness increases at small indentation depth, and then it reaches at maximum value when normalized depth is 0.25, and it decreases with increasing indentation depth [Che05b]. Fig. 5-17 also shows a similar tendency, so the hardness data can be obtained around 0.25 of normalized indentation depth. The results show that the highest crystal quality films (ZC202: ~27 GPa, ZC204: ~31 GPa) exhibited higher hardness values than those of lower crystalline quality films (ZC210a: ~22 GPa, ZC210c: ~19GPa). This maximum ZrC hardness is comparable to the maximum hardness (30.2GPa) of nanocrystalline ZrC reported recently [Che05a].

### **5.5 Summary**

In summary, epitaxial ZrC films deposited by using the pulsed laser deposition technique were tested for hardness and elastic modulus using depth sensing nanoindentation. In nanoindentation measurement, surface cleanness, accurate area function, and indenter tip stability when approaching near surface were critical problems for obtaining correct data. Both hardness and elastic modulus were predominantly depending on films crystalline quality rather than their textures. A high value of hardness (~31 GPa) and elastic modulus (over 450 GPa) were obtained for high crystalline quality ZrC (111) deposited on sapphire substrate.

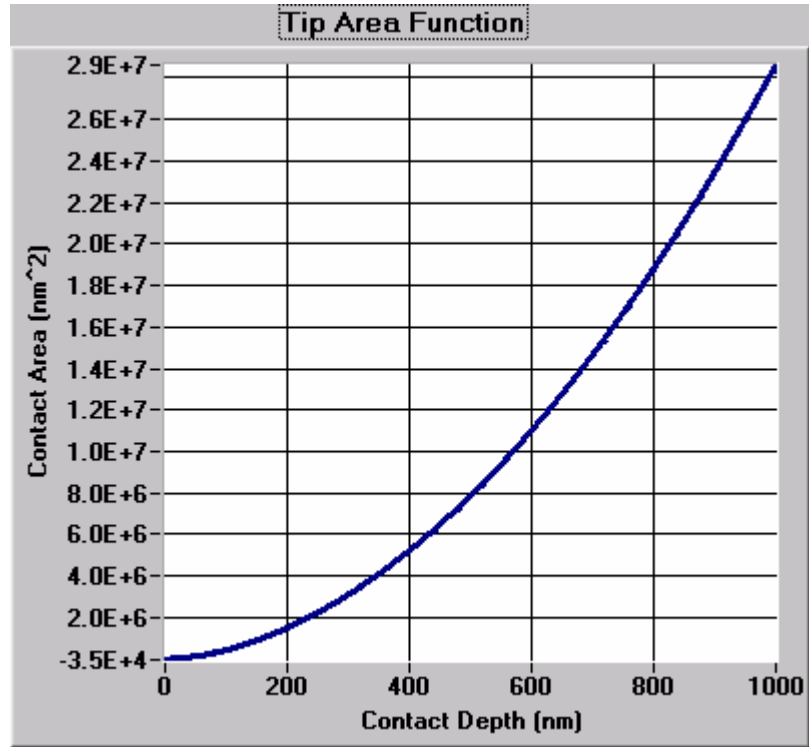


Figure 5-1. Tip area function used for calculation of mechanical properties.

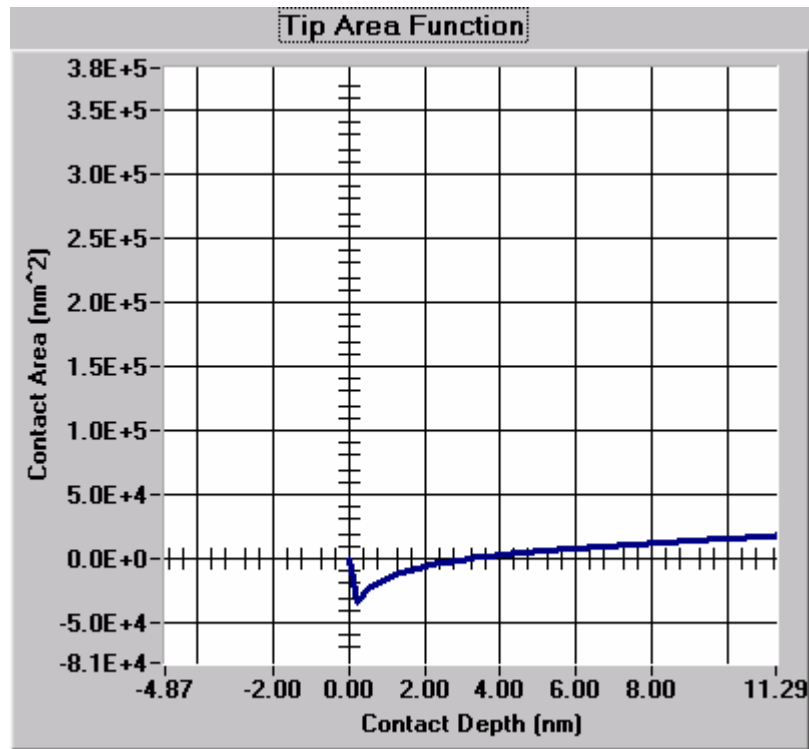


Figure 5-2. Example of erroneous fitting of tip area function in depth below 5nm range.

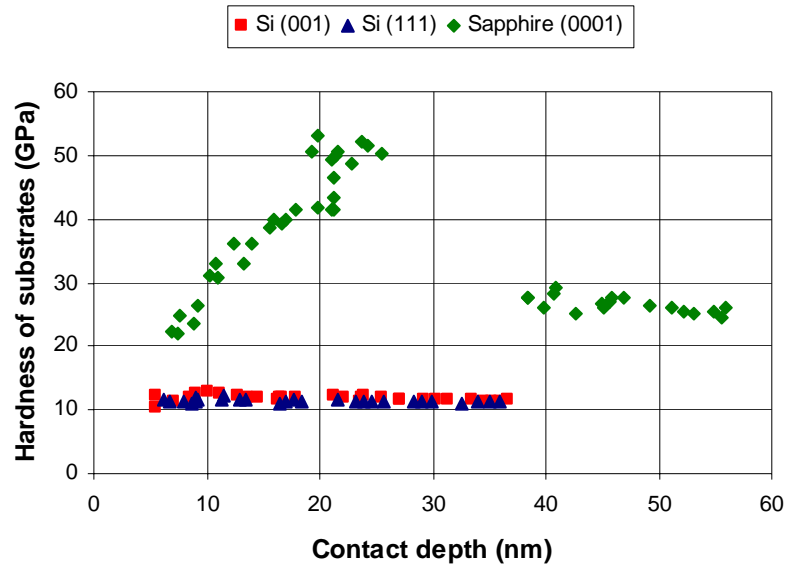


Figure 5-3. Hardness of Si (001), Si (111), and sapphire (0001) single crystal substrates.

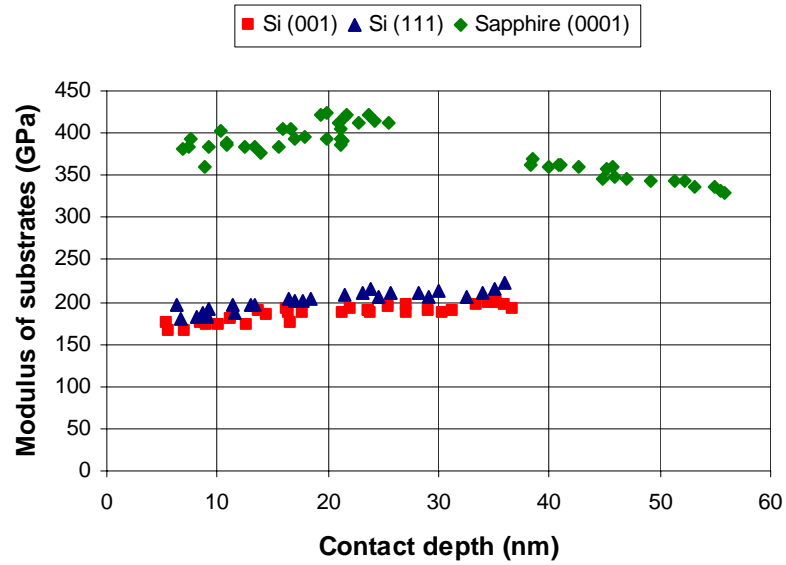


Figure 5-4. Young's modulus of Si (001), Si (111), and sapphire (0001) single crystal substrates.

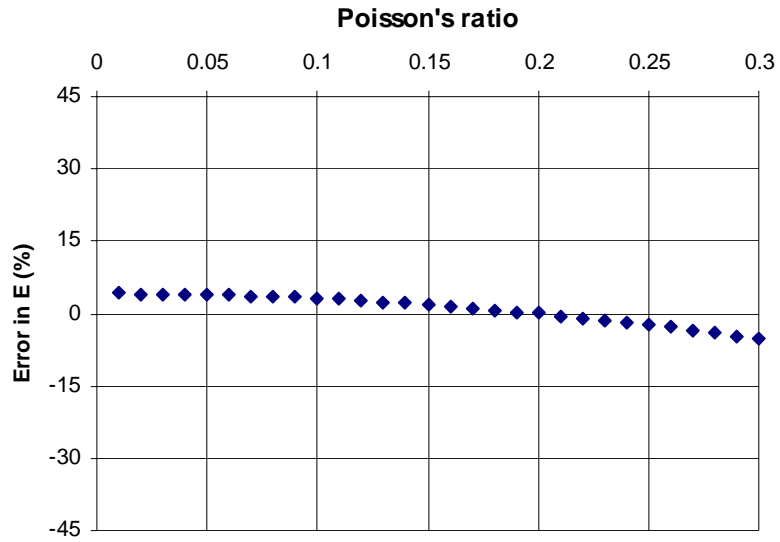


Figure 5-5. Error range change in Young's modulus as function of Poisson's ratio of substrate according to eq. (5-1).

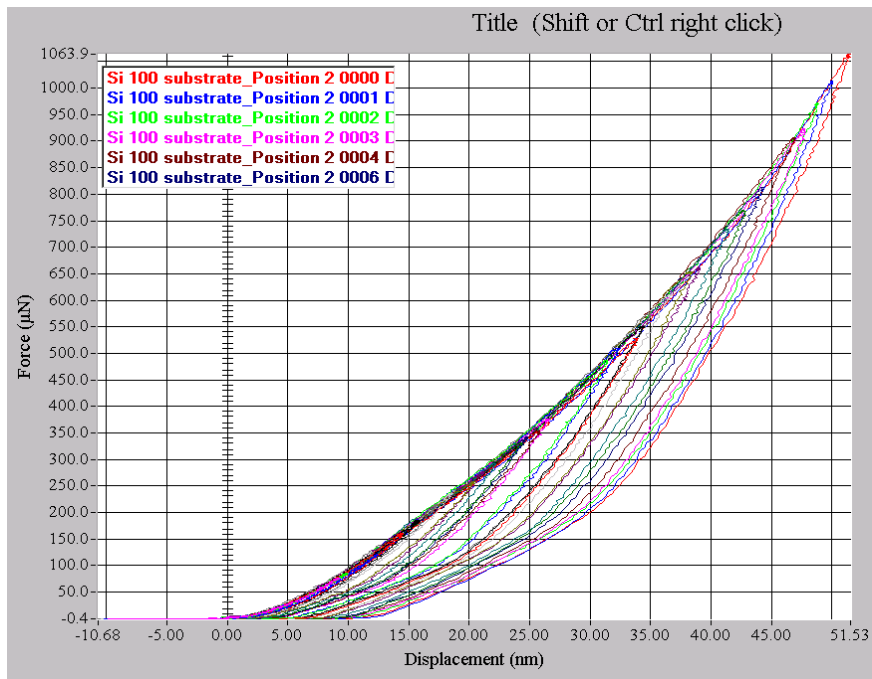


Figure 5-6. Load-displacement curves of Si (001) substrate.

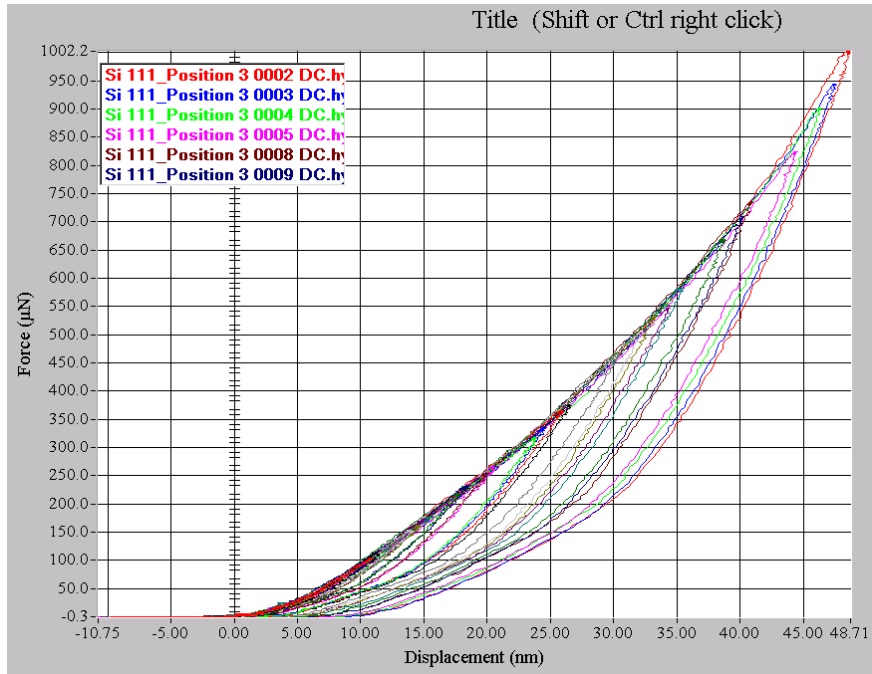


Figure 5-7. Load-displacement curves of Si (111) substrate.

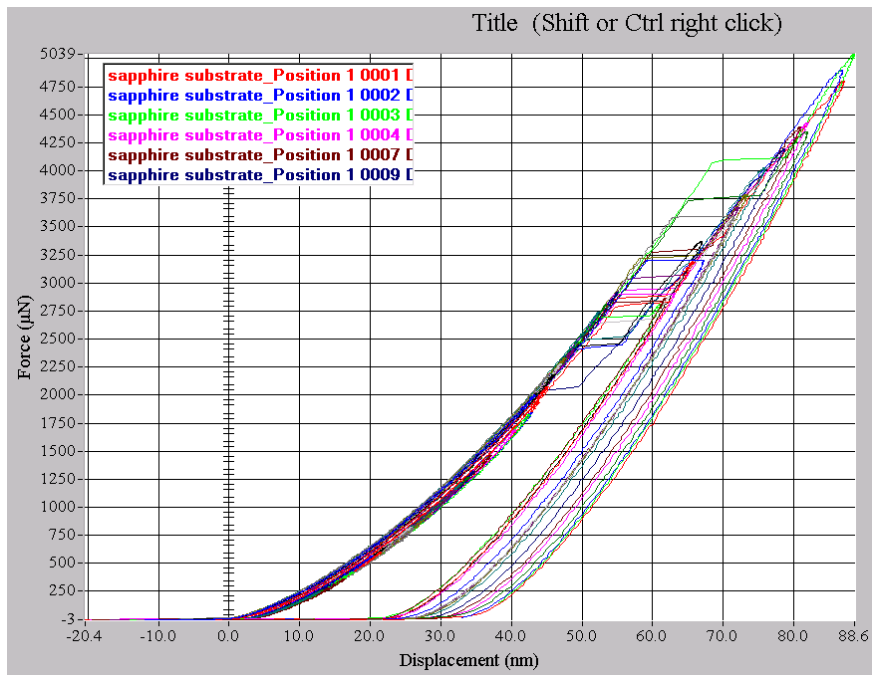


Figure 5-8. Load-displacement curves of sapphire (0001) substrate.

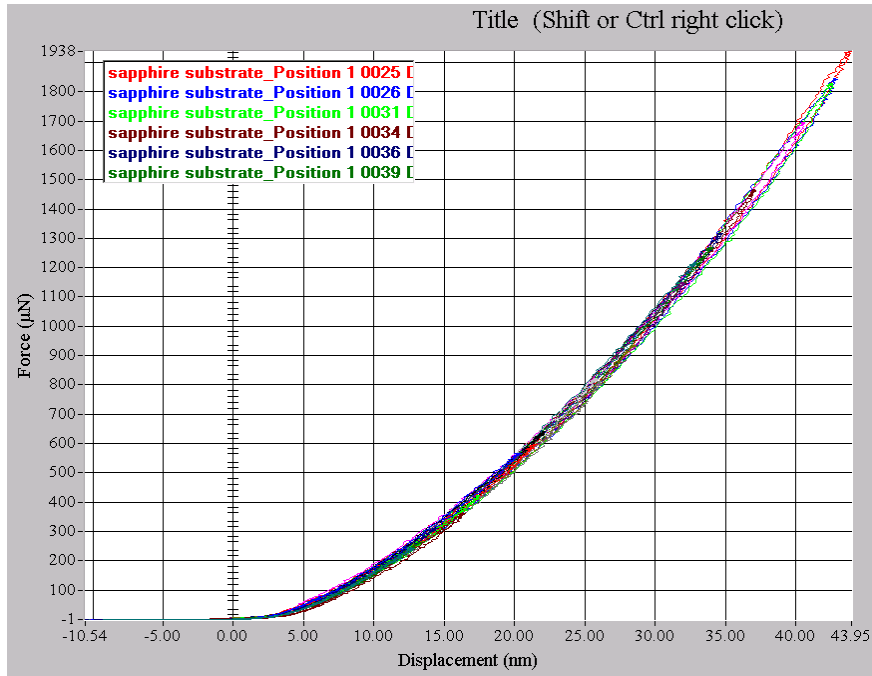


Figure 5-9. Load-displacement curves of sapphire (0001) substrate before 'pop-in' occurs.

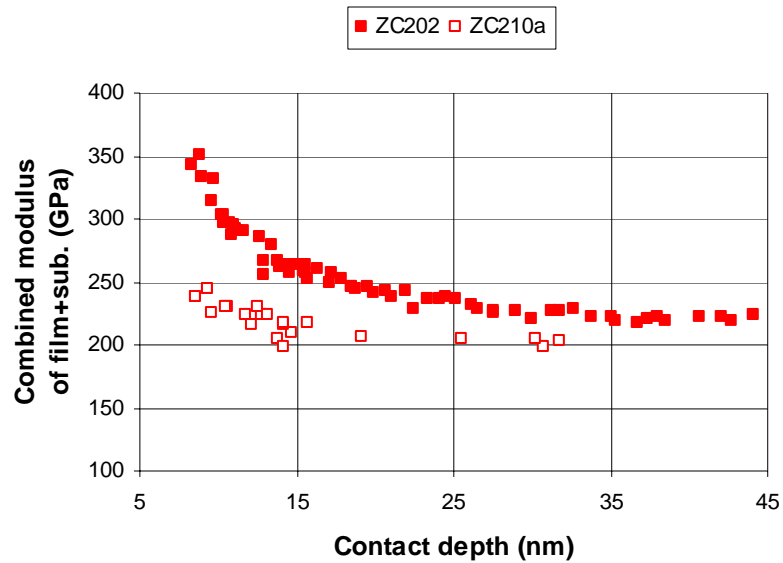


Figure 5-10. Combined modulus of film and substrate for different quality of ZrC (001) grown on Si (001) substrate. FWHM of ZC202 = 2.53, FWHM of ZC210a = 7.27 in omega rocking curve.

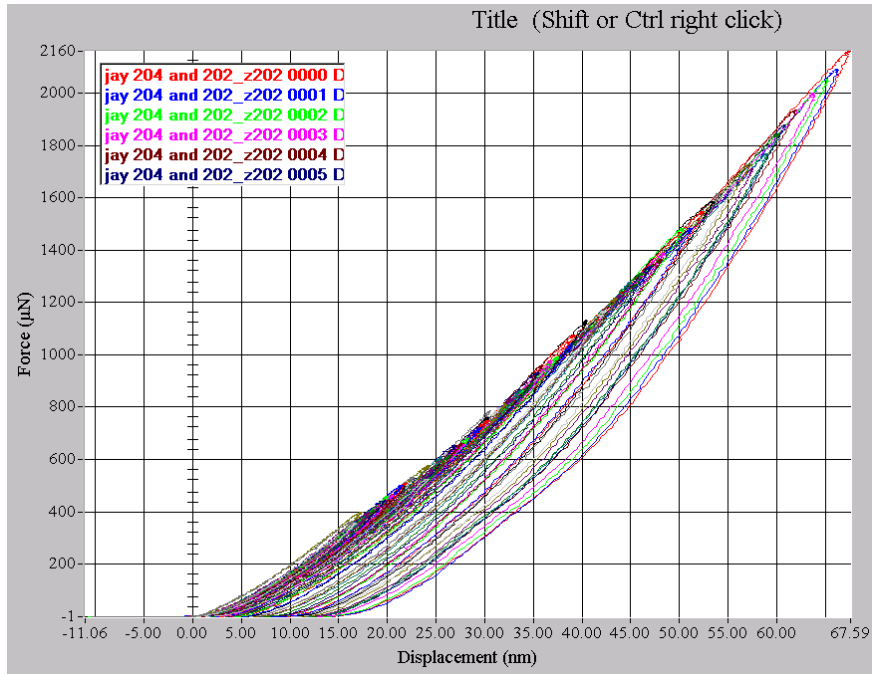


Figure 5-11. Load-displacement curves of ZrC (001) grown on Si (001) substrate, sample ZC202 in fig 5-10.

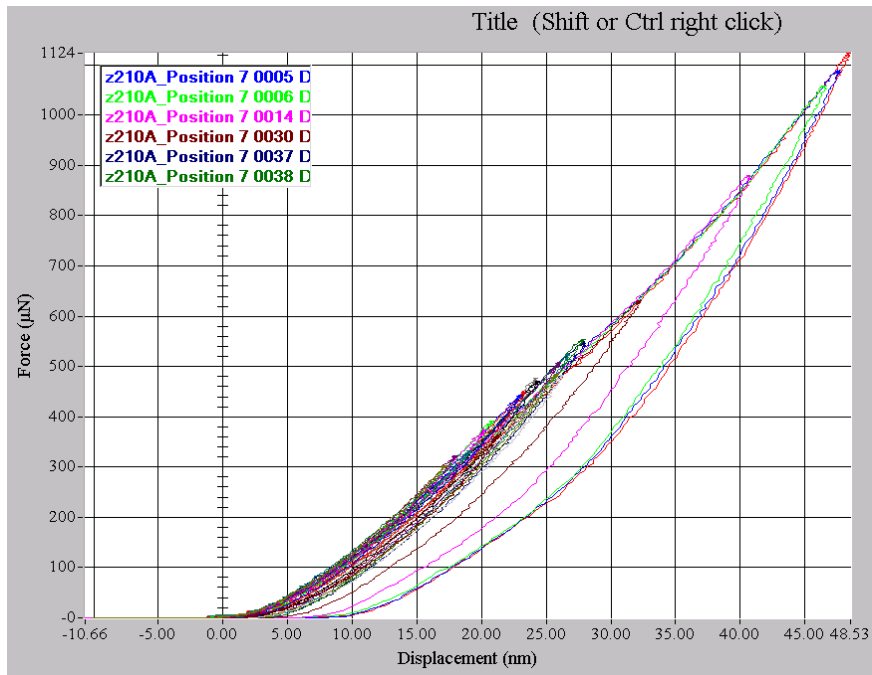


Figure 5-12. Load-displacement curves of ZrC (001) grown on Si (001) substrate, sample ZC202 in fig 5-10.

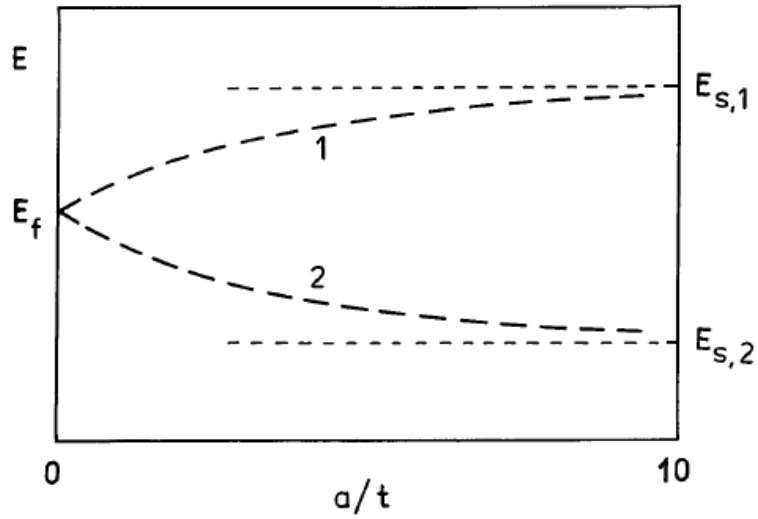


Figure 5-13. Measured elastic modulus as a function of relative penetration into a coated specimen ( $a$  is contact radius, and  $t$  is film thickness). For curve 1,  $E_{\text{film}}$  is less than  $E_{\text{substrate}}$ , and opposite case for curve 2 [Men97].

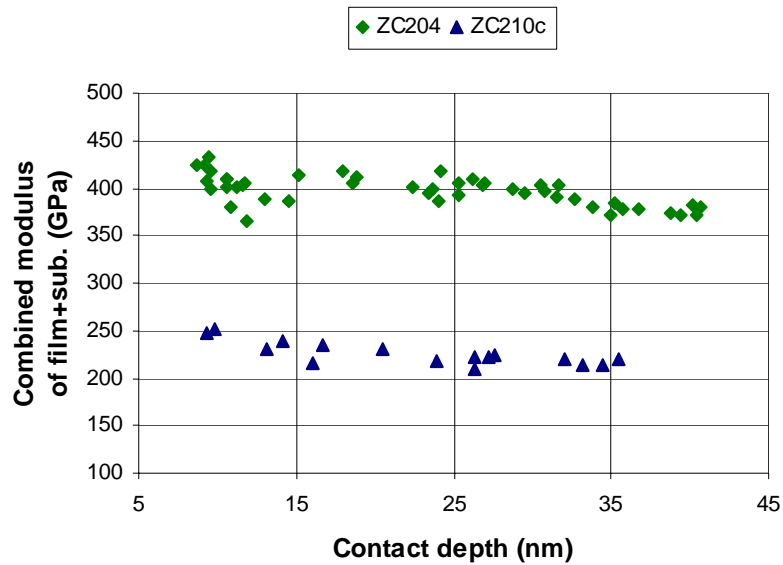


Figure 5-14. Combined modulus of film and substrate for different quality of ZrC (111) grown on sapphire (0001) and Si (001) substrate, sample ZC204 and ZC210c respectively. FWHM of ZC204 = 2.53, FWHM of ZC210c = 6.95 in omega rocking curve.

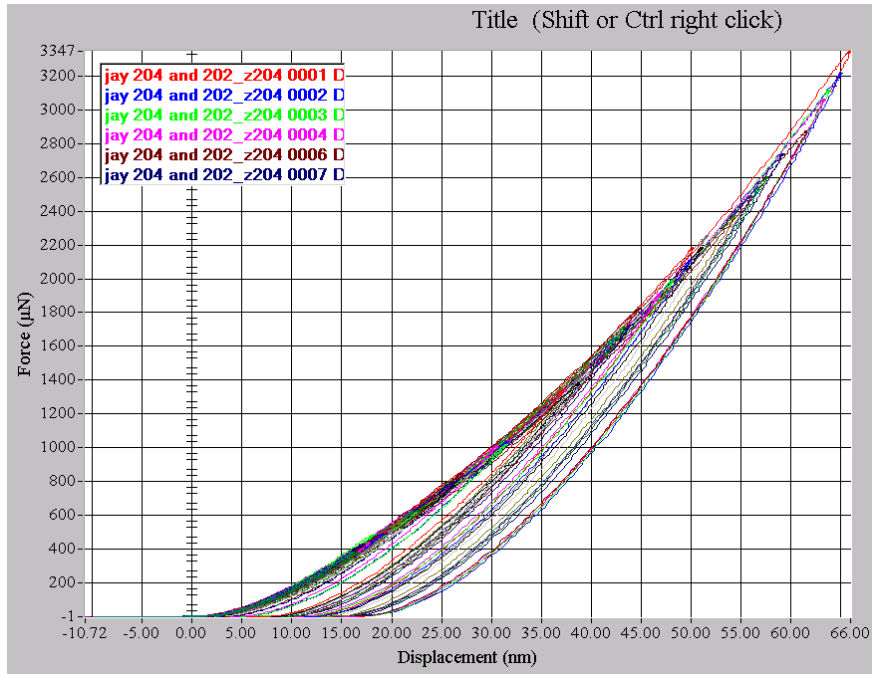


Figure 5-15. Load-displacement curves of ZrC (111) grown on sapphire (0001) substrate, sample ZC204 in fig 5-14.

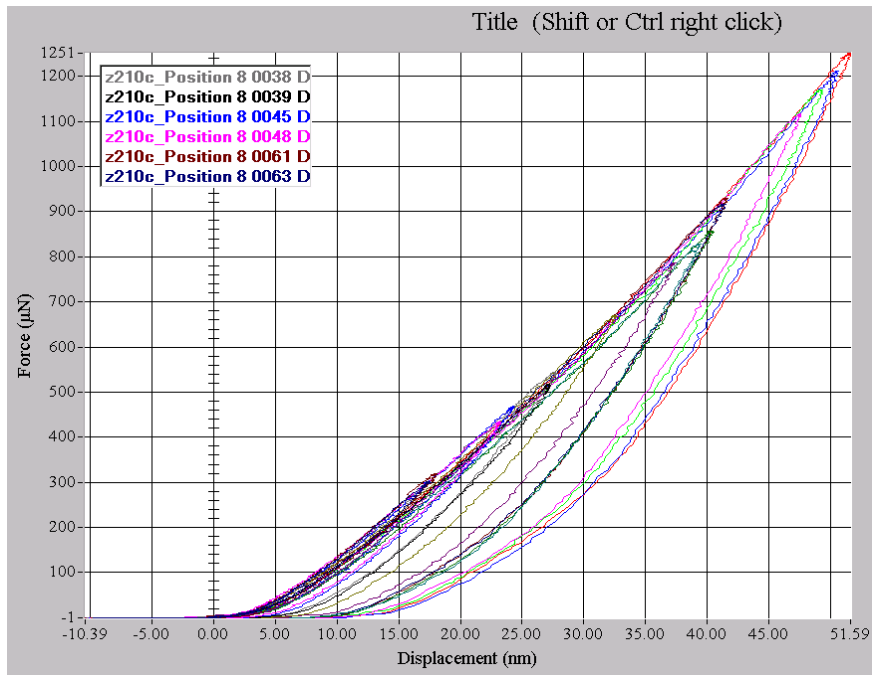


Figure 5-16. Load-displacement curves of ZrC (111) grown on Si (111) substrate, sample ZC210c in fig 5-14.

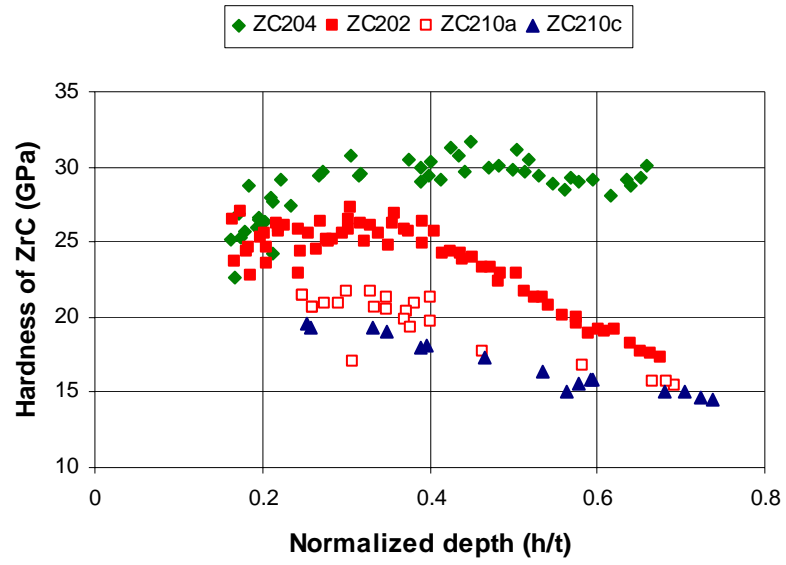


Figure 5-17. Combined hardness of ZrC and substrate as a function of normalized depth; h - displacement, t - film thickness.

## CHAPTER 6 CONCLUSION

Epitaxial ZrC thin films were deposited on Si (001), Si (111), and sapphire (0001) substrates by the pulsed laser deposition technique. First of all, ZrC thin films were grown on chemically cleaned Si (001) substrate with various process parameters except laser pulse repetition rate of 5 Hz. Under the temperature range of 200~600 °C and/or laser fluence below 6 J/cm<sup>2</sup>, resulting ZrC films showed no crystallinity. By increasing the laser fluence at 8 J/cm<sup>2</sup> and substrate temperature at 600 °C, we obtained ZrC film that showed some crystallinity. However, when the ZrC target was not pre-ablated for at least 1 min, XRD spectra showed as-grown films were a substoichiometric ZrC, which was caused by the oxidation of target surface. A combination of high laser fluence around 10 J/cm<sup>2</sup> and high substrate temperature of 600 ~ 700 °C was required to obtain high crystalline films. Under these conditions films grew with a (001) texture on Si (001) substrate. Grazing incidence x-ray diffraction investigations, which are much more surface sensitive than symmetric XRD investigations, evidenced the presence of a rather small fraction of randomly oriented crystallites. According to GIXD and XPS investigation, low pressure of C<sub>2</sub>H<sub>2</sub> as background gas gave a little beneficial effect on enhancing crystallinity and stoichiometry. XPS study confirmed that the surface layers contained mainly Zr-O bonds. After a 5 minute Ar<sup>+</sup> sputtering process, a homogeneous composition of Zr-C and Zr-O was found in the surface region.

The study was then focused on the use of a high laser fluence of 10 J/cm<sup>2</sup> and high substrate temperature around 750 °C on Si (001), Si (111), and sapphire (0001) substrates.

10 Hz repetition rate of laser pulse was used because growth rate was rather low at 5 Hz. To avoid oxidation problem, special care was taken to maintain low water vapor pressures during depositions, below  $\sim 10^{-8}$  Torr, as measured with a residual gas analyzer attached to the deposition chamber. Prior to deposition, the Si substrates were heated up to 900 °C for 20 min under high vacuum to remove the native oxide. Under these conditions, epitaxial ZrC films were deposited on single crystalline substrates. The ZrC films grew along the [001] axis on Si (001), while they grew along the [111] axis on Si (111) and sapphire (0001). Pole figure measurements showed that ZrC films exhibited in-plane orientation too, depending on the type of substrate. For sapphire (0001) substrate case, pole figure analysis revealed parallel in-plane relationship between  $\langle 11\bar{2}0 \rangle$  of sapphire and  $\langle 110 \rangle$  of ZrC, which indicates a 30° rotation of ZrC lattice with respect to the sapphire lattice, and six {100} reflections from ZrC film in (100) pole figure showed that twinning was occurred during growth. This in-plane orientation relationship was well explained by translational symmetries on both sides of the interface. Grazing incidence x-ray diffraction investigations evidenced the presence of a rather small fraction of randomly oriented crystallites in these films. TEM investigation on cross-sectional specimen showed clear lattice fringes over wide region for all case, corroborating the epitaxial growth indicated by XRD results. For Si (111) substrates only, several Moiré fringes were observed, indicating randomly oriented crystallites. For sapphire substrates two types of twin boundary were found; one was perpendicular to surface of film, and the other was parallel to surface. This fact suggests the Stranski-Krastanov (island after monolayer) growth model because these two types of twinning are possible when some nuclei grow in the ABCABC order, and other nuclei grow in ACBACB order during the

initial stage of growth. Omega rocking-curves measurement showed that ZrC film had best lateral out-of-plane alignment but relatively rather poor in-plane alignment due to twinning. ZrC (001) films showed good quality both in-plane and out-of-plane. ZrC (111) films grown on Si (111) showed (111) preferred orientation with rather poor quality in epitaxy, which was controlled by moderated  $C_2H_2$  background gas pressure. Lattice parameter of deposited ZrC film was changed by small variations of  $C_2H_2$  pressure. There exists an optimum pressure value for good crystal quality. AES surface composition analysis showed oxygen concentration both on surface of film and in bulk (7~8%) was still high. Despite the high levels of oxygen contamination, the deposited ZrC films were very conductive. Under best vacuum conditions ( $P_o = 1.3\sim 1.5 \times 10^{-7}$  Torr) and using a low pressure of high purity  $CH_4$  during deposition, oxygen concentration was less than 2.5 %, a very good value for ZrC. Simulation result using a three layer model from XRR spectra showed that the films mass density was around the tabulated value of  $6.7 \text{ g/cm}^3$ , while the surface morphology was very smooth, with a roughness value (rms) of around 0.6 nm.

Epitaxial ZrC films deposited by using the pulsed laser deposition technique were tested for hardness and elastic modulus using depth sensing nanoindentation. In nanoindentation measurement, surface cleanness, accurate area function, and indenter tip stability when approaching near surface were critical problems in getting correct data. Both hardness and elastic modulus predominantly depended on crystalline quality rather than their textures. High value of hardness ( $\sim 31 \text{ GPa}$ ) and elastic modulus (over 450 GPa) were obtained for high crystalline quality ZrC (111) deposited on sapphire substrate, one of the highest values reported so far.

Finally, as a future work, it is worth noting that films grown at low temperature of only 300 °C and a rather low laser fluence of only 2 J/cm<sup>2</sup> from a ZrC doped with Co target exhibited sharp diffraction lines, as one can see in fig. 6-1. However, because the films were well textured, exhibiting only three diffraction lines, the crystalline compound formed was not identified. The properties such as electrical resistivity and electron emission of these Co doped ZrC films are worth being investigated further because the rather low processing temperature and laser fluence were required to obtain good crystallinity.

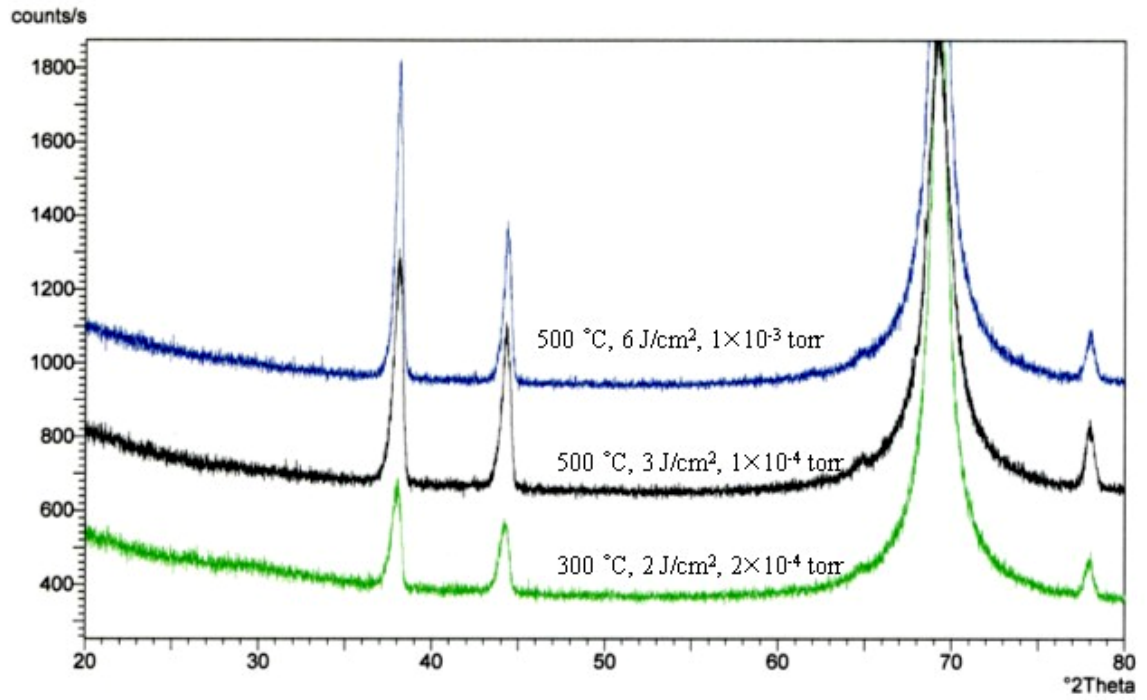


Figure 6-1. XRD spectra of thin films deposited from a Co doped ZrC target under various conditions.

## LIST OF REFERENCES

- [Ada74] H. Adachi, Y. Shibuya, T. Hariu, and Y. Shibats, *J. Phys. D* 7, 2150 (1974).
- [Ale00] L. D'Alessio, A. Santagata, R. Teghil, M. Zaccagnino, I. Zaccardo, V. Marotta, D. Ferro, and G. De Maria, *Appl. Surf. Sci.* 168, 284 (2000).
- [Asm01] M. Asmani, C. Kermel, A. Leriche, and M. Ourak, *J. Euro. Ceram. Soc.* 21, 1081 (2001).
- [Auc01] O. Auciello and A. R. Krauss, *In Situ Real-Time Characterization of Thin Films*, Wiley-Interscience, New York (2001).
- [Ber95] H. Berndt, A.-Q. Zeng, H.-R. Stock, and P. Mayer, *Surf. Coat. Technol.* 74/75, 369 (1995).
- [Bhu96] B. Bhushan and X. Li, *J. Mater. Res.* 12(1), 54 (1997).
- [Bra66] D. G. Brandon, *Acta Metall.* 14, 1479 (1966).
- [Bra92] E. A. Brandes and G. B. Brook, *Smithells Metals Reference Book*, 7<sup>th</sup> Edition, Butterworth-Heinemann, Oxford, 11-159 (1992).
- [Bre62] F. Breech and L. Cross, *Appl. Spectrosc.* 16, 59 (1962).
- [Brü93] J. Brückner and T. Mänytlä, *Suf. Coat. Technol.* 59, 166 (1993).
- [Cac99] D. Caceres, I. Vergara, R. Gonzalez, E. Monory, F. Calle, E. Munoz, and F. Omnes, *J. Appl. Phys.* 86, 6773 (1999).
- [Cha99] F. M. Charbonnier, W. A. Mackie, T. Xie, and P. R. Davis, *Ultramicroscopy* 79, 73 (1999).
- [Cha01] F. M. Charbonnier, W. A. Mackie, R. L. Hartman, and T. Xie, *J. Vac. Sci. Technol. B*19, 1064 (2001).
- [Che05a] C.-S. Chen, C.-P. Liu, and C. -Y. A. Tsao, *Thin Solid Films* 479, 130 (2005).
- [Che05b] S. Chen, L. Liu, and T. Wang, *Suf. Coat. Technol.* 191, 25 (2005).

- [Chr94] D. B. Chrisey and G. K. Hubler, Pulsed Laser Deposition of Thin Films, Wiley-Interscience, New-York, 188 and 342-353 (1994).
- [Coc98] D. Cocke and M. Owens, Appl. Surf. Sci. 31, 471 (1998).
- [Coc99] B. V. Cockeram, D. P. Measures, and A. J. Mueller, Thin Solid Films 17, 355 (1999).
- [Dij87] D. Dijkamp, T. Venkatesan, X.D. Wu, S.A. Shaheen, N. Jisrawi, Y.H. Min-Lee, W.L. McLean, and M. Croft, Appl. Phys. Lett. 51, 619 (1987).
- [Doe86] M. F. Doerner and W. D. Nix, J. Mater. Res. 1, 601 (1986).
- [Dye89] P. E. Dyer, R. D. Greenough, A. Issa, and P. H. Key, Appl. Surf. Sci. 43, 387 (1989).
- [Eda96] K. Edamoto, T. Anazawa, S. Tokumitsu, A. Tanabe, R. Sekine, E. Miyazaki, H. Kato, and S. Otani, Solid State Commun. 97, 435 (1996).
- [Han95] K. Hanko, G. Vass, and L. Szepes, J. Organometallic Chem. 492, 235 (1995).
- [He98] X.-M. He, L. Shu, H.-B. Li, H.-D. Li, and S.-T. Lee, J. Vac. Sci. Technol. A16, 2337 (1998).
- [Hol77] C. M. Hollabaugh, L. A. Wahman, R. D. Reiswig, and R. W. White, Nucl. Tech. 35, 527 (1977).
- [How02] J. M. Howard, V. Craciun, C. Essary, and R. K. Singh, Appl. Phys. Lett. 81, 3431 (2002).
- [Hu91] S. M. Hu, J. Appl. Phys. 69(11), 7901 (1991).
- [Kas78] D. Kashchiev, Thin Solid Films 55, 399 (1978).
- [Kau90] W. Kautek, B. Roas, and L. Schultz, Thin Solid Films 191, 371 (1990).
- [Kuc00] S.O. Kucheyev, J.E. Bradby, J.S. Williams, C. Jagadish, M. Toth, M.R. Phillips, and M.V. Swain, Appl. Phys. Lett. 77, 3373 (2000).
- [Lew78] B. Lewis and J. C. Anderson, Nucleation and Growth of Thin Films, Academic Press, New York (1978).
- [Lid05] D. R. Lide, Handbook of Chemistry and Physics on CD-ROM version 2005, CRC press (2005).
- [Mac92] W. A. Mackie, J. L. Morrissey, C. H. Hinrichs, and P. R. Davis, J. Vac. Sci. Technol. A 10, 2852 (1992).

- [Mac93] W. A. Mackie, R. L. Hartman, and P. R. Davis, *Appl. Surf. Sci.* 67, 29 (1993).
- [Mac94] W. A. Mackie, R. L. Hartman, M. A. Anderson, and P. R. Davis, *J. Vac. Sci. Technol. B* 12, 722 (1994).
- [Mac95] W. A. Mackie, T. Xie, and P. R. Davis, *J. Vac. Sci. Technol. B* 13(6), 2459 (1995).
- [Mac98a] W. A. Mackie, T. Xie, J. E. Blackwood, S. C. Williams, and P. R. Davis, *J. Vac. Sci. Technol. B* 16, 1215 (1998).
- [Mac98b] W. A. Mackie, T. Xie, M. R. Matthews, B. R. Routh, Jr., and P. R. Davis, *J. Vac. Sci. Technol. B* 16 2057 (1998).
- [Mac98c] W. A. Mackie, T. Xie, M. R. Matthews, and P. R. Davis, *Mater. Res. Soc. Symp. Proc.* 509, 173 (1998).
- [Mah99] S. Mahajan and K. S. S. Harsha, *Principles of Growth and Processing of Semiconductors (International Editions)*, McGraw-Hill, Seoul, 264 (1999).
- [Mat86] A. Matsunawa, S. Katayama, A. Susuki, and T. Ariyasu, *Trans. J. Welding Res. Technol.* B3, 968 (1986).
- [Men97] J. Menčík, D. Munz, E. Quandt, and E. R. Weppelmann, *J. Mater. Res.* 12, 2475 (1997).
- [Met89] S. Metev and K. Meteva, *Appl. Surf. Sci.* 43, 402 (1989).
- [Mod85] F. A. Modine, T. W. Haywood, and C. Y. Allison, *Phys. Rev. B* 32(12), 7743 (1985).
- [Név80] L. Névtot and P. Croce, *Rev. Phys.* 15, 761 (1980).
- [Now99] R. Nowak, M. Pessa, M. Sukanuma, M. Leszczynski, I. Grzegory, S. Porowski, and F. Yoshida, *Appl. Phys. Lett.* 75, 2070 (1999).
- [Oga86] T. Ogawa and K. Ikawa, *High Temp. Sci.* 22, 179 (1986).
- [Oga92] T. Ogawa, K. Fukuda, S. Kashimura, T. Tobita, F. Kobayashi, S. Kado, H. Miyanishi, I. Takahashi, and T. Kikuchi, *J. Am. Ceram. Soc.* 75, 2985 (1992).
- [Oli92] W. C. Oliver and G. M. Pharr, *J. Mater. Res.* 7, 1564 (1992).
- [Oya92a] S. T. Oyama, *Catalysis Today* 15(2), 179 (1992).
- [Oya92b] S. T. Oyama, *Journal of Solid State Chemistry* 96, 442 (1992).

- [Par54] L. G. Parratt, *Phys. Rev.* 95, 359 (1954).
- [Pcp94] PCPDFWIN Version 1.00, Joint Committee on Powder Diffraction International Centre for Diffraction Data (JCPDS-ICDD) (1994).
- [Pri92] D. L. Price, B. R. Cooper, and J. M. Wills, *Phys. Rev. B* 46, 11368 (1992).
- [Rey74] G. H. Reynolds, *J. Nucl. Mater.* 50, 215 (1974).
- [Rus02] C. H. Russell, *Mat. Res. Symp. Proc.* 716, B1.3.1 (2002).
- [She97] J. R. Sheats, W. A. Mackie, S. Anz, and T. Xie, *Proc. SPIE* 3148, 219 (1997).
- [Shi98] S. Shimada, M. Yoshimatsu, M. Inagaki, and S. Otani, *Carbon* 36, 1225 (1998).
- [Smi65] H.M. Smith and A.F. Turner, *Appl. Opt.* 4, 147 (1965).
- [Smi93] D. C. Smith, R. R. Rubiano, M. D. Healy, and R. W. Springer, *Mater. Res. Soc. Symp. Proc.* 282, 643 (1993).
- [Spr86] W. D. Sproul, *J. Vac. Sci. Technol. A* 4(6), 2874 (1986).
- [Tem99] D. Temple, *Mat. Sci. Engr.* R24, 185 (1999).
- [Tes93] T. C. Tessner and P. R. Davis, *J. Vac. Sci. Technol. A* 11(1), 1 (1993).
- [Tot71] L. E. Toth, *Transition Metal Carbides and Nitrides*, Academic, New York (1971).
- [Tsu99] T.Y. Tsui and G.M. Phraa, *J. Mater. Res.* 14, 292 (1999).
- [Var94] D. J. Varacalle, Jr., L. B. Lundberg, H. Herman, G. Bancke, and W. L. Riggs II, *Surf. Coat. Technol.* 68/69, 86 (1994).
- [Ven84] J. A. Venables, G. D. T. Spiller, and M. Hanbucken, *Rep. Prog. Phys.* 47, 399 (1984).
- [Wag76] P. Wagner, L. A. Wahman, R. W. White, C. M. Hollabaugh, and R. D. Reiswig, *J. Nucl. Mater.* 62, 228 (1976).
- [Wor65] J. J. Wortman and R. A. Evans, *J. Appl. Phys.* 36(1), 153 (1965).
- [Xie96] T. Xie, W. A. Mackie, and P. R. Davis, *J. Vac. Sci. Technol. B* 14, 2090 (1996).
- [Yim74] W. M. Yim and R. J. Paff, *J. Appl. Phys.* 45(3), 1456 (1974).

- [Yu98] G. Yu, H. Ishikawa, T. Egawa, T. Soga, J. Watanabe, T. Jimbo, and M. Umeno, *J. Cryst. Growth* 189/190, 701 (1998).
- [Zab94] H. Zabel, *Appl. Phys.* A58, 159 (1994).
- [Zai84] S. Zaima, H. Adachi, and Y. Shibata, *J. Vac. Sci. Technol. B* 2(1), 73 (1984).
- [Zur84] A. Zur and T. C. McGill, *J. Appl. Phys.* 55(2), 378 (1984).

## BIOGRAPHICAL SKETCH

Juhyun Woo was born in Deagu, Korea, November 8, 1972. He attended Duk-won High School in Deagu, Korea. After his graduation with a BS in metallurgical engineering from Kyungpook National University in 2000, his education continued with graduate studies at University of Florida in the Department of Materials Science and Engineering.